

University of Alberta

**A High-Resolution Anisotropic Finite-Volume
Head Model for EEG Source Analysis**

by

Michael Jay Douglas Cook



A thesis submitted to the Faculty of Graduate Studies and Research
in partial fulfillment of the requirements for the degree of

Master of Science

**Department of Electrical and Computer Engineering
Department of Biomedical Engineering**

**Edmonton, Alberta
Fall 2008**



Library and
Archives Canada

Bibliothèque et
Archives Canada

Published Heritage
Branch

Direction du
Patrimoine de l'édition

395 Wellington Street
Ottawa ON K1A 0N4
Canada

395, rue Wellington
Ottawa ON K1A 0N4
Canada

Your file Votre référence
ISBN: 978-0-494-47195-1
Our file Notre référence
ISBN: 978-0-494-47195-1

NOTICE:

The author has granted a non-exclusive license allowing Library and Archives Canada to reproduce, publish, archive, preserve, conserve, communicate to the public by telecommunication or on the Internet, loan, distribute and sell theses worldwide, for commercial or non-commercial purposes, in microform, paper, electronic and/or any other formats.

The author retains copyright ownership and moral rights in this thesis. Neither the thesis nor substantial extracts from it may be printed or otherwise reproduced without the author's permission.

AVIS:

L'auteur a accordé une licence non exclusive permettant à la Bibliothèque et Archives Canada de reproduire, publier, archiver, sauvegarder, conserver, transmettre au public par télécommunication ou par l'Internet, prêter, distribuer et vendre des thèses partout dans le monde, à des fins commerciales ou autres, sur support microforme, papier, électronique et/ou autres formats.

L'auteur conserve la propriété du droit d'auteur et des droits moraux qui protègent cette thèse. Ni la thèse ni des extraits substantiels de celle-ci ne doivent être imprimés ou autrement reproduits sans son autorisation.

In compliance with the Canadian Privacy Act some supporting forms may have been removed from this thesis.

Conformément à la loi canadienne sur la protection de la vie privée, quelques formulaires secondaires ont été enlevés de cette thèse.

While these forms may be included in the document page count, their removal does not represent any loss of content from the thesis.

Bien que ces formulaires aient inclus dans la pagination, il n'y aura aucun contenu manquant.

■ ■ ■
Canada

Abstract

Source analysis of the electroencephalogram (EEG) provides a noninvasive method of localizing electrical/functional activity of the brain and is particularly important in the diagnosis of certain neurological disorders such as epilepsy. This research focuses on improving the accuracy of EEG source analysis by developing a high-resolution finite-volume head model that accounts for anisotropic conductivities of the human head. The numerical accuracy of the finite volume method (FVM) formulation is evaluated, with the analytical solution for a spherical head serving as the “gold standard” of comparison. The FVM formulation is shown to produce accurate results, but severe anisotropy appears to be a problem at the current head model resolution. Additionally, the effect of anisotropy on EEG source analysis is investigated using realistic head model geometries and conductivities obtained from magnetic resonance images. It is determined that anisotropy should not be ignored since a significant amount of source localization error can occur.

Acknowledgement

I would like to thank my supervisor, Dr. Zoltan Koles, for the time and effort he has invested in helping me throughout this research project. It has been a pleasure to work for someone who genuinely cares about the success of his students in their personal and professional lives. I would also like to thank my fellow graduate students in Dr. Koles' lab. Dan Withey, John Russell, Todd Penney, Natasha Kuzbik, and Aisha Yahya have all been a valuable source of technical support and, more importantly, friendship. The contributions of summer students Doug Vujanic and Kelvin Chow to portions of this research, even after they had finished their work in Dr. Koles' lab, are also gratefully acknowledged.

I would like to express my gratitude to Lora Major, whose assistance during the early stages of my research was an invaluable resource. Thank you also to Luis Concha and Yusuf Bhagat for helping me to acquire, analyze, and interpret the MRI and DTI data sets that I used over the course of my research. As well, I would like to express my appreciation to Dr. Vien Van for sharing his knowledge of computational electromagnetics.

I would like to thank my family and friends for their encouragement and support throughout my research project.

Financial support for this research was provided by the Natural Sciences and Engineering Research Council (NSERC) of Canada, the Alberta Informatics Circle of Research Excellence (iCORE), Alberta Ingenuity, the Alberta Heritage Scholarship Fund, and the University of Alberta.

Table of Contents

Chapter 1: Introduction.....	1
1.1 Motivation and Objectives	1
1.2 Thesis Organization	2
Chapter 2: Background Information	3
2.1 Basic Head Anatomy	3
2.2 Epilepsy.....	4
2.3 EEG Source Analysis.....	5
2.4 Forward Problem	6
2.4.1 Quasi-static Conditions.....	6
2.4.2 Poisson's Equation.....	6
2.4.3 Boundary Conditions	7
2.5 Current Source Model.....	8
2.6 Tissue Conductivity	10
2.7 Anisotropic Conductivity	11
2.8 Head Volume Conductor Models	15
2.8.1 Analytical Models.....	15
2.8.2 Numerical Models.....	16
2.8.2.1 Boundary Element Method.....	18
2.8.2.2 Finite Difference Method.....	20
2.8.2.3 Finite Element Method	22
2.8.2.4 Finite Volume Method.....	25
2.9 Inverse Problem	28
2.9.1 Lead Field Analysis	28
2.9.2 Reciprocity.....	30
Chapter 3: Anisotropic Finite-Volume Head Model in 2D.....	32
3.1 Head Model Development	33
3.1.1 Voxel-Centered Approach	34
3.1.2 Vertex-Centered Approach	39
3.2 Head Model Comparison	45
3.2.1 Methods.....	45
3.2.1.1 Forward Problem Solution.....	46
3.2.1.2 Memory Requirements.....	48
3.2.2 Results.....	50
3.2.2.1 Forward Problem Solution.....	50
3.2.2.2 Memory Requirements.....	52
3.2.3 Discussion.....	52
Chapter 4: Anisotropic Finite-Volume Head Model in 3D.....	55
4.1 Head Model Development	55
4.2 System Matrix Properties.....	65

Chapter 5: Head Model Validation	67
5.1 Methods.....	67
5.1.1 Forward Problem Solution.....	67
5.1.1.1 Conjugate Gradient Method.....	68
5.1.1.2 Matrix Deflation.....	69
5.1.1.3 Matrix Preconditioning.....	70
5.1.1.3.1 Jacobi Preconditioning.....	71
5.1.1.3.2 Polynomial Preconditioning with Chebyshev Polynomials.....	72
5.1.2 Inverse Problem Solution.....	73
5.1.3 Validation Experiments	74
5.1.3.1 Surface Voltage Error	74
5.1.3.2 Source Localization Error	78
5.2 Results.....	82
5.2.1 Surface Voltage Error	82
5.2.2 Source Localization Error	87
5.3 Discussion.....	88
 Chapter 6: Effect of Neglecting Anisotropy.....	 93
6.1 Methods.....	93
6.1.1 Realistic Head Model.....	93
6.1.2 Source Localization Error	97
6.2 Results.....	100
6.3 Discussion.....	104
 Chapter 7: Conclusions and Future Directions.....	 107
 References	 110

List of Tables

Table 3.1: Circular head model conductivities.	47
Table 3.2: Forward problem solution comparison for 2D FVM approaches.....	50
Table 5.1: Spherical head model conductivities.	76
Table 5.2: Electrode configuration.	79
Table 5.3: Surface voltage error for a radial dipole at an eccentricity of 0.8.	82
Table 5.4: Surface voltage error for a tangential dipole at an eccentricity of 0.8.....	83
Table 5.5: Surface voltage error for a radial dipole at an eccentricity of 0.5.	83
Table 5.6: Surface voltage error for a tangential dipole at an eccentricity of 0.5.....	84
Table 5.7: Spherical head model source localization error.....	87
Table 5.8: Average PCG method solution time on the spherical head model.	88
Table 6.1: Source localization error due to neglecting anisotropy.	100

List of Figures

Figure 2.1: A simplified view of human head anatomy.....	3
Figure 2.2: Current dipole and its associated parameters.	9
Figure 2.3: Conductivity tensor ellipsoid.....	12
Figure 2.4: Node numbering used by the isotropic FDM head model.....	21
Figure 2.5: Visual representation of the lead field matrix.	29
Figure 3.1: Computational grid for the 2D FVM voxel-centered approach.	34
Figure 3.2: Secondary cells used for the 2D FVM voxel-centered approach.....	36
Figure 3.3: Computational grid for the 2D FVM vertex-centered approach.	40
Figure 3.4: Current flow through a control volume face.	41
Figure 3.5: Normalized voltage contour plots for anisotropy ratio of 1:1.	51
Figure 3.6: Normalized voltage contour plots for anisotropy ratio of 10:1.	51
Figure 4.1: Node numbers for the 3D FVM computational grid.	56
Figure 4.2: Voxel labels for the 3D FVM computational grid.	56
Figure 4.3: Labeling convention for a control volume face.....	58
Figure 4.4: Current flow through a control volume face.	59
Figure 5.1: Electrode placement on the spherical head model.	79
Figure 5.2: Surface voltages for a tangential dipole at an eccentricity of 0.8.....	85
Figure 5.3: Surface voltages for a tangential dipole at an eccentricity of 0.5.....	86
Figure 6.1: Real head and segmented head comparison.	95
Figure 6.2: Three-dimensional representation of the realistic head model.....	96
Figure 6.3: Electrode placement on the realistic head model.	98
Figure 6.4: Source localization error histograms.	101
Figure 6.5: Normalized scalp voltages for the realistic head model.....	103
Figure 6.6: Normalized scalp voltages for an axial slice of the realistic head model.....	104

Chapter 1: Introduction

The research presented in this thesis introduces a new tool that will hopefully improve the quality of life for people with epilepsy. This chapter will establish the motivation and objectives of the research and will outline of the organization used in this thesis.

1.1 Motivation and Objectives

Electroencephalogram (EEG) source analysis is a tool that can potentially provide an accurate, noninvasive method of analyzing and localizing specific electrical activity in the brain. This tool could be particularly valuable in the pre-surgical planning for epilepsy patients, and may even aid in the selection of appropriate medication for non-surgical epilepsy patients. With epilepsy being one of the most common serious neurological disorders in the world [1, 2], EEG source analysis could drastically improve the quality of life for many people. EEG source analysis basically consists of solving two problems: the forward problem and the inverse problem. While the forward problem involves calculating the scalp potentials generated by a known current source, the inverse problem involves calculating the location, orientation, and magnitude of a current source from measured EEG scalp potentials. A head volume conductor model is an essential part of the solution to both these problems and it can include realistic head geometry, tissue distributions, and tissue conductivities. In fact, the utility of EEG source analysis can ultimately be determined by the accuracy of the available head volume conductor model. Consequently, a high-resolution, realistic, patient-specific head model is considered a vital component of EEG source analysis.

The research in this thesis focuses on improving the accuracy of EEG source analysis by developing a more realistic head volume conductor model. Specifically, a high-resolution head model will be developed with the finite volume method (FVM) and will account for anisotropic conductivities. The inclusion of anisotropic conductivities is very important since some tissues, such as the skull and white matter, are known to be highly anisotropic [3, 4]. Unfortunately, much research on EEG source analysis continues to neglect anisotropy and use head models that assume all tissues are isotropic. Therefore, it is felt that an anisotropic FVM head model will be an invaluable contribution to the

field of EEG source analysis and could aid in improving the quality of life for epilepsy patients.

1.2 Thesis Organization

The remainder of this thesis is organized into seven chapters. Chapter 2 presents the relevant background information related to epilepsy and EEG source analysis. Particular attention is paid to the topics of anisotropy and head volume conductor models. Chapter 3 showcases the development and comparison of two different FVM head models that incorporate anisotropy. The head models are developed in two dimensions and are based on voxel- and vertex-centered approaches to the FVM. In Chapter 4, the vertex-centered approach to the FVM is expanded to three dimensions and the important system matrix properties are examined. Chapter 5 evaluates the accuracy of this anisotropic FVM head model by quantifying the modeling error associated with the FVM. This validation is done using a spherical head for which an analytical solution exists and is used as the “gold standard” of comparison. Chapter 6 uses the anisotropic FVM head model to investigate the effect of neglecting anisotropic conductivities. The error associated with not including anisotropy is quantified using a realistic head model, which is obtained using magnetic resonance images. Finally, Chapter 7 attempts to draw some conclusions from this research and ideas are presented for future directions to take this research.

Chapter 2: Background Information

This chapter will introduce the relevant background information for the research presented in this thesis. Both epilepsy and electroencephalogram (EEG) source analysis are discussed with more detailed descriptions for topics related to the forward and inverse problems.

2.1 Basic Head Anatomy

In order to better understand epilepsy and EEG source analysis, it is convenient to have some basic knowledge of the anatomy of the human head. From a simplified point of view, the human head consists of scalp on the outer surface, which surrounds the skull. The brain lies within the skull and the spaces between the brain and the skull, as well as some ventricles within the brain, are filled with cerebrospinal fluid (CSF). The brain itself is composed of both gray matter (GM) and white matter (WM). The GM portion of the brain primarily consists of cell bodies and occurs on the outer surface of the brain, known as the cerebral cortex, as well as some locations within the brain. The WM portion of the brain, on the other hand, primarily consists of nerve fibers that connect the cell bodies and occur below the cerebral cortex. All of these tissues are illustrated in Figure 2.1, which depicts a cutaway view of the human head.

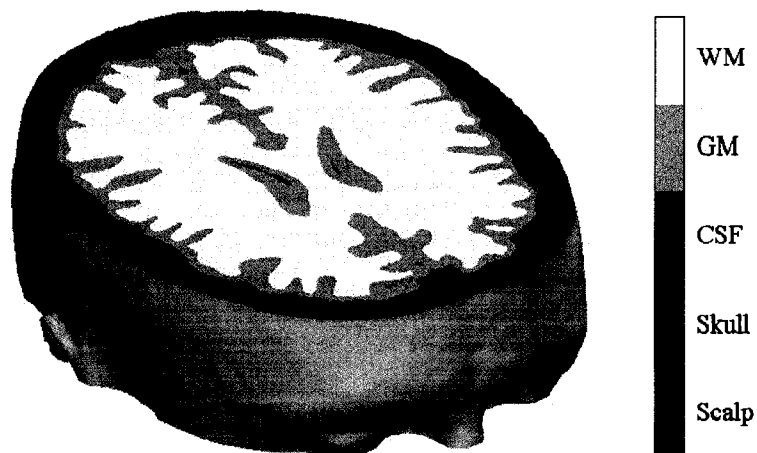


Figure 2.1: A simplified view of human head anatomy.

2.2 Epilepsy

Epilepsy is one of the most common serious neurological disorders, affecting 0.5% to 2% of the population, or roughly 60 million people worldwide [1, 2]. In Canada alone, it is estimated that 15500 new cases of epilepsy are diagnosed each year [1]. Epilepsy is characterized by seizures, which are sudden and excessive electrical discharges in the cerebral cortex [1, 5, 6]. Seizures can vary from patient to patient and can vary in severity and frequency. In fact, the physical manifestation of this abnormal electrical activity can be anything from a brief stare, an unusual body movement, a change in awareness, or even a convulsion [1].

While there are many different types of seizures associated with epilepsy, a classification system of epileptic seizures has been developed. Recognizing the type of seizure is often the first step towards being able to treat a patient's epilepsy [1]. Seizures are typically classified into two main categories: generalized and partial seizures. Generalized seizures begin with a widespread electrical discharge that involves the entire brain [7]. Partial seizures, however, begin with an electrical discharge that is restricted to a focal point within the brain [1]. Partial seizures affect the largest portion of the population, with approximately 60% of adult epilepsy patients experiencing them [1].

The major form of treatment of epilepsy is long-term drug therapy, with seizures being successfully controlled by medication in up to 70% of patients [2]. However, it is important to note that this is not a cure, and there can be numerous, sometimes severe, side effects associated with anti-epileptic medications [1]. For those patients with medically intractable epilepsy, surgical treatment offers a potential cure. This means that, when successful, surgery can completely eliminate a patient's seizures and drastically improve their quality of life. Unfortunately, the probability of an patient being seizure-free after surgery is not 100%, and, in some cases, can be as low as 29% [8]. The success rate of surgery is highly dependent on the pre-surgical identification of the region of the brain causing the seizures, also known as the epileptogenic focus. For this reason, surgery is only recommended for patients with partial epilepsy, since the seizures can be localized to one area of the brain [1]. The necessity of accurately localizing the epileptogenic focus is apparent because the patient may still suffer from seizures if not enough of the brain is removed. Conversely, if too much of the brain is removed, there may be functional

deficits in the patient's brain. While the importance of accurately localizing the epileptogenic focus is obvious, a noninvasive clinical or laboratory test that can be used for such a purpose does not exist.

2.3 EEG Source Analysis

The EEG is a very useful clinical tool that records the electrical activity of the brain and is routinely used to diagnose and investigate brain disorders. The physiological basis for this technology is that the activation of pyramidal cells in the cerebral cortex generates an electric field which can be detected as an electric potential by EEG scalp electrodes [6]. The EEG is particularly useful in the study and diagnosis of epilepsy and is, in fact, the main investigative tool for localizing the epileptogenic focus.

One approach that is widely employed in a clinical setting involves visually inspecting the EEG time series or the scalp voltage topography. While it is possible to determine the approximate electrical source location with this technique, it is still a highly qualitative process. Consequently, more quantitative approaches to locate the sources of the EEG have been and are currently being researched, with some of the earliest efforts starting over 50 years ago [9]. The aim of such research, termed EEG source analysis, is to create a tool that will provide an accurate, noninvasive method of analyzing and localizing specific electrical activity in the brain. This tool could be particularly valuable in the pre-surgical planning for epilepsy patients, and may even aid in the selection of appropriate medication for non-surgical epilepsy patients.

There are two key problems in the field of EEG source analysis: the forward problem and the inverse problem. The process of calculating the scalp potentials generated by a known current source in the brain constitutes the forward problem. This involves using a mathematical model to approximate how current propagates through the head. Both the geometric and conductive properties of the head must be modeled, as well as the current source generating the electrical activity. The process of calculating the location, orientation, and magnitude of the current source from measured EEG scalp potentials constitutes the inverse problem. Ultimately, both the forward and inverse problems must be solved to localize the source of neural activity. It is the solutions to all possible forward problems that provide the necessary data for the inverse problem to

determine the source location responsible for generating the measured EEG scalp potentials.

2.4 Forward Problem

The forward problem involves calculating the electric potential generated by a known current source at any point in the head. While the forward problem has a unique solution, finding this solution requires knowledge of the how electrical signals propagate in the head. For EEG source analysis, several approximations are typically made to justify using quasi-static conditions. Under these conditions, Poisson's equation is used to mathematically describe the electrical activity in the head and solve the forward problem. In order to obtain an accurate solution, it is also important to satisfy both Neumann and Dirichlet boundary conditions. The following sections will discuss these topics in greater detail.

2.4.1 Quasi-static Conditions

When solving bioelectric problems, such as EEG source analysis, it is usually assumed that quasi-static conditions exist. This assumption is justified since it has been shown that the frequency of internal bioelectric activity is quite low, with the highest frequency being on the order of 1 kHz [10]. At these low frequencies the capacitive component of tissue impedance can be considered negligible and tissue can be modeled as a purely resistive medium [11]. Additionally, it has been shown that time delay effects can be neglected since changes in sources of bioelectric activity are much slower than the rate of signal propagation [12]. This means that at any instant in time, time-varying currents and fields behave as if they were stationary [10].

2.4.2 Poisson's Equation

Under quasi-static conditions, Maxwell's equations can be used to derive Poisson's equation, the partial differential equation which governs electrical activity in the head. Poisson's equation is defined as

$$\nabla \cdot (\boldsymbol{\sigma} \nabla \phi) = -I_v, \quad (2.1)$$

where σ is the tissue conductivity tensor with units of S/m, ϕ is the electric potential distribution with units of V, and I_v is the current source density with units of A/m³. For the case when there is no current source, Poisson's equation is called Laplace's equation and is defined as

$$\nabla \cdot (\sigma \nabla \phi) = 0. \quad (2.2)$$

For EEG source analysis, the electric potential satisfies Poisson's equation at every location in the head volume conductor model. With a given current source and head model, (2.1) can be used to calculate the electric potential and solve the forward problem. While Poisson's equation is the governing equation, there are two other equations that are also commonly used to describe the electrical activity in the head. The electric field, \mathbf{E} , has units of V/m and is defined as

$$\mathbf{E} = -\nabla \phi, \quad (2.3)$$

while the current density, \mathbf{J} , has units of A/m² and is defined by Ohm's Law as

$$\mathbf{J} = \sigma \mathbf{E}. \quad (2.4)$$

2.4.3 Boundary Conditions

Satisfying the appropriate boundary conditions is an important consideration when solving bioelectric problems. In the case of EEG source analysis, both Neumann and Dirichlet boundary conditions must be considered at the interface between two different regions. Two different regions can be characterized by their conductivities, σ_1 and σ_2 , and the unit normal vector to the interface between the regions, $\hat{\mathbf{n}}$. Neumann boundary conditions are used to specify the normal component of current at a boundary. Since the head is modeled as a purely resistive medium, no charge can accumulate at an interface and there must be current continuity. This means that all current leaving one region through an interface must enter the adjacent region, such that

$$(\sigma_1 \nabla \phi_1) \cdot \hat{\mathbf{n}} = (\sigma_2 \nabla \phi_2) \cdot \hat{\mathbf{n}}. \quad (2.5)$$

At the outer boundary of the head, no current can flow from the head into the surrounding air, due to the extremely low conductivity of the air. This homogeneous Neumann boundary condition is specified on the surface of the head, such that

$$(\boldsymbol{\sigma}_1 \nabla \phi_1) \cdot \hat{\mathbf{n}} = 0. \quad (2.6)$$

Dirichlet boundary conditions are used to specify the value of the electric potential at a boundary. The electric potential must be continuous across interfaces, such that

$$\phi_1 = \phi_2. \quad (2.7)$$

Additionally, a reference electrode for the EEG must be specified with a given electrical potential. The reference electrode is usually assigned a potential of zero, such that

$$\phi_{\text{ref}} = 0. \quad (2.8)$$

In order to obtain an accurate solution, all these boundary conditions need to be taken into account when solving the forward problem.

2.5 Current Source Model

The most common and simplest current source model used in EEG source analysis is the equivalent current dipole. It has been shown that current dipoles can adequately approximate the electric field produced by an active region of the cerebral cortex at a single instant in time [13-15]. In fact, there is a strong physiological basis for this assertion. Pyramidal cells are aligned parallel with each other and perpendicular to the cortical surface. When several square centimeters of these geometrically aligned cells are synchronously active, they generate an electric field that is detectable by the EEG [14]. Since the distance to the EEG electrodes is relatively large compared to the size of the patch of active pyramidal cells, the electric potential detected on the scalp commonly has a dipolar configuration; that is, the scalp voltage topography has two maxima, one negative and one positive [14]. Therefore, the instantaneous electric field can be effectively modeled by a single equivalent current dipole.

A current dipole consists of a current source and a current sink that insert and remove equal amounts of current, I , and are separated by distance, d , as illustrated in Figure 2.2. The position of the dipole is typically chosen to be halfway between the

source and the sink. The orientation and magnitude of the dipole can be characterized by the dipole moment, \mathbf{p} , a vector directed from the sink to the source that is defined as

$$\mathbf{p} = Id\hat{\mathbf{n}}_d, \quad (2.9)$$

where $\hat{\mathbf{n}}_d$ is the unit vector defining the direction from the sink to the source. In general, a dipole in Cartesian coordinates can be represented as

$$\mathbf{p} = p_x\hat{\mathbf{x}} + p_y\hat{\mathbf{y}} + p_z\hat{\mathbf{z}}, \quad (2.10)$$

where $\hat{\mathbf{x}}$, $\hat{\mathbf{y}}$, and $\hat{\mathbf{z}}$ are the unit basis vectors for the Cartesian coordinate system, and p_x , p_y , and p_z are the dipole's Cartesian components. To simplify the forward problem calculations, a dipole of arbitrary orientation can be represented by three separate dipoles, one in each of the three mutually orthogonal directions. Since Poisson's equation is linear, the principle of superposition can be applied and the forward problem results for each of the separate dipoles can be summed to yield the results for the net dipole.

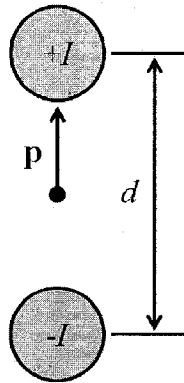


Figure 2.2: Current dipole and its associated parameters.

While it is most common to use a single current dipole to represent EEG data at one instance in time, sometimes more complex source activity can evolve in the brain over time. This necessitates the use of a more complicated source model when considering the temporal evolution of EEG measurements. Spatiotemporal dipole modeling is a technique that uses multiple dipoles that are fixed in location and orientation, but are allowed to vary in magnitude and polarity to account for the time-varying EEG measurements [14]. The principle of superposition is extremely important

for the spatiotemporal dipole model since any distribution of single dipoles can be summed in order to represent an arbitrarily complex current source evolving over a period of time.

2.6 Tissue Conductivity

A common issue that arises in EEG source analysis is determining what conductivity values should be used for head volume conductor models. The most simplistic of such models usually differentiate the scalp, skull, and brain, while more accurate models include CSF, GM, and WM. Each of these tissues has a unique conductivity and it has been reported [16-21] that EEG source analysis can be significantly influenced by using incorrect values. Therefore, the more accurately each conductivity value is known, the more accurately EEG source analysis can be performed.

Ideally, patient-specific conductivity values should be obtained for every tissue in the head whenever EEG source analysis is required. Recently, some non-invasive approaches to measuring the conductivity of the head have been reported, including diffusion tensor imaging (DTI) [22-24], electrical impedance tomography [25], and others [26, 27]. While some of these methods are still fairly new and are limited in what tissue conductivities they can measure, there is promise that eventually all head models will use patient-specific conductivity values. Currently, though, it is more common to use values from past studies that are readily available from the literature [3, 25, 28-38]. These measurements are extremely valuable in modeling the head, but, it is important to realize that there will be some variability between people and not all tissues will exhibit a homogeneous conductivity throughout. As well, due to the large number of studies and differing methods of measuring conductivity, there exists much variability among the reported conductivity values and, unfortunately, there is little consensus as to what the most accurate values are.

When it comes to determining accurate conductivity values, much of the focus has been placed on the scalp, skull, and brain since three-tissue head models are quite popular. The scalp and brain have similar conductivities and, in most studies, are assumed to be identical, while the skull has a much smaller conductivity. It is often sufficient to specify the conductivity of these three tissues as a relative value, a ratio that

defines the conductivity between the scalp, skull, and brain. The most widely used scalp-to-skull-to-brain conductivity ratio has long been 1:1/80:1, which was reported in 1968 [4] and again in 1983 [39]. However, in recent years the accuracy of this ratio has become highly disputed and new measurements of the conductivity ratio have been obtained [25, 33, 36, 40]. Of these new measurements, the conductivity ratio of 1:1/15:1 reported in [33] seems to be the most accurate since it used both *in vivo* and *in vitro* conductivity measurements. It should be noted that, while conductivity ratios are a convenient way to specify conductivity, their use is limited to localizing current sources and can not provide information about the magnitude of the sources or the electric potentials. If accurate magnitude values are desired, accurate absolute values for the conductivities must be used.

2.7 Anisotropic Conductivity

A property, such as conductivity, is considered anisotropic if its value has a directional dependence. Conversely, a property is considered isotropic if its value is independent of direction. In general, anisotropic conductivity is a much less intuitive concept than isotropic conductivity. Isotropic conductivity has the same value regardless of direction and is mathematically described by a scalar value, σ . Anisotropic conductivity, however, has a value that varies with direction and is mathematically described by a tensor, $\boldsymbol{\sigma}$. A conductivity tensor is a 3×3 matrix that is both symmetric and positive definite, and is defined as

$$\boldsymbol{\sigma} = \begin{bmatrix} \sigma^{xx} & \sigma^{xy} & \sigma^{xz} \\ \sigma^{xy} & \sigma^{yy} & \sigma^{yz} \\ \sigma^{xz} & \sigma^{yz} & \sigma^{zz} \end{bmatrix}. \quad (2.11)$$

The diagonal elements of a conductivity tensor relate voltage in one direction to a current in the same direction. For example, σ^{xx} determines how much current in the x -direction is due to a voltage in the x -direction. On the other hand, the tensor off-diagonal elements relate voltage in one direction to a current in a perpendicular direction. For example, σ^{xy} determines how much current in the x -direction is due to a voltage in the y -direction.

And, since the tensor is symmetric, the σ^{xy} term also determines how much current in y -direction is due to a voltage in the x -direction.

Both the eigenvectors and eigenvalues of a conductivity tensor provide further information about the nature of the conductivity. While the eigenvectors define the principal directions of the conductivity, the eigenvalues define the magnitude of the conductivity along each of the corresponding principal directions. An ellipsoid is often used to provide a three-dimensional representation of a conductivity tensor. As illustrated in Figure 2.3, the axes of the ellipsoid are oriented in the direction of the conductivity tensor eigenvectors (\mathbf{e}_1 , \mathbf{e}_2 , and \mathbf{e}_3), and each axis is scaled by the corresponding eigenvalue (λ_1 , λ_2 , and λ_3) [22, 23]. Common shapes for conductivity tensor ellipsoids are cigar-shaped, when one eigenvalue is larger than the other two, and disk-shaped, when one eigenvalue is smaller than the other two [41]. Additionally, in the case of isotropic conductivity when all the eigenvalues are equal, the ellipsoid reduces to a sphere [41].

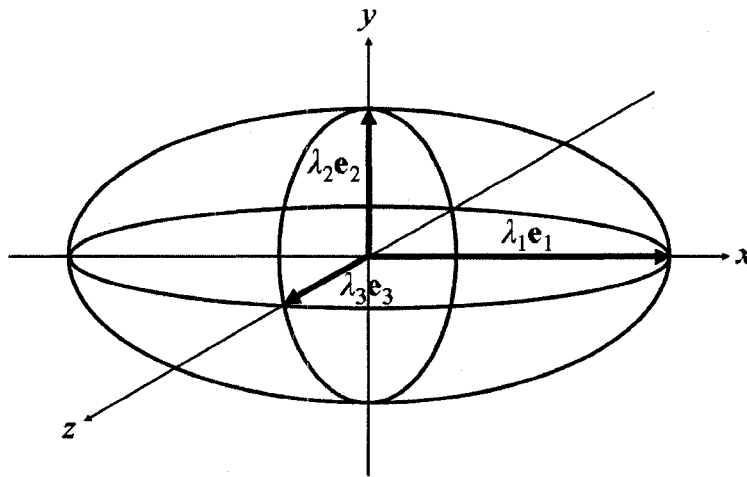


Figure 2.3: Conductivity tensor ellipsoid.

In EEG source analysis studies it is typically assumed that all tissues in the head have isotropic conductivities [18, 42-55]. This is a convenient assumption since most of the literature only cites isotropic conductivities. As well, head volume conductor models are much simpler when only isotropic conductivities are considered. While it is convenient to assume that all conductivities in the head are isotropic, this is an incorrect assumption since some tissue conductivities are actually anisotropic. For example, WM is

known to be highly anisotropic, being more conductive in the direction parallel to WM fiber tracts than perpendicular to the fiber direction. In fact, the ratio of conductivity in the parallel (longitudinal) direction to conductivity in the perpendicular (transverse) direction has been measured as approximately 9:1 [3]. In general, GM seems to be mostly isotropic [56]. However, some studies have indicated that GM may be slightly anisotropic, with conductivity measurements of GM in the cerebellum indicating a conductivity ratio of approximately 2:1 [32]. Another similar study reported a slightly higher ratio [57]. Like WM, the skull has also been reported to be highly anisotropic, being more conductive tangentially to the surface of the skull than radially to the surface of the skull. The ratio of conductivity in the tangential direction to conductivity in the radial direction has often been cited in the literature as being approximately 10:1 [58-61], a value that seems to have originated from [4]. It is important to realize that these anisotropic conductivity values, just like their isotropic counterparts in the literature, may vary within a particular tissue type and from person to person. Furthermore, the anisotropy may depend on the scale at which one looks at the tissue. For example, when considering the skull as a whole, it does indeed exhibit anisotropic conductivity. However, on a smaller scale, the origin of this anisotropy is revealed. Much of the skull actually consists of three layers: a middle layer of highly conductive spongy (cancellous) bone sandwiched between two layers of low conductivity compact (cortical) bone [21, 35, 38]. Therefore, instead of using anisotropic conductivity for the skull, some studies actually model the skull as three layers with isotropic conductivities [21, 45, 62], which may be appropriate in high-resolution head volume conductor models.

Regardless of the nature of the anisotropy in head tissues, it has been shown that if isotropic conductivities are used for tissues that are anisotropic, significant modeling errors can be introduced and adversely affect the accuracy of EEG source analysis [58, 60-63]. Unfortunately, a lack of robust, non-invasive techniques to measure conductivity tensors seems to have prevented many researchers from including anisotropic conductivities in their head volume conductor models [62]. Recently, however, it was proposed that conductivity tensors can be approximated from diffusion tensors obtained non-invasively with a relatively new magnetic resonance imaging (MRI) modality called DTI [22-24, 64]. DTI is an imaging technique that provides a quantitative measure of the

net diffusive movement of water in tissue [65]. The diffusion of water is fully described by a self-diffusion tensor, \mathbf{D} , which is both symmetric and positive definite, and is defined as

$$\mathbf{D} = \begin{bmatrix} D_{xx} & D_{xy} & D_{xz} \\ D_{xy} & D_{yy} & D_{yz} \\ D_{xz} & D_{yz} & D_{zz} \end{bmatrix}. \quad (2.12)$$

The relationship between conductivity and diffusion is based on the idea that, even though these two processes are fundamentally unrelated, the movement of ions and water molecules are both functions of the underlying tissue geometry [22, 23, 62]. In other words, boundaries presented by the tissue microstructure cause both ions and water molecules to move preferentially in the same direction. Based on this common geometry, conductivity and diffusion tensors are assumed to share the same eigenvectors and should only differ in their eigenvalues [64]. Using an effective medium approach, a strong linear relationship was shown to exist between the conductivity and diffusion tensor eigenvalues [23]. An approximation to this more formal relation exists, such that the linear relationship between the conductivity tensor, $\boldsymbol{\sigma}$, and the diffusion tensor, \mathbf{D} , is given by

$$\boldsymbol{\sigma} = \frac{\sigma_e}{d_e} \mathbf{D}, \quad (2.13)$$

where σ_e and d_e are the effective extracellular conductivity and diffusivity, respectively, and the ratio σ_e/d_e has been empirically determined to be $0.736 \text{ S}\cdot\text{s}/\text{mm}^3$ [62]. The approximate linear relationship given by (2.13) assumes that the intracellular conductivity and diffusivity are negligibly small, meaning that both conductivity and diffusion are mediated primarily by extracellular pathways [62]. Conductivity tensors obtained with DTI and calculated using the linear relationship have shown good agreement with conductivity values from the literature [23, 24]. More studies are probably still needed to sufficiently validate the accuracy of measuring conductivity tensors with DTI. However, DTI seems to be the best option for non-invasively obtaining patient-specific conductivity values. Additionally, DTI has the potential to all but

eliminate the need for segmentation of magnetic resonance (MR) images into the different tissue compartments. One limitation to DTI is that it cannot provide a measure of the conductivity tensor in the skull. DTI only measures the diffusion of water and, while most tissues in the head have a large concentration of water in them, the skull does not.

2.8 Head Volume Conductor Models

Head volume conductor models are essential to EEG source analysis, and in particular the forward problem. They can be grouped into two main categories: analytical models and numerical models. Analytical models are typically restricted in both the geometry and conductivity they can model, using a sphere or a set of concentric spheres to represent the head. Conductivities for the spheres can be isotropic or anisotropic, but must be homogeneous for each sphere. This simple geometry and conductivity distribution allows analytic expressions to be used to calculate the exact value of electric potentials on the surface of the head. Numerical models, on the other hand, provide a more approximate solution to Poisson's equation, but they offer much more freedom than analytical models. Complicated geometries and conductivity distributions can easily be handled by most numerical models. And, depending on the resolution of the numerical model, accuracies can easily approach that of the analytical models. There are several numerical methods that are commonly used for numerical volume conductors, including the boundary element method (BEM), the finite difference method (FDM), the finite element method (FEM), and the finite volume method (FVM). Each of these different numerical models, as well as the analytical models, will be discussed in the following sections.

2.8.1 Analytical Models

The most simple head models for EEG source analysis are analytically-derived spherical volume conductors, which use a sphere or a series of concentric spheres to represent the head. While it is obvious that spheres do not accurately portray the geometry of a real head, spherical volume conductors have long been popular since solutions to the forward problem can be easily and quickly calculated using analytical expressions. These analytical expressions may vary depending on the exact configuration of the volume conductor, but typically they involve an infinite series of Legendre polynomials to solve

Poisson's equation [4, 66-70]. The first such analytical model approximated the head using a single sphere with a homogeneous isotropic conductivity [66]. This was a very crude model that did not take into account the large difference in conductivity between the brain and the skull. As a result, concentric sphere models were introduced [4, 70, 71]. In these models, each sphere is given a radius that, on average, approximates the size of each tissue and each tissue is assigned a homogeneous isotropic conductivity. The most common of the concentric sphere models is the three-shell model, where three concentric spheres are used to represent the scalp, skull, and brain. While not as common, there have also been models that use five or more shells in an attempt to represent more tissue types. Another, slightly more complicated concentric sphere model uses shells that have anisotropic conductivities [67-69]. While still homogeneous within each sphere, the conductivity can vary in the radial and tangential directions. For each of these spherical head models, the electric potential on the scalp can be analytically calculated for a current dipole specified at any position within the head.

Several studies have been conducted to examine the use of a spherical head model as opposed to a realistically-shaped head model [53-55, 72]. These days, most researchers agree that spherical head models are much too simplistic to accurately perform EEG source analysis. It has been shown that dipole localization errors can be as large as several centimeters when a spherical head model is used instead of a realistic head model [14, 15, 53, 54, 72]. While some researchers may still use spherical models to solve the forward problem, more researchers use them solely to test the accuracy of their numerical head volume conductor models. In fact, analytical spherical models serve as the "gold standard" by which the performance of numerical models may be evaluated.

2.8.2 Numerical Models

With the increased accessibility to inexpensive and powerful computers, it is much more common for researchers to employ numerical head volume conductor models instead of analytical ones. Numerical head volume conductors use numerical methods to find a discrete approximation to the solution of Poisson's equation. They have the ability to accurately model realistic head geometry, including complex tissue boundaries and tissue distributions. Additionally, some numerical models can account for heterogeneous tissue conductivity distributions and anisotropic conductivity.

The first step in solving Poisson's equation numerically is generating a mesh or computational grid. This involves partitioning the computational domain (the head) into discrete sections based on tissue type and assigning conductivity values to these sections. Computational nodes are defined at N discrete locations within the computational grid and represent locations where an unknown approximate value of the solution is to be found. The second step involves using a numerical method to obtain a discrete version of Poisson's equation and apply the appropriate boundary conditions. Doing this for every node results in a finite system of algebraic equations that can be expressed in matrix form, such that

$$\mathbf{A}\mathbf{v} = \mathbf{i}, \quad (2.14)$$

where \mathbf{A} is an $N \times N$ system (or stiffness) matrix, \mathbf{v} is an $N \times 1$ vector containing the approximate electric potentials, and \mathbf{i} is an $N \times 1$ vector containing the current source terms. The final step in solving Poisson's equation numerically involves solving (2.14) to obtain the approximate solution, \mathbf{v} . While this can be accomplished with direct matrix inversion on smaller matrices, many system matrices are very large and sparse. Inverting such a matrix is more efficiently accomplished using iterative matrix inversion methods, such as successive over-relaxation, the preconditioned conjugate gradient (PCG) method, or the algebraic multigrid method [49].

When generating a realistic head model, MR images are typically used to obtain anatomical information such as head shape and tissue distributions. Image segmentation techniques are used to classify different tissue types, which are then used to assign the appropriate conductivity values to the computational grid. As previously mentioned, DTI has the potential to eliminate the need for tissue segmentation in some cases. Since tissue types are usually only required to assign conductivity values to the computational grid, DTI circumvents the need for image segmentation in tissues whose conductivity tensors can be measured.

The following sections will provide a basic description of the most common numerical methods used for head volume conductors, including the BEM, FDM, FEM, and FVM. While some brief mathematical descriptions of the individual methods will be described here, more detailed descriptions can be found in the referenced literature.

2.8.2.1 Boundary Element Method

The BEM is a numerical method that is commonly used to solve the forward problem in EEG source analysis [16, 42, 51, 53-55, 73-75]. Similar to some concentric spherical shell models, BEM head models represent the different tissues of the head with a series of nested regions characterized by homogeneous isotropic conductivities. Unlike spherical head models, though, these regions are realistically shaped. Geometric information from MR images is used to generate a tiled surface of triangles to more accurately represent the actual shape of the boundaries between the different head regions. Therefore, only the shell surfaces need to be discretized in BEM head models instead of the entire head volume. Consequently, the electric potential is only calculated for the shell surfaces, with the computational nodes being located at a point on the each of the triangular tiles.

In order to calculate the electric potential on each of the surfaces due to a dipole at position \mathbf{r}_0 , Poisson's equation is reformulated into an integral equation that is valid for a head model divided into n_s regions by closed surfaces, S_j ($j=1, \dots, n_s$). The electric potential, ϕ , at position $\mathbf{r} \in S_k$ is then given by

$$\phi(\mathbf{r}) = \frac{2\sigma_0}{\sigma_k^{in} + \sigma_k^{out}} \phi_0(\mathbf{r}) + \frac{1}{2\pi} \sum_{j=1}^{n_s} \frac{\sigma_j^{in} - \sigma_j^{out}}{\sigma_k^{in} + \sigma_k^{out}} \oint_{S_j} \phi(\mathbf{r}') \frac{\mathbf{r}' - \mathbf{r}}{|\mathbf{r}' - \mathbf{r}|^3} d\mathbf{S}', \quad (2.15)$$

where σ_i^{in} and σ_i^{out} are the conductivities of the regions located to the interior and exterior of surface S_i , respectively, σ_0 is the conductivity of the medium in which the dipole is located, ϕ_0 is the electric potential caused by a dipole at \mathbf{r}_0 if it were in an infinite medium of conductivity σ_0 , and $d\mathbf{S}'$ is the differential area vector oriented normal to the surface [73]. Because each surface in the head model is actually a mesh of triangles, the surface integrals in (2.15) can be replaced by a summation of surface integrals over the area of each triangle. The surface integral for each triangle can then be evaluated by making an assumption about the value of the electric potential across the each triangle. Typically, the potential is assumed to either be constant or have linear or quadratic variation over each triangle [73].

The system of algebraic equations resulting from (2.15) has the form

$$\mathbf{v} = \mathbf{v}_0 + \mathbf{B}\mathbf{v}, \quad (2.16)$$

where \mathbf{v} is a vector of the unknown electric potentials at the nodes, \mathbf{v}_0 is a vector of the electric potentials produced at the nodes from the current source alone, and \mathbf{B} is a square matrix whose elements are determined by the geometry and conductivity of the regions of the head model. It is easy to see that (2.16) can be rewritten in the same form as (2.14), such that

$$[\mathbf{I} - \mathbf{B}]\mathbf{v} = \mathbf{v}_0, \quad (2.17)$$

where \mathbf{I} is the identity matrix with the same dimensions as \mathbf{B} and $[\mathbf{I} - \mathbf{B}]$ is the system matrix. For BEM head models, the system matrix is typically a full matrix, meaning that iterative techniques are not very useful for solving the system of equations. Instead, direct methods, such as Gaussian elimination, are usually employed.

Like the spherical head models, most BEM head models just define three distinct regions: the scalp, skull, and brain. Typically, about 1000 nodes are used for each of the three boundaries in the model, including the air-scalp, the scalp-skull, and the skull-brain boundaries [9]. It has been shown that 500 nodes per shell is too coarse a resolution to get accurate results, whereas 1000 nodes per shell seems to produce satisfactory results [74]. While the accuracy of the BEM is roughly proportional to the number of nodes, this is limited by the quickly increasing computational demand to solve the system matrix [74].

Head models generated with the BEM are considered the most simplistic of numerical head volume conductors. Since the models are constructed from closed surfaces with regions of homogeneous isotropic conductivity, important features of real heads are left unaccounted, such as tissue discontinuities, tissue inhomogeneities, and anisotropic conductivities. With forward problem solutions being limited to a finite number of surfaces in the head, BEM head models are not very useful for accurately modeling electrical activity throughout the entire head volume. Additionally, since the system matrix is full, it is difficult to solve the system of equations efficiently. Direct methods of inverting the system matrix must be employed and are typically much less computationally efficient than iterative techniques.

2.8.2.2 Finite Difference Method

The FDM is one of the most well known and straightforward methods used to numerically solve partial differential equations. Consequently, FDM head models are a very common choice for solving the forward problem in EEG source analysis [18, 43, 49, 50, 52, 60, 76-81]. Unlike analytical or BEM head models, FDM head models are not just limited to using nested regions to represent the head. Instead, the entire head is partitioned into a regular grid of hexahedral volume elements, each of which can be assigned its own conductivity based on its particular tissue type. These volume elements, or voxels, are usually chosen to correspond to the position and size of the voxels in MR images. Hence, mesh generation for the FDM is extremely easy and the appropriate head volume information can be directly mapped from the medical image voxels. Discretizing Poisson's equation is accomplished by substituting all the partial derivatives with truncated Taylor series expansions. Thus, for every computational node there is an algebraic equation in which the partial derivatives are replaced by finite differences.

In the simplest of FDM head models, isotropic conductivity is assumed and scalar conductivity values are assigned to every voxel. In this case, the head is usually discretized with cubic voxels with side lengths of h and the computational nodes are chosen to be at the center of each voxel. Utilizing the box integration scheme [82], Poisson's equation and the boundary conditions are discretized to obtain algebraic equations for every node in the head model. For example, consider a node and its six neighboring nodes, as depicted in Figure 2.4. The linear equation for the electric potential at node 0 can be written as

$$\left(\sum_{i=1}^6 a_i \right) \phi_0 - \sum_{i=1}^6 a_i \phi_i = I, \quad (2.18)$$

where ϕ_i is the electric potential for node i , a_i correspond to the conductance between neighboring nodes, such that

$$a_i = 2h \cdot \frac{\sigma_0 \sigma_i}{\sigma_0 + \sigma_i}, \quad (2.19)$$

and I is the total current leaving the voxel, such that

$$I = \begin{cases} +I & \text{for a current source} \\ -I & \text{for a current sink} \\ 0 & \text{otherwise} \end{cases} \quad (2.20)$$

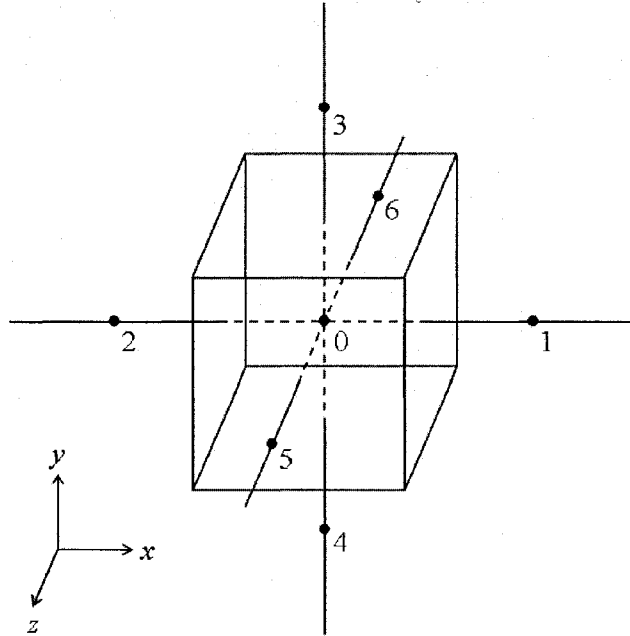


Figure 2.4: Node numbering used by the isotropic FDM head model.

In order to incorporate anisotropic conductivity, a more complicated FDM head model was introduced by Saleheen and Ng [81], and has subsequently been used by other research groups [60]. Extending the two-dimensional case presented by Asencor and Panizo [83], Saleheen and Ng [81] developed the FDM for inhomogeneous anisotropic media in three dimensions. In this anisotropic FDM head model, each voxel in the computational grid is assigned a conductivity tensor. Unlike the isotropic FDM head model, the computational nodes are chosen to be at the vertices of the voxels instead of the centers. While this allows for anisotropy to be incorporated into the head model, it does make the discretization of Poisson's equation more difficult. At the nodes, there is a discontinuity in the conductivity, which can normally be accounted for by applying the proper boundary conditions. However, the boundary normal direction is not well defined at the voxel vertices, making it difficult to apply the boundary conditions. As a result, the complicated "transition layer" technique [84] is employed to account for the discontinuities in the conductivity and derive the finite difference equations. The

resulting linear algebraic equation is similar to (2.18), except that the electric potential of a node is expressed as a linear combination of eighteen neighboring nodes instead of just six. A more detailed description of the derivation and the resulting algebraic equation is available in the literature [81].

Regardless of the type of conductivity used, applying the FDM to every node in the head model results in a linear set of algebraic equations with the same form as (2.14). Since the electric potential at every node can be expressed as a linear combination of only its neighboring nodes, the resultant system matrix is sparse. In the isotropic case there are no more than seven nonzero values per row in the system matrix, while in the anisotropic case there are no more than nineteen nonzero values per row. It can also be shown, that the system matrix is both symmetric and positive definite, which allows fast iterative methods, such as the PCG method, to be used to solve the system of equations. It should be noted that the current vector is also sparse, with nonzero values only occurring for nodes where there is a current source or sink.

The main benefit of the FDM is that realistic features of the head can be accounted for, such as tissue discontinuities, tissue inhomogeneities, and anisotropic conductivity. This gives FDM head models a distinct advantage over analytical head models and even BEM head models. The electric potential is calculated for the entire head volume, allowing more detailed knowledge of the electrical activity in the head, as opposed to just knowing what is happening at a finite number of surfaces in the head. In both the isotropic and anisotropic formulations, discrete changes or discontinuities in the conductivity between neighboring voxels are allowed. Since only rectangular grids are employed, there can be concerns related to how well the grid represents the true head geometry, especially around tissue boundaries with complicated shapes. And, while this can be somewhat remedied by using higher resolution head models, computational resources place a limit on the number of nodes that can be used.

2.8.2.3 Finite Element Method

The FEM is a numerical method that has been used to solve partial differential equations for many different applications, especially when the modeling of complicated geometries is a concern. With the complex tissue boundaries and distributions in the head, FEM head models are quite popular for solving the forward problem in EEG source analysis [17, 44,

45, 58, 59, 61-63, 85-91]. Similar to FDM head models, FEM head models partition the entire head into smaller volumes, creating a computational grid consisting of finite elements. While regular grids of hexahedrons are occasionally employed, it is more common for irregular grids of tetrahedrons to be used with FEM head models. Such computational grids provide geometric flexibility that allows for the head anatomy obtained from MR images to be more accurately modeled. Regardless of the grid that is used, the computational nodes are typically located at the vertices of the finite elements. Additionally, both isotropic and anisotropic conductivity can be accounted for by the FEM, with the appropriate conductivity value being assigned to every finite element in the head model.

In order to find the electric potential at every node, a number of different FEM approaches are possible. The two most common of these are Galerkin's weighted residual method and the Rayleigh-Ritz variational method [92]. Both methods reformulate Poisson's equation and substitute in an approximation for the electric potential in order to obtain a discrete equation. For example, Galerkin's method reformulates Poisson's equation by multiplying it by a weighting function, α , and then integrating it over the head volume, V , such that

$$\int_V \alpha \nabla \cdot (\boldsymbol{\sigma} \nabla \phi) dV = - \int_V \alpha I_v dV . \quad (2.21)$$

Then, using Green's first identity, the left hand side of (2.21) can be expressed as

$$\int_V \alpha \nabla \cdot (\boldsymbol{\sigma} \nabla \phi) dV = \oint_{\partial V} \alpha (\boldsymbol{\sigma} \nabla \phi) \cdot d\mathbf{S} - \int_V (\nabla \alpha) \cdot (\boldsymbol{\sigma} \nabla \phi) dV , \quad (2.22)$$

where ∂V is the surface of the head volume. Substituting (2.22) into (2.21) and applying boundary conditions (2.6) results in the "weak formulation" of the forward problem

$$\int_V (\nabla \alpha) \cdot (\boldsymbol{\sigma} \nabla \phi) dV = \int_V \alpha I_v dV . \quad (2.23)$$

Regardless of whether Galerkin's method or the Rayleigh-Ritz method is used, the next step for the FEM is converting the reformulated Poisson's equation into a discrete equation. In FEM head models, the unknown electric potential over the entire computational domain is approximated by

$$\phi(x, y, z) = \sum_{i=1}^N \phi_i \alpha_i(x, y, z), \quad (2.24)$$

where N is the number of nodes in the grid, ϕ_i is the electric potential at node i , and $\alpha_i(x, y, z)$ is a basis or shape function associated with node i . Basis functions are interpolating functions that have a value of zero outside of the finite elements connected to their corresponding node and they span the space of piecewise polynomial functions [92]. Furthermore, basis functions have the unique property that they are equal to one at their corresponding node and are equal to zero at all other nodes [92]. It should be noted that Galerkin's method is a specific case of the general method of weighted residuals and it uses weighting functions that are identical to the basis functions in (2.24). Substituting (2.24) into the reformulated version of Poisson's equation results in a system of algebraic equations with the same form as (2.14). Because the basis functions have local support, only neighboring nodes contribute to the electric potential at every node. Thus, the system matrix is sparse and is usually quite large, depending on the number of nodes in the grid. As with the FDM, the FEM system matrix can be shown to be both symmetric and positive definite, thus making the use of fast iterative solvers possible.

Head models generated with the FEM are very popular since they can accurately model realistic features of the head such as tissue discontinuities, tissue inhomogeneities, and anisotropic conductivity. Additionally, arbitrarily complex tissue geometries throughout the head volume can be more accurately modeled with the FEM than with other methods such as the FDM. While there are many positive aspects to FEM head models, there are some negatives. One of the main problems with FEM head models is determining how to best model a current dipole. This problem arises because the grids used by the FEM are, in general, irregular [90]. As a result of this, many different approaches have been proposed for modeling a dipole in FEM head models [59, 90, 91]. There does not seem to be a general consensus, however, the two most popular methods seem to be the direct approach and the subtraction approach [59]. Another problem with FEM head models has to do with actually generating the irregular grid. Setting up an optimal volume grid can be a challenging and, sometimes, time consuming task when compared to the regular grid used by FDM head models. In fact, dedicated algorithms

have been written just to generate optimal FEM computational grids. One of the benefits of using a regular grid is that conductivity tensors obtained with DTI can be directly mapped to the voxels in the head model. However, when irregular grids are used, as is the case with FEM head models, much more effort is required to determine what values should go where and may involve interpolating tensor values.

2.8.2.4 Finite Volume Method

The FVM was originally developed to solve partial differential equations for heat transfer and fluid flow applications [93], and it remains very popular in the field of computational fluid dynamics [46]. While the FVM is still not quite as common in electromagnetic applications, FVM head models have been used by several research groups for EEG source analysis [46-48, 94-100] and other related applications [101-105]. Like FDM and FEM head models, FVM head models partition the entire head into small volume elements. Theoretically, these voxels can be arbitrary shapes and sizes, providing the FVM with some geometric flexibility similar to the FEM. However, many of the head models in the literature use a regular grid with hexahedral voxels, similar to the FDM. This allows for a simple mapping of MRI data into the head model. Just as with the FDM and FEM, both isotropic and anisotropic conductivity can be accounted for by assigning the appropriate conductivity value to each voxel. However, nearly every FVM head model in the literature uses isotropic conductivities, with only one paper [94] using anisotropic conductivity.

Poisson's equation is discretized by integrating it over finite volumes called control volumes that surround each computational node [93]. The nodes are usually located at the center of the voxels, so in this case the control volumes and the voxels are identical in location and shape and there is no need to distinguish between the two. Integrating Poisson's equation over a control volume, V , results in

$$\int_V \nabla \cdot (\boldsymbol{\sigma} \nabla \phi) dV = - \int_V I_v dV, \quad (2.25)$$

which can be simplified into Gauss' law by applying the divergence theorem, such that

$$\oint_{\partial V} (\boldsymbol{\sigma} \nabla \phi) \cdot d\mathbf{S} = - \int_V I_v dV, \quad (2.26)$$

where ∂V is the surface of the control volume. The surface integral in (2.26) can be discretized as a sum of fluxes, or currents, through the surfaces of each control volume. And, because the current leaving a given control volume is identical to that entering the adjacent control volume, the FVM is conservative.

In the most common case of using a cubic grid, (2.26) can be rewritten as

$$\sum_{i=1}^6 (\boldsymbol{\sigma} \nabla \phi \cdot \mathbf{S})_i = - \int_V I_v dV, \quad (2.27)$$

where $(\boldsymbol{\sigma} \nabla \phi \cdot \mathbf{S})_i$ is the current through face i on the cube and \mathbf{S} is the face area vector, oriented normal to the surface. The only thing left to discretize in (2.27) is the gradient of the electric potential, $\nabla \phi$, on the faces of the control volume. There are two ways that this can be accomplished: using either the differential or integral definition of the gradient. With the differential definition of the gradient, finite differences are used to approximate the gradient. This is basically the same idea as with the FDM since the partial derivatives are substituted with truncated Taylor series expansions. With the integral definition of the gradient, the gradient theorem is used to derive an expression for the gradient across a closed surface, such that

$$\nabla \phi = \frac{1}{V} \oint_S \phi d\mathbf{S}, \quad (2.28)$$

where V is the volume of the closed surface S . The surface integral in (2.28) can be discretized as a summation over the faces of the surface, such that

$$\nabla \phi = \frac{1}{V} \sum_i \phi_i \mathbf{S}_i, \quad (2.29)$$

where ϕ_i is the electric potential on face i and \mathbf{S}_i is the face area vector for face i . This method was employed in [46] and has the advantage over the differential form of the gradient in that it imposes fewer restrictions on the smoothness of the computational grid [46]. It should be noted that on a regular hexahedral grid, both the differential and integral definition of the gradient result in the same algebraic equation. Therefore, the resulting discrete version of Poisson's equation on a cubic grid with isotropic conductivity is the same as (2.18) for the isotropic FDM head model.

For all variants of FVM head models presented in the literature, the system of algebraic equations is in the exact same form as (2.14). As with the FDM and FEM, the FVM system matrix is sparse due to the fact that only neighboring nodes contribute to the equation for a particular node's electric potential. Additionally, the system matrix can be shown to be both symmetric and positive definite. All these properties of the system matrix allow for fast iterative solvers to be used to solve the forward problem.

Head models generated with the FVM may not currently be as popular as their FDM and FEM counterparts, but they share many of the same features that make them ideal for modeling heads. FVM head models are able to accurately model realistic features of the head such as tissue discontinuities, tissue inhomogeneities, and anisotropic conductivity. Additionally, since integral equations are employed, the FVM is a naturally conservative numerical method. This is sometimes considered the most attractive feature of the FVM [93]. Current is conserved such that Gauss' law is exactly satisfied for each control volume and over the entire computational domain [93]. And, this feature of the FVM exists for any grid resolution, not just in the limiting case when the number of grid points becomes very large [93]. As was the case with a cubic grid and isotropic conductivity, the FVM can sometimes result in the same algebraic equations as the FDM. While both numerical methods are very similar, the FVM benefits from having a more physics oriented approach to discretizing partial differential equations. Thus, in addition to providing a discrete version of Poisson's equation, the FVM also allows for a more intuitive understanding of the algebraic terms and how they relate to the electrical activity of the head. While the FVM is not limited to rectangular grids, it is quite common for such grids to be used out of convenience. These regular grids with hexahedral voxels allow for direct mapping of MRI data, such as conductivity tensors, into the head model. Thus, it is possible to eliminate some reliance on image segmentation to generate numerical head models. As well, when irregular grids are employed, a considerable amount of effort and time can be expended just to generate an optimal grid. With rectangular grids, the grid can simply be chosen to be the same as in the source MR images.

While the FVM has many desirable features, there does not seem to be a FVM head model for EEG source analysis that incorporates anisotropy and uses a rectangular

grid. Only one example of an anisotropic FVM head model seems to exist in the literature, and it used an irregular grid with tetrahedral voxels [94]. Additionally, generalized anisotropy was not used by this head model, since it employed conductivity tensors with anisotropy only in the radial and tangential directions. With the advantages of FVM head models previously mentioned, it seems like an anisotropic FVM head model using a regular grid of hexahedrons would be a valuable contribution to the field of EEG source analysis. Such a model has been developed in the work presented in the following chapters.

2.9 Inverse Problem

In EEG source analysis, the inverse problem involves characterizing a current source from measured EEG scalp potentials. For the case of a single equivalent dipole model, this means determining the current source's location, orientation, and magnitude. Lead field analysis using reciprocity is an efficient way to determine the best fit current source for the EEG measurements. Both lead field analysis and reciprocity will be discussed in greater detail in the following sections.

2.9.1 Lead Field Analysis

Lead field analysis is a technique used to solve the inverse problem in EEG source analysis. Central to the concept of lead field analysis is the lead field matrix (LFM), which defines the relationship between current sources at discrete locations and the electric potentials at the scalp electrodes [106]. Determining the LFM is a prerequisite for solving the inverse problem, and it is equivalent to solving the forward problem for each possible dipole location and orientation. While there are a seemingly limitless number of possible dipole orientations, the principle of superposition allows any single dipole to be represented as a linear combination of three mutually orthogonal dipoles. Thus, the forward problem need only be evaluated for three mutually orthogonal orientations at each dipole location.

The LFM is calculated column-by-column in an iterative fashion, solving each of the required forward problems and filling the LFM columns with the electrode potentials. Figure 2.5 provides a visual representation of the LFM structure for the case when there are M electrodes and N possible dipole locations. As indicated, the indices of the rows

correspond to the electrodes on the scalp, while the indices of the columns correspond to the dipole locations and orientations. For example, the column labeled i_x corresponds to a dipole at location i and oriented in the x -direction. Once the LFM is calculated, a dipole localization algorithm is used to determine the location and orientation that results in electric potentials that best fit the measured EEG scalp potentials. While there are a variety of different dipole localization algorithms, one of the more commonly used ones is the well-known MUSIC (MUltiple Signal Classification) algorithm. For the case of a single equivalent dipole model, the MUSIC algorithm involves a least squares fitting and an exhaustive search of the solution space to find the dipole that best accounts for the measured EEG scalp potentials. Full details of the MUSIC algorithm and its application to the inverse problem can be found in the literature [107, 108].

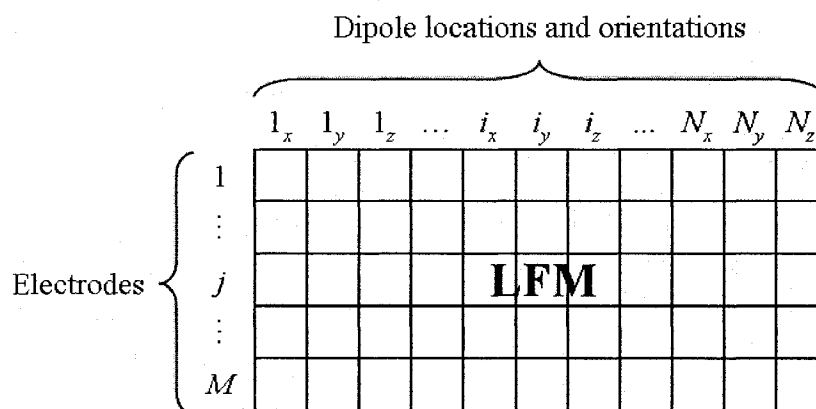


Figure 2.5: Visual representation of the lead field matrix.

One of the benefits of using lead field analysis is that the LFM only depends on the head model and the electrode configuration. Therefore, once the LFM is generated, it can be used repeatedly with any dipole localization method to localize any number of sources from different EEG scalp potentials. Unfortunately, generating the LFM in the first place can be an extremely time consuming process. Head models can have anywhere from several hundred thousand nodes up to several million nodes, depending on the resolution of the computational grid. Since the forward problem must be solved for three dipole orientations at up to several million locations, it seems obvious that generating the LFM can quickly become the limiting factor in performing lead field analysis. One way to deal with this problem is to restrict the inverse problem's solution space by reducing

the number of possible dipole locations used in the LFM. Therefore, fewer forward problem solutions are required to generate the LFM. Oftentimes this is accomplished by using *a priori* knowledge about the nature of the current source, including physiological and anatomical information so that the possible solutions make biological sense [15]. For example, EEG scalp potentials originate from the pyramidal cells, which are located within the cerebral cortex and are oriented perpendicular to the cortical surface. With this knowledge, the possible location and orientation of a current dipole in a head model can be limited. Other *a priori* knowledge sometimes comes from functional imaging techniques, such as functional MRI, which can be used to determine the active regions of the brain and limit the solution search to those regions. In addition to reducing the solution space, there is also an alternative method of calculating the LFM which is much more efficient. Using the reciprocity theorem, the time required to calculate the LFM can be drastically reduced.

2.9.2 Reciprocity

Reciprocity is an essential part of EEG source analysis that allows for the LFM to be constructed in a time efficient manor. Finding a solution to the inverse problem normally requires solving the forward problem for three mutually orthogonal dipole orientations at every possible dipole location in the head model. However, the reciprocity theorem can be exploited so that the number of forward problem solutions is reduced to just the number of electrodes being used. With no more than one hundred electrodes typically being used in EEG source analysis, the reciprocity theorem can easily reduce the amount of time required to construct the LFM.

The reciprocity theorem was first applied to EEG source analysis by Rush and Driscoll in 1969 [70], when they proved that reciprocity holds true for general inhomogeneous anisotropic conductors. The easiest way to understand the reciprocity theorem is to consider a general 2-port resistor network with ports AB and CD . If current I_{AB} is introduced at port AB , potential difference ϕ_{CD} is generated at port CD . Conversely, if current I_{CD} is introduced at port CD , potential difference ϕ_{AB} is generated at port AB . The reciprocity theorem then states that these currents and potential differences are related, such that

$$\phi_{AB} I_{AB} = \phi_{CD} I_{CD}. \quad (2.30)$$

While not identical to (2.30), a very similar relationship can be derived for the case when the reciprocity theorem is applied to EEG source analysis. In this case, the potential difference between electrodes A and B due to a current dipole, \mathbf{p} , at position \mathbf{r} , can be calculated if the electric potential $\phi(\mathbf{r})$ due to current I_{AB} between electrodes A and B is known. This can be expressed more concisely with the mathematical version of the reciprocity theorem, which states that

$$\phi_{AB}(\mathbf{r}, \mathbf{p}) = \frac{\mathbf{p}^T \cdot \nabla \phi(\mathbf{r})}{I_{AB}}. \quad (2.31)$$

Therefore, instead of calculating the electric potential at the electrodes for every possible dipole location and orientation, the LFM can be calculated simply by doing the opposite to this procedure. Placing a current sink at the reference electrode and a current source at each other electrode, the electric potential at any location in the head model can be calculated. Using the reciprocity theorem, the potential differences at the electrodes due to any dipole can easily be calculated. Essentially, this can be thought of as calculating the LFM row-by-row instead of column-by-column. For a more detailed description of lead field analysis using reciprocity, see the literature [52, 70, 106].

Chapter 3: Anisotropic Finite-Volume Head Model in 2D

The finite volume method (FVM) has many features that make it an attractive numerical method for electroencephalogram (EEG) source analysis. It is able to accurately model realistic features of the head, including tissue discontinuities and tissue inhomogeneities. The FVM is also a naturally conservative numerical method, with current being conserved and Gauss' Law being satisfied over the entire computational domain [93]. Compared to other numerical methods, the FVM benefits from having a more physics oriented approach to discretizing partial differential equations. This allows for an intuitive understanding of the algebraic terms and how they relate to the electrical activity of the head. Additionally, it is quite common with the FVM for the system matrix to be symmetric and positive definite. These properties in particular are very desirable since they allows for computationally efficient methods to be used to solve the system of equations. While the FVM does have many attractive features, there seems to be little to no mention in the literature of using anisotropic conductivity in FVM head models. Although the possibility of using anisotropic conductivity has been mentioned [46, 92], only one example of anisotropic FVM head model has been found in the literature [94] and it uses a complicated grid of triangular prisms. Consequently, it is felt that developing an anisotropic FVM head model would be a valuable contribution to the field of EEG source analysis.

In this chapter, two different methods of incorporating anisotropic conductivity into a FVM head model will be developed: a voxel-centered approach and a vertex-centered approach. The voxel-centered approach places the computational nodes at the voxel centers, while the vertex-centered approach places the computational nodes at the vertices of the voxels. For clarity, both are only presented in two dimensions here, but can easily be extended to three dimensions. The purpose of developing two different anisotropic FVM head models is to determine which one would be better suited to the purpose of EEG source analysis. With this in mind, both approaches are evaluated and compared based on their solutions to the forward problem as well as the amount of computer memory required to implement them. Based on this evaluation, the vertex-centered approach was ultimately chosen over the voxel-centered approach.

3.1 Head Model Development

In some previous studies [46], the FVM was developed within a generalized curvilinear coordinate system. While a curvilinear coordinate system offers flexibility in terms of voxel shape, the present work will be limited to the Cartesian coordinate system with strictly cubic voxels. In two dimensions this means that the voxels and control volumes are both two-dimensional square elements with dimensions of $h \times h$. Additionally, the conductivity tensor in two dimensions is represented by a symmetric 2×2 matrix, such that

$$\boldsymbol{\sigma} = \begin{bmatrix} \sigma^{xx} & \sigma^{xy} \\ \sigma^{xy} & \sigma^{yy} \end{bmatrix}. \quad (3.1)$$

There are two reasons for using this Cartesian voxel framework. First, non-rectangular grids may have geometric singularities, where voxels degenerate into a line or a point, that require special treatment [46]. Typically this means additional equations and unknowns are necessary, complicating the process of discretizing Poisson's equation. Second, setting up an irregular grid can be a challenging and, sometimes, time consuming task that may even require a dedicated algorithm. With a Cartesian grid the qualitative and quantitative head tissue properties can be directly mapped from the Cartesian grid used by the medical images. However, when irregular grids are used, much more effort is required to determine the mapping from medical images to the head model. This can be even more complicated when the mapping involves conductivity tensor values instead of just scalar values.

With a Cartesian coordinate system chosen, voxel-centered and vertex-centered approaches to the FVM were used to incorporate anisotropic conductivity into a head conductor model. The initial steps involved with both approaches are the same, starting with each side of Poisson's equation being integrated over the control volume, V , such that

$$-\int_V \nabla \cdot (\boldsymbol{\sigma} \nabla \phi) dV = \int_V I_v dV. \quad (3.2)$$

This is followed by the application of the divergence theorem to the left hand side of (3.2), which results in

$$-\oint_{\partial V} (\boldsymbol{\sigma} \nabla \phi) \cdot d\mathbf{S} = \int_V I_v dV. \quad (3.3)$$

At this point in the derivation the subsequent steps for the voxel-centered and vertex-centered approaches begin to differ. Therefore, detailed descriptions of the remaining steps involved in the development of both approaches are provided in the separate sections.

3.1.1 Voxel-Centered Approach

Motivation for the voxel-centered approach came from several sources [46, 96, 104] and it involves placing the computational nodes at the centers of the grid voxels. The two-dimensional computational grid used for the following derivation is depicted in Figure 3.1. Figure 3.1 (a) shows the voxel and node numbering convention, while Figure 3.1 (b) shows the labeling convention for locations on the control volume.

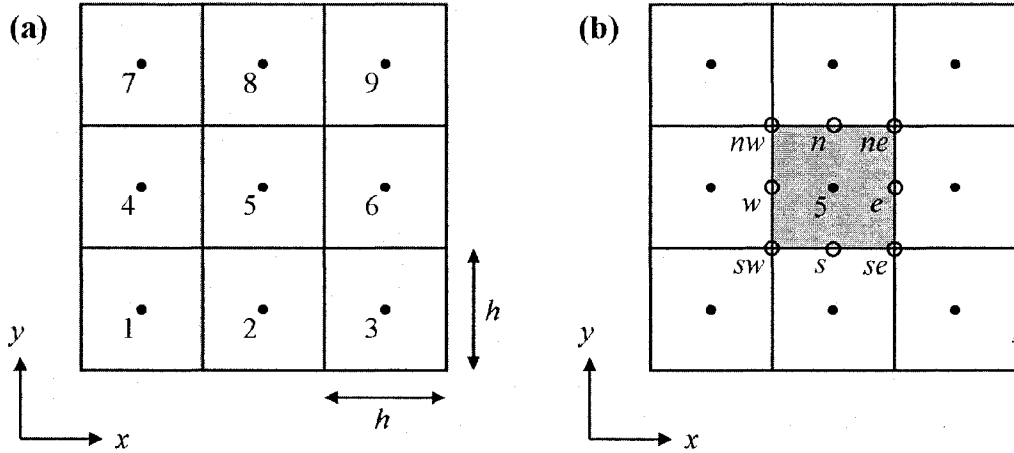


Figure 3.1: Computational grid for the 2D FVM voxel-centered approach. The (a) voxels and nodes are denoted by numbers 1 through 9 and the (b) control volume (shaded area) labeling convention is shown.

To discretize (3.3) for node 5, the current source density is assumed to be constant over the control volume and the surface integral can be evaluated for each face of the control volume such that

$$-\left((\boldsymbol{\sigma} \nabla \phi \cdot \mathbf{S}^x)_e - (\boldsymbol{\sigma} \nabla \phi \cdot \mathbf{S}^x)_w + (\boldsymbol{\sigma} \nabla \phi \cdot \mathbf{S}^y)_n - (\boldsymbol{\sigma} \nabla \phi \cdot \mathbf{S}^y)_s \right) = I_v h^2, \quad (3.4)$$

where \mathbf{S}^x and \mathbf{S}^y are the normal vectors for the faces of the control volume and are defined as

$$\mathbf{S}^x = \begin{bmatrix} h \\ 0 \end{bmatrix}, \quad (3.5)$$

$$\mathbf{S}^y = \begin{bmatrix} 0 \\ h \end{bmatrix}. \quad (3.6)$$

Each of the terms on the left hand side of (3.4) can be physically interpreted as the current flowing out of the faces of the control volume, while the term on the right hand side is the total source current, I , originating in the control volume. The left hand side terms in (3.4) can be discretized further by calculating the current flowing through each face of the control volume. As a sample calculation, the current flowing out through face e will be evaluated. This is done by first approximating the gradient at point e using finite differences, such that

$$\nabla \phi_e = \begin{bmatrix} (\phi_6 - \phi_5)/h \\ (\phi_{ne} - \phi_{se})/h \end{bmatrix}. \quad (3.7)$$

Therefore, substituting (3.7) into $(\sigma \nabla \phi \cdot \mathbf{S}^x)_e$ allows it to be simplified into

$$(\sigma \nabla \phi \cdot \mathbf{S}^x)_e = \begin{bmatrix} \sigma_e^{xx} & \sigma_e^{xy} \\ \sigma_e^{xy} & \sigma_e^{yy} \end{bmatrix} \begin{bmatrix} (\phi_6 - \phi_5)/h \\ (\phi_{ne} - \phi_{se})/h \end{bmatrix} \cdot \begin{bmatrix} h \\ 0 \end{bmatrix} = \sigma_e^{xx} (\phi_6 - \phi_5) + \sigma_e^{xy} (\phi_{ne} - \phi_{se}). \quad (3.8)$$

The electric potential at the corners of the control volume, ϕ_{ne} and ϕ_{se} , are not located at computational nodes but they can still be approximated, such that

$$\phi_{ne} = \frac{\phi_5 + \phi_6 + \phi_8 + \phi_9}{4}, \quad (3.9)$$

$$\phi_{se} = \frac{\phi_2 + \phi_3 + \phi_5 + \phi_6}{4}. \quad (3.10)$$

Then (3.8) can be further simplified using just the electric potential at computational nodes

$$(\boldsymbol{\sigma} \nabla \phi \cdot \mathbf{S}^x)_e = \sigma_e^{xx} (\phi_6 - \phi_5) + \frac{\sigma_e^{xy}}{4} [(\phi_8 + \phi_9) - (\phi_2 + \phi_3)]. \quad (3.11)$$

Since the conductivity tensors are defined as being piecewise constant over each voxel, the conductivity is not very well-defined along the faces of the voxels. As such, the value of the components of $\boldsymbol{\sigma}_e$ are not very well defined in (3.11). In order to define these values, knowledge of the Neumann boundary conditions is utilized, which specifies that current is continuous across face e . Using a similar technique as employed in [104], two non-overlapping “secondary cells” are defined and used to calculate the current on either side of face e , as shown in Figure 3.2.

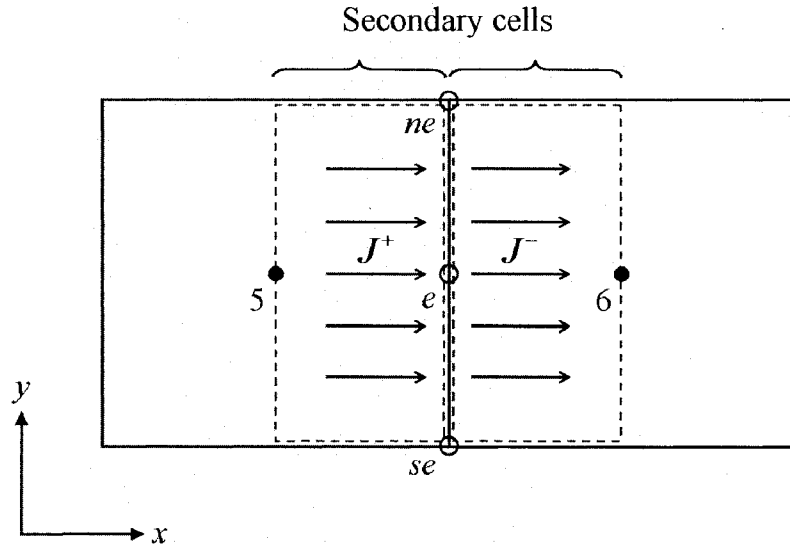


Figure 3.2: Secondary cells used for the 2D FVM voxel-centered approach. The secondary cells are indicated by the dashed lines and are used to calculate the current on either side of control volume face e .

The current on the left hand side of face e can be defined, such that

$$J^+ = \begin{bmatrix} \sigma_5^{xx} & \sigma_5^{xy} \\ \sigma_5^{xy} & \sigma_5^{yy} \end{bmatrix} \begin{bmatrix} (\phi_e - \phi_5)/(h/2) \\ (\phi_{ne} - \phi_{se})/h \end{bmatrix} \cdot \begin{bmatrix} h \\ 0 \end{bmatrix} = 2\sigma_5^{xx} (\phi_e - \phi_5) + \sigma_5^{xy} (\phi_{ne} - \phi_{se}), \quad (3.12)$$

while the current on the right hand side of face e can be defined similarly, such that

$$J^- = \begin{bmatrix} \sigma_6^{xx} & \sigma_6^{xy} \\ \sigma_6^{xy} & \sigma_6^{yy} \end{bmatrix} \begin{bmatrix} (\phi_6 - \phi_e)/(h/2) \\ (\phi_{ne} - \phi_{se})/h \end{bmatrix} \cdot \begin{bmatrix} h \\ 0 \end{bmatrix} = 2\sigma_6^{xx} (\phi_6 - \phi_e) + \sigma_6^{xy} (\phi_{ne} - \phi_{se}). \quad (3.13)$$

Since current is continuous across face e , then $J^+ = J^-$, implying that

$$2\sigma_5^{xx}(\phi_e - \phi_5) + \sigma_5^{xy}(\phi_{ne} - \phi_{se}) = 2\sigma_6^{xx}(\phi_6 - \phi_e) + \sigma_6^{xy}(\phi_{ne} - \phi_{se}). \quad (3.14)$$

Rearranging (3.14) to solve for ϕ_e results in

$$\phi_e = \frac{\sigma_5^{xx}\phi_5 + \sigma_6^{xx}\phi_6 + \frac{1}{2}(\sigma_6^{xy} - \sigma_5^{xy})(\phi_{ne} - \phi_{se})}{\sigma_5^{xx} + \sigma_6^{xx}}. \quad (3.15)$$

Therefore, (3.15) can now be substituted into either of (3.12) or (3.13) since the Neumann boundary conditions specify that $J^+ = J^- = (\boldsymbol{\sigma}\nabla\phi \cdot \mathbf{S}^x)_e$. The result of this is

$$(\boldsymbol{\sigma}\nabla\phi \cdot \mathbf{S}^x)_e = \frac{2\sigma_5^{xx}\sigma_6^{xx}}{\sigma_5^{xx} + \sigma_6^{xx}}(\phi_6 - \phi_5) + \frac{\sigma_5^{xx}\sigma_6^{xy} + \sigma_6^{xx}\sigma_5^{xy}}{\sigma_5^{xx} + \sigma_6^{xx}}(\phi_{ne} - \phi_{se}). \quad (3.16)$$

As before, ϕ_{ne} and ϕ_{se} can be approximated using (3.9) to obtain an expression similar to (3.11)

$$(\boldsymbol{\sigma}\nabla\phi \cdot \mathbf{S}^x)_e = \frac{2\sigma_5^{xx}\sigma_6^{xx}}{\sigma_5^{xx} + \sigma_6^{xx}}(\phi_6 - \phi_5) + \frac{\sigma_5^{xx}\sigma_6^{xy} + \sigma_6^{xx}\sigma_5^{xy}}{4(\sigma_5^{xx} + \sigma_6^{xx})}[(\phi_8 + \phi_9) - (\phi_2 + \phi_3)]. \quad (3.17)$$

Using the same reasoning employed for face e , similar expressions can be developed for the current through each other face of the control volume. The current through the faces of the control volume can thus be written as

$$-\oint_{\partial V} (\boldsymbol{\sigma}\nabla\phi) \cdot d\mathbf{S} = - \left\{ \begin{array}{l} \sigma_{52}^{yy}(\phi_2 - \phi_5) + \frac{\sigma_{52}^{yx}}{4}[(\phi_1 + \phi_4) - (\phi_3 + \phi_6)] \\ + \sigma_{54}^{xx}(\phi_4 - \phi_5) + \frac{\sigma_{54}^{xy}}{4}[(\phi_1 + \phi_2) - (\phi_7 + \phi_8)] \\ + \sigma_{56}^{xx}(\phi_6 - \phi_5) + \frac{\sigma_{56}^{xy}}{4}[(\phi_8 + \phi_9) - (\phi_2 + \phi_3)] \\ + \sigma_{58}^{yy}(\phi_8 - \phi_5) + \frac{\sigma_{58}^{yx}}{4}[(\phi_9 + \phi_6) - (\phi_7 + \phi_4)] \end{array} \right\}, \quad (3.18)$$

where simple expressions for the conductivity values have been used for clarity and are defined as

$$\sigma_{52}^{yy} = \frac{2\sigma_2^{yy}\sigma_5^{yy}}{\sigma_2^{yy} + \sigma_5^{yy}}, \quad (3.19)$$

$$\sigma_{52}^{yx} = \frac{\sigma_2^{yy}\sigma_5^{xy} + \sigma_5^{yy}\sigma_2^{xy}}{\sigma_2^{yy} + \sigma_5^{yy}}, \quad (3.20)$$

$$\sigma_{54}^{xx} = \frac{2\sigma_4^{xx}\sigma_5^{xx}}{\sigma_4^{xx} + \sigma_5^{xx}}, \quad (3.21)$$

$$\sigma_{54}^{xy} = \frac{\sigma_4^{xx}\sigma_5^{xy} + \sigma_5^{xx}\sigma_4^{xy}}{\sigma_4^{xx} + \sigma_5^{xx}}, \quad (3.22)$$

$$\sigma_{56}^{xx} = \frac{2\sigma_5^{xx}\sigma_6^{xx}}{\sigma_5^{xx} + \sigma_6^{xx}}, \quad (3.23)$$

$$\sigma_{56}^{xy} = \frac{\sigma_5^{xx}\sigma_6^{xy} + \sigma_6^{xx}\sigma_5^{xy}}{\sigma_5^{xx} + \sigma_6^{xx}}, \quad (3.24)$$

$$\sigma_{58}^{yy} = \frac{2\sigma_5^{yy}\sigma_8^{yy}}{\sigma_5^{yy} + \sigma_8^{yy}}, \quad (3.25)$$

$$\sigma_{58}^{yx} = \frac{\sigma_5^{yy}\sigma_8^{xy} + \sigma_8^{yy}\sigma_5^{xy}}{\sigma_5^{yy} + \sigma_8^{yy}}, \quad (3.26)$$

Rearranging (3.18) and substituting it into (3.4) results in the final discrete version of Poisson's equation using the voxel-centered approach

$$\left. \begin{aligned}
& - \left(\frac{\sigma_{52}^{yx} + \sigma_{54}^{xy}}{4} \right) \phi_1 - \left(\frac{\sigma_{52}^{yy} + \sigma_{54}^{xy} - \sigma_{56}^{xy}}{4} \right) \phi_2 \\
& + \left(\frac{\sigma_{52}^{yx} + \sigma_{56}^{xy}}{4} \right) \phi_3 - \left(\frac{\sigma_{54}^{xx} + \sigma_{52}^{yx} - \sigma_{58}^{yx}}{4} \right) \phi_4 \\
& \quad + \left(\frac{\sigma_{52}^{yy} + \sigma_{54}^{xx} + \sigma_{56}^{xx} + \sigma_{58}^{yy}}{4} \right) \phi_5 \\
& - \left(\frac{\sigma_{56}^{xx} - \sigma_{52}^{yx} + \sigma_{58}^{yx}}{4} \right) \phi_6 + \left(\frac{\sigma_{54}^{xy} + \sigma_{58}^{yx}}{4} \right) \phi_7 \\
& - \left(\frac{\sigma_{58}^{yy} - \sigma_{54}^{xy} + \sigma_{56}^{xy}}{4} \right) \phi_8 - \left(\frac{\sigma_{56}^{xy} + \sigma_{58}^{yx}}{4} \right) \phi_9
\end{aligned} \right\} = I. \quad (3.27)$$

3.1.2 Vertex-Centered Approach

Motivation for this approach came from numerous sources, with comparable numerical formulations having been applied to research areas such as modeling fluid flow in oil reservoir simulations [109-121]. As the name indicates, the vertex-centered approach places the computational nodes at the vertices of the voxels, as opposed to the voxel-centered approach, which places the nodes at the center of the voxels. The two-dimensional computational grid used for the following derivation is depicted in Figure 3.3. Figure 3.3 (a) shows the voxel labeling and node numbering convention, while Figure 3.3 (b) shows the labeling convention for locations on the control volume.

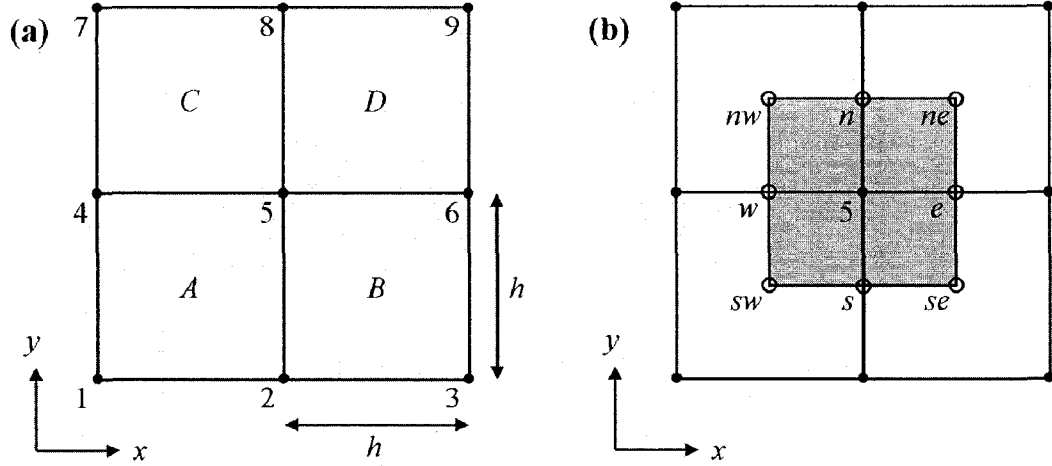


Figure 3.3: Computational grid for the 2D FVM vertex-centered approach. The (a) voxels are denoted by letters A through D and nodes are denoted by numbers 1 through 9 and the (b) control volume (shaded area) labeling convention is shown.

To discretize (3.3) for node 5, the current source density is assumed to be constant over the control volume and the surface integral can be evaluated for each face of the control volume such that

$$-\left(\left(\boldsymbol{\sigma}\nabla\phi\cdot\mathbf{S}^x\right)_e - \left(\boldsymbol{\sigma}\nabla\phi\cdot\mathbf{S}^x\right)_w + \left(\boldsymbol{\sigma}\nabla\phi\cdot\mathbf{S}^y\right)_n - \left(\boldsymbol{\sigma}\nabla\phi\cdot\mathbf{S}^y\right)_s\right) = I_v h^2 \quad (3.28)$$

where \mathbf{S}^x and \mathbf{S}^y are the normal vectors for the surface of the control volume and are defined as

$$\mathbf{S}^x = \begin{bmatrix} h \\ 0 \end{bmatrix}, \quad (3.29)$$

$$\mathbf{S}^y = \begin{bmatrix} 0 \\ h \end{bmatrix}. \quad (3.30)$$

As with the voxel-centered approach, each of the terms on the left hand side of (3.28) can be physically interpreted as the current flowing out of the faces of the control volume, while the term on the right hand side is the total source current, I , originating in the control volume. The left hand side terms in (3.28) can be discretized further by calculating the current flowing through each face of the control volume. As a sample calculation, the current flowing out through face e will be evaluated. To do this, the

current can first be split into a sum of two currents, one in voxel B and one in voxel D , as shown in Figure 3.4, such that

$$(\sigma \nabla \phi \cdot \mathbf{S}^x)_e = J_e^B + J_e^D = \sigma_B \nabla \phi_e^B \cdot \left(\frac{\mathbf{S}^x}{2} \right) + \sigma_D \nabla \phi_e^D \cdot \left(\frac{\mathbf{S}^x}{2} \right), \quad (3.31)$$

where J_e^B and J_e^D are the currents through face e in voxels B and D , respectively, and $\nabla \phi_e^B$ and $\nabla \phi_e^D$ are the electric potential gradients at point e in voxels B and D , respectively.

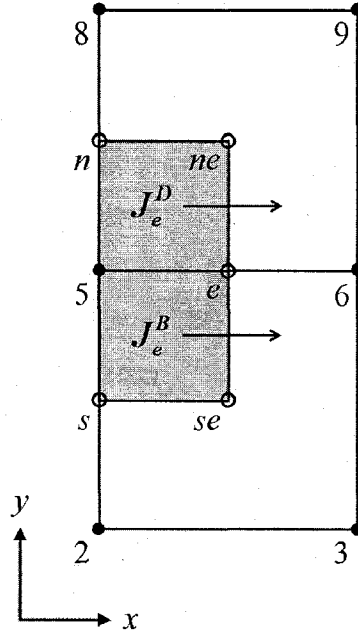


Figure 3.4: Current flow through a control volume face. The current can be split into two components through face e , one in voxel B and one in voxel D .

The gradients in (3.31) can be approximated using finite differences, such that

$$\nabla \phi_e^B = \begin{bmatrix} (\phi_6 - \phi_5)/h \\ (\phi_e - \phi_{se})/(h/2) \end{bmatrix}, \quad (3.32)$$

$$\nabla \phi_e^D = \begin{bmatrix} (\phi_6 - \phi_5)/h \\ (\phi_{ne} - \phi_e)/(h/2) \end{bmatrix}. \quad (3.33)$$

Expressions for the currents J_e^B and J_e^D can now be rewritten as

$$J_e^B = \begin{bmatrix} \sigma_B^{xx} & \sigma_B^{xy} \\ \sigma_B^{xy} & \sigma_B^{yy} \end{bmatrix} \begin{bmatrix} (\phi_6 - \phi_5)/h \\ (\phi_e - \phi_{se})/(h/2) \end{bmatrix} \cdot \begin{bmatrix} h/2 \\ 0 \end{bmatrix} = \frac{\sigma_B^{xx}}{2}(\phi_6 - \phi_5) + \sigma_B^{xy}(\phi_e - \phi_{se}), \quad (3.34)$$

$$J_e^D = \begin{bmatrix} \sigma_D^{xx} & \sigma_D^{xy} \\ \sigma_D^{xy} & \sigma_D^{yy} \end{bmatrix} \begin{bmatrix} (\phi_6 - \phi_5)/h \\ (\phi_{ne} - \phi_e)/(h/2) \end{bmatrix} \cdot \begin{bmatrix} h/2 \\ 0 \end{bmatrix} = \frac{\sigma_D^{xx}}{2}(\phi_6 - \phi_5) + \sigma_D^{xy}(\phi_{ne} - \phi_e). \quad (3.35)$$

Additionally, (3.34) and (3.35) can be further simplified by approximating the electric potentials ϕ_{ne} , ϕ_{se} , and ϕ_e as

$$\phi_{ne} = \frac{\phi_5 + \phi_6 + \phi_8 + \phi_9}{4}, \quad (3.36)$$

$$\phi_{se} = \frac{\phi_2 + \phi_3 + \phi_5 + \phi_6}{4}, \quad (3.37)$$

$$\phi_e = \frac{\phi_5 + \phi_6}{2}. \quad (3.38)$$

Therefore, (3.34) and (3.35) can be rewritten using (3.36), (3.37), and (3.38), such that

$$J_e^B = \frac{\sigma_B^{xx}}{2}(\phi_6 - \phi_5) + \frac{\sigma_B^{xy}}{4} [(\phi_5 + \phi_6) - (\phi_2 + \phi_3)], \quad (3.39)$$

$$J_e^D = \frac{\sigma_D^{xx}}{2}(\phi_6 - \phi_5) + \frac{\sigma_D^{xy}}{4} [(\phi_8 + \phi_9) - (\phi_5 + \phi_6)], \quad (3.40)$$

which results in a final expression for the current through face e

$$(\sigma \nabla \phi \cdot \mathbf{S}^x)_e = \left\{ \begin{array}{l} \frac{(\sigma_B^{xx} + \sigma_D^{xx})}{2}(\phi_6 - \phi_5) \\ + \frac{\sigma_B^{xy}}{4} [(\phi_5 + \phi_6) - (\phi_2 + \phi_3)] \\ + \frac{\sigma_D^{xy}}{4} [(\phi_8 + \phi_9) - (\phi_5 + \phi_6)] \end{array} \right\}. \quad (3.41)$$

Using the same reasoning employed for face e , similar expressions can be developed for the current through each other face of the control volume

$$(\boldsymbol{\sigma} \nabla \phi \cdot \mathbf{S}^x)_w = - \left\{ \begin{array}{l} \frac{(\sigma_A^{xx} + \sigma_C^{xx})}{2} (\phi_4 - \phi_5) \\ + \frac{\sigma_A^{xy}}{4} [(\phi_1 + \phi_2) - (\phi_4 + \phi_5)] \\ + \frac{\sigma_C^{xy}}{4} [(\phi_4 + \phi_5) - (\phi_7 + \phi_8)] \end{array} \right\}, \quad (3.42)$$

$$(\boldsymbol{\sigma} \nabla \phi \cdot \mathbf{S}^y)_n = \left\{ \begin{array}{l} \frac{(\sigma_C^{yy} + \sigma_D^{yy})}{2} (\phi_8 - \phi_5) \\ + \frac{\sigma_C^{xy}}{4} [(\phi_5 + \phi_8) - (\phi_4 + \phi_7)] \\ + \frac{\sigma_D^{xy}}{4} [(\phi_6 + \phi_9) - (\phi_5 + \phi_8)] \end{array} \right\}, \quad (3.43)$$

$$(\boldsymbol{\sigma} \nabla \phi \cdot \mathbf{S}^y)_s = - \left\{ \begin{array}{l} \frac{(\sigma_A^{yy} + \sigma_B^{yy})}{2} (\phi_2 - \phi_5) \\ + \frac{\sigma_A^{xy}}{4} [(\phi_1 + \phi_4) - (\phi_2 + \phi_5)] \\ + \frac{\sigma_B^{xy}}{4} [(\phi_2 + \phi_5) - (\phi_3 + \phi_6)] \end{array} \right\}. \quad (3.44)$$

Now, (3.41), (3.42), (3.43), and (3.44) can be used to rewrite (3.28), such that the final discrete form of Poisson's equation using the vertex-centered approach is

$$\left\{ \begin{array}{l} -\frac{1}{2} \sigma_A^{xy} \phi_1 - \frac{1}{2} (\sigma_A^{yy} + \sigma_B^{yy}) \phi_2 + \frac{1}{2} \sigma_B^{xy} \phi_3 - \frac{1}{2} (\sigma_A^{xx} + \sigma_C^{xx}) \phi_4 \\ + \frac{1}{2} \left(\sigma_A^{xx} + \sigma_B^{xx} + \sigma_C^{xx} + \sigma_D^{xx} + \sigma_A^{yy} + \sigma_B^{yy} \right) \phi_5 \\ - \frac{1}{2} (\sigma_B^{xx} + \sigma_D^{xx}) \phi_6 + \frac{1}{2} \sigma_C^{xy} \phi_7 - \frac{1}{2} (\sigma_C^{yy} + \sigma_D^{yy}) \phi_8 - \frac{1}{2} \sigma_D^{xy} \phi_9 \end{array} \right\} = I. \quad (3.45)$$

Using the properties of the coefficients, (3.45) can be written in a more compact form, such that

$$\sum_{\substack{i=1 \\ i \neq 5}}^9 A_i \phi_i - \left(\sum_{\substack{i=1 \\ i \neq 5}}^9 A_i \right) \phi_5 = I, \quad (3.46)$$

where the coefficients, A_i , are defined as

$$A_1 = -\frac{1}{2} \sigma_A^{xy}, \quad (3.47)$$

$$A_2 = -\frac{1}{2} (\sigma_A^{yy} + \sigma_B^{yy}), \quad (3.48)$$

$$A_3 = \frac{1}{2} \sigma_B^{xy}, \quad (3.49)$$

$$A_4 = -\frac{1}{2} (\sigma_A^{xx} + \sigma_C^{xx}), \quad (3.50)$$

$$A_6 = -\frac{1}{2} (\sigma_B^{xx} + \sigma_D^{xx}), \quad (3.51)$$

$$A_7 = \frac{1}{2} \sigma_C^{xy}, \quad (3.52)$$

$$A_8 = -\frac{1}{2} (\sigma_C^{yy} + \sigma_D^{yy}), \quad (3.53)$$

$$A_9 = -\frac{1}{2} \sigma_D^{xy}. \quad (3.54)$$

Upon evaluating the coefficients in (3.46), it can be seen that they are similar to those derived by the anisotropic finite difference method (FDM) in [81]. In fact, with some rearrangement of the equations, the vertex-centered approach's coefficients and the coefficients in [81] can be shown to be identical. This is important to note, since the anisotropic FDM has already been shown to have a good degree of accuracy [81]. Its accuracy was evaluated using the analytical solution to Laplace's equation for an inhomogeneous anisotropic cube. While an anisotropic cube obviously does not represent

a real head, the analytical solution allowed the numerical accuracy of the anisotropic FDM to be assessed. It is also important to note that the main difference between the vertex-centered approach and the anisotropic FDM is that the vertex-centered approach utilizes a considerably simpler derivation. Instead of using the complicated “transition layer” technique [84], the vertex-centered approach employs a much more physically intuitive derivation, allowing the algebraic terms to be understood with regards to the electrical activity that they represent.

3.2 Head Model Comparison

Since only one FVM approach is to be implemented in three dimensions, the voxel- and vertex-centered approaches must be evaluated and compared to determine which one is better suited to EEG source analysis. The two approaches are compared based on their solutions to the forward problem as well as the amount of computer memory required to implement them. These methods of comparison are described in more detail in the following section and it should be noted that all computer simulations are implemented on a desktop computer with a 3.2 GHz Pentium 4 processor and 2 GB of RAM.

3.2.1 Methods

Two different methods are used to compare the voxel- and vertex-centered approaches. The first method compares their solutions to the forward problem. Ideally, an analytical solution would be used as a “gold standard” to determine which approach’s forward problem solution is more accurate. However, since it has already been determined that the vertex-centered approach produces accurate results [81], the voxel-centered approach will be compared to the vertex-centered approach. The second method compares how efficient the voxel- and vertex-centered approaches are at using memory when implemented on a computer. The main culprit for using memory is the system matrix, since there are typically millions of computational nodes and their associated equations. As such, both the voxel- and vertex-centered approaches’ system matrices are evaluated to determine how efficient they are at using computer memory. The full details for both methods of comparison are provided below.

3.2.1.1 Forward Problem Solution

The forward problem is solved for a two-dimensional version of the three-shell spherical head model. For this circular head model, the radii of the shells are 9.2 cm, 8.6 cm, and 8.0 cm for the scalp, skull, and brain, respectively. With a current dipole located at the center of the head model and oriented in the positive x-direction, the voltages at every computational node within the head models are computed.

For the head model's conductivity, an isotropic case and three different anisotropic cases are used to compare the voxel- and vertex-centered approaches. For the isotropic case, a ratio of 1:1/15:1 is used for the scalp-to-skull-to-brain conductivity ratio [33]. For the anisotropic cases, only the skull and brain are made anisotropic with anisotropy ratios of 2:1, 5:1, and 10:1 for the skull's tangential-to-radial conductivity ratio and for the brain's radial-to-tangential conductivity ratio. In order to make valid comparisons between the isotropic and anisotropic cases, the volume constraint [59] is used to calculate the anisotropic conductivities of the skull and brain. The volume constraint retains the geometric mean of the tensor eigenvalues and, thus, the volume of the conductivity tensor ellipsoid. In two dimensions, this means the area of the conductivity tensor ellipse is retained, such that

$$\pi(\sigma_{\text{iso}})^2 = \pi\sigma_{\text{rad}}\sigma_{\text{tan}}, \quad (3.55)$$

where σ_{iso} is the isotropic conductivity and σ_{rad} and σ_{tan} are the anisotropic conductivities in the radial and tangential directions, respectively. The idea behind using the volume constraint is that each test case will contain equal amounts of total conductivity, and thus, the only difference is the directionality of the conductivity. Table 3.1 summarizes the conductivities used for each test case.

Table 3.1: Circular head model conductivities.

Anisotropy Ratio	Scalp Conductivity (S/m)		Skull Conductivity (S/m)		Brain Conductivity (S/m)	
	Radial	Tangential	Radial	Tangential	Radial	Tangential
1:1	0.300	0.300	0.0200	0.0200	0.300	0.300
2:1	0.300	0.300	0.0141	0.0283	0.424	0.212
5:1	0.300	0.300	0.00894	0.0447	0.671	0.134
10:1	0.300	0.300	0.00632	0.0632	0.949	0.0949

Since the voxel- and vertex-centered approaches have different node locations, special consideration must be paid when positioning the current dipole. In order to position the current dipole at the center of the head, there must be a node located at the center of the head model. For the voxel-centered approach this means that a voxel's center must be at the center of the head model. However, for the vertex-centered approach this means that a voxel's vertex must be at the center of the head model. Consequently, both approaches require slightly different grid resolutions to accommodate this dipole location. The voxel-centered approach uses a head model that is comprised of 183 voxels across its diameter, corresponding to a grid resolution of 1.005 mm and a total of 26317 nodes in the head model. The vertex-centered approach, however, uses a head model that is comprised of 184 voxels across its diameter, corresponding to a grid resolution of 1.000 mm and a total of 26981 nodes in the head model. With different grid resolutions and node locations, special consideration must also be paid when comparing the resulting voltage values. In order to evaluate the forward problem solution for the two different approaches, voltages at the same locations in the head model must be compared. Consequently, linear interpolation is used to calculate the vertex-centered voltages at the node locations of the voxel-centered head model.

Both the voxel- and vertex-centered approaches are implemented with MATLAB software. Before solving the forward problem, a reference potential is assigned to the node at the center of the head model. The forward problem is solved iteratively by MATLAB using the built-in iterative solvers. For the vertex-centered head model, the conjugate gradient (CG) method is used, whereas for the voxel-centered head model, the bi-conjugate gradient (BCG) method is used. The reason for this difference is that the

voxel-centered system matrix is not symmetric and the CG method requires a symmetric system matrix, but the BCG method does not.

The forward problem solutions for the voxel- and vertex-centered approaches are compared quantitatively using two error measures: the L2 relative error norm and the correlation coefficient. These error measures are chosen since they are commonly used in the EEG source analysis to evaluate head model performance [45, 62, 78, 85, 122]. The L2 relative error norm is defined as

$$\text{RE} = \frac{\|\phi^{\text{vox}} - \phi^{\text{vert}}\|_2}{\|\phi^{\text{vert}}\|_2} \times 100\%, \quad (3.56)$$

where ϕ^{vox} and ϕ^{vert} are the voltage values from the voxel- and vertex-centered approaches, respectively. The L2 relative error norm measures the agreement of the magnitude and shape of the two different sets of voltages, and is measured with respect to the vertex-centered voltages. A value of 0% for the L2 relative error norm indicates perfect agreement between the two sets of values. The correlation coefficient is defined as

$$\text{CC} = \frac{\sum_{i=1}^N (\phi_i^{\text{vert}} - \overline{\phi^{\text{vert}}}) (\phi_i^{\text{vox}} - \overline{\phi^{\text{vox}}})}{\sqrt{\left(\sum_{i=1}^N (\phi_i^{\text{vert}} - \overline{\phi^{\text{vert}}})^2\right) \left(\sum_{i=1}^N (\phi_i^{\text{vox}} - \overline{\phi^{\text{vox}}})^2\right)}}, \quad (3.57)$$

where $\overline{\phi^{\text{vox}}}$ and $\overline{\phi^{\text{vert}}}$ are the mean values of the voxel- and vertex-centered voltages, respectively, and N is the number of voltage values being compared. The correlation coefficient measures the agreement of the shape of the two different voltage distributions. A value of 1 for the correlation coefficient indicates perfect agreement between the two sets of values.

3.2.1.2 Memory Requirements

When deciding between the voxel- and vertex-centered approaches it is important to examine how efficiently each approach uses memory when implemented on a computer. When dealing with head models that consist on several million nodes, the amount of available memory and computational power on a computer becomes a primary concern.

The main culprit when it comes to using up memory is creating and loading the system matrix. As such, both the voxel- and vertex-centered approaches will be evaluated on the memory requirements for their system matrices.

While both approaches produce a large, sparse system matrix, they do have one major difference. The vertex-centered approach has a symmetric system matrix, while the voxel-centered approach does not. When a system matrix is symmetric it implies that the coefficient of node X in the equation for node Y should be the same as the coefficient of node Y in the equation for node X . For example, using the voxel-centered approach and the numbering convention in Figure 3.1, the coefficient for node 6 when evaluating node 5 is

$$A_{56} = -\left(\sigma_{56}^{xx} - \frac{\sigma_{52}^{yx}}{4} + \frac{\sigma_{58}^{yx}}{4}\right), \quad (3.58)$$

while the coefficient for node 5 when evaluating node 6 is

$$A_{65} = -\left(\sigma_{65}^{xx} + \frac{\sigma_{63}^{yx}}{4} - \frac{\sigma_{69}^{yx}}{4}\right). \quad (3.59)$$

It can be shown that $\sigma_{56}^{xx} = \sigma_{65}^{xx}$, but $-\sigma_{52}^{yx} + \sigma_{58}^{yx} \neq \sigma_{63}^{yx} - \sigma_{69}^{yx}$. Therefore, $A_{56} \neq A_{65}$ and the system matrix for the voxel-centered approach is not symmetric. Alternatively, using the vertex-centered approach and the labeling and numbering convention in Figure 3.3, the coefficient for node 6 when evaluating node 5 is

$$A_{56} = -\frac{1}{2}(\sigma_B^{xx} + \sigma_D^{xx}), \quad (3.60)$$

while the coefficient for node 5 when evaluating node 6 is

$$A_{65} = -\frac{1}{2}(\sigma_B^{xx} + \sigma_D^{xx}). \quad (3.61)$$

It is easy to see that $A_{56} = A_{65}$ and that the system matrix for the vertex-centered approach is symmetric.

3.2.2 Results

The results for the comparison of the voxel- and vertex-centered approaches are provided below. While the results of the forward problem solution provide a quantitative comparison of the two approaches, the results of the memory requirements are more qualitative in nature.

3.2.2.1 Forward Problem Solution

The results from the quantitative comparison of the voxel- and vertex-centered approaches are summarized in Table 3.2. In addition to the L2 relative error norm and the correlation coefficient, the maximum and minimum voltage values are also provided for both approaches in Table 3.2.

Table 3.2: Forward problem solution comparison for 2D FVM approaches.

Anisotropy Ratio	RE (%)	CC	Maximum Voltage (V)		Minimum Voltage (V)	
			Voxel-centered	Vertex-centered	Voxel-centered	Vertex-centered
1:1	0.80	1.0000	121.14	120.81	-121.14	-120.81
2:1	2.79	0.9997	131.69	130.95	-131.69	-130.95
5:1	15.27	0.9976	156.40	131.97	-156.40	-131.97
10:1	44.07	0.9947	187.90	124.73	-187.90	-124.73

After evaluating all the test cases, it can be observed that there is good agreement between the voxel- and vertex-centered approaches for the isotropic case and for the anisotropic case with an anisotropy ratio of 2:1. However, the agreement between the voxel- and vertex-centered approaches decreases considerably as the anisotropy ratio increases to 10:1. Overall, the trend of the data is that the L2 relative error norm increases and the correlation coefficient decreases for higher anisotropy ratios. Additionally, as the anisotropy ratio increases, it would appear that the agreement of the voltages' magnitude is more affected than the shape of the voltage distributions. The changes in the L2 relative error norm are fairly substantial, increasing from 0.80% for the isotropic case to 44.07% for the anisotropic case with an anisotropy ratio of 10:1. This increase in the L2 relative error norm corresponds to differences between peak voltages of 0.33 V for the isotropic case and 63.17 V for the anisotropic case with an anisotropy ratio of 10:1. The changes in the correlation coefficient, however, are less substantial than those for the L2

relative error norm. The correlation coefficient decreases from 1.0000 for the isotropic case to 0.9947 for the anisotropic case with an anisotropy ratio of 10:1. This decrease in the correlation coefficient corresponds to only a slight reduction in agreement of the shapes of the two different voltage distributions, as illustrated in Figure 3.5 and Figure 3.6. It should be noted that normalized voltages are used for Figure 3.5 and Figure 3.6 so that only the differences in the shape of the voltage distributions are shown and not differences in the voltage magnitudes.

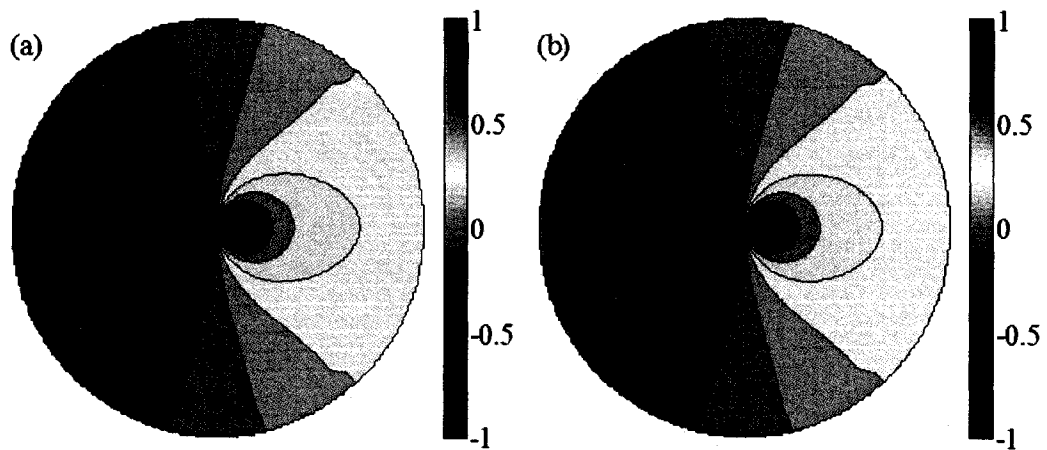


Figure 3.5: Normalized voltage contour plots for anisotropy ratio of 1:1. The voltages shown are for the (a) voxel- and (b) vertex-centered approaches.

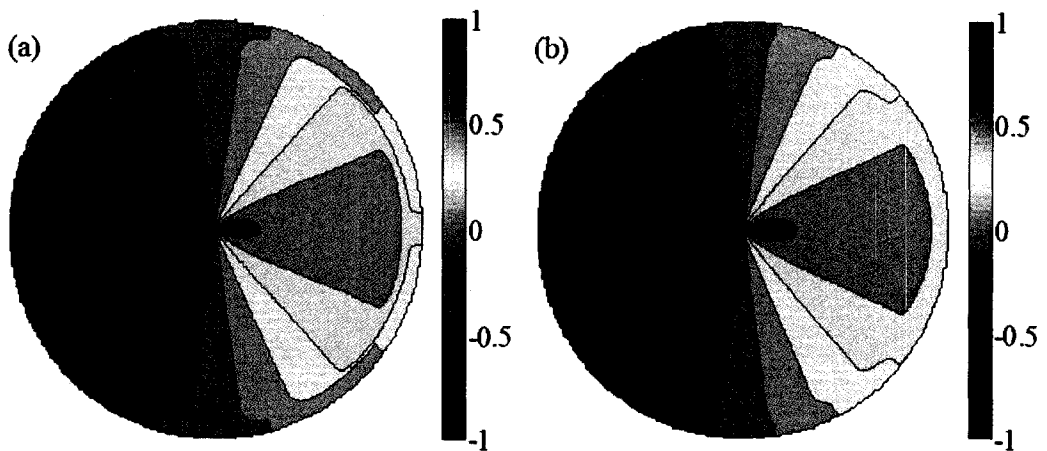


Figure 3.6: Normalized voltage contour plots for anisotropy ratio of 10:1. The voltages shown are for the (a) voxel- and (b) vertex-centered approaches.

3.2.2.2 Memory Requirements

With regards to memory requirements, the result of having a symmetric system matrix is easy to understand. For a symmetric system matrix, only the upper triangle of the matrix needs to be stored in memory, reducing the memory requirements by almost half when compared to a matrix that is not symmetric. For example, in the two-dimensional case presented for the voxel- and vertex-centered approaches there are nine coefficients per row of the system matrix. For the voxel-centered approach, every coefficient in every row must be stored in memory. However, for the vertex-centered approach, only five of the nine coefficients in each row need to be stored in memory due to the symmetry of the system matrix. Therefore, with the same amount of available memory, this means that almost double the number of equations, or double the grid resolution, can be implemented for the vertex-centered approach as opposed to the voxel-centered approach.

3.2.3 Discussion

The voxel- and vertex-centered approaches to the FVM were evaluated and compared in order to determine the more suitable head model to use for EEG source analysis. Quantitatively, the voxel-centered approach showed good agreement with the vertex-centered approach for anisotropy ratios of 1:1 and 2:1. However, the agreement between the voxel- and vertex-centered approaches decreases as the anisotropy ratio increases to 10:1; that is, the L2 relative error norm increases and the correlation coefficient decreases as the anisotropy ratio increases. While the correlation coefficient decreases as the anisotropy ratio increases, it only decreases from 1.0000 down to 0.9947 for anisotropy ratios of 1:1 and 10:1, respectively. As shown in Figure 3.5 and Figure 3.6, this drop in correlation coefficients seems to indicate that the shape of the voltage distributions remain in good agreement for all the test cases. Conversely, the L2 relative error norm increases from 0.80% up to 44.07% for anisotropy ratios of 1:1 and 10:1, respectively. With the shapes of the voltage distributions being in good agreement, it appears that the main reason for the decreasing agreement between the voxel- and vertex-centered approaches is due to a difference in the voltages' magnitude. This is further illustrated by the increasing difference between the maximum (and minimum) voltages for the voxel- and vertex-centered approaches.

It is expected that these results can be somewhat accounted for by the slight difference in the head models. With the voxel- and vertex-centered head models having slightly different resolutions, some amount of discrepancy between their voltage values is expected. However, it is not clear why there is such a large disagreement between the methods as the anisotropy ratio increases to 10:1. Since the vertex-centered approach has already been shown to produce accurate results [81], these quantitative results seem to indicate that the voxel-centered approach is less accurate than the vertex-centered approach. One possible explanation for this could be that the voxel-centered approach has some difficulty in accurately modeling the anisotropic conductivity.

Using a somewhat qualitative comparison, the voxel- and vertex-centered approaches were evaluated based on the memory requirements of their system matrices. The vertex-centered approach was shown to have a symmetric system matrix, while the voxel-centered approach does not. In terms of memory requirements, this means that the vertex-centered approach's system matrix will be much more memory efficient, requiring nearly half the amount of the memory when compared to the voxel-centered approach's system matrix. The implication of this is that the vertex-centered approach could potentially use a head model with double the grid resolution or double the number nodal equations. This gives the vertex-centered approach a distinct advantage over the voxel-centered approach since the accuracy of the FVM increases as the size of the voxels decreases.

Another consideration that should be made is that the preconditioned conjugate gradient (PCG) method is the preferred iterative solver since it has been shown to be very efficient in terms of both computational time and memory requirements [96, 97]. However, in order to use the PCG method the system matrix must be positive definite and symmetric. In terms of positive definiteness, both the voxel- and vertex-centered approaches are expected to have positive definite system matrices based on the physical nature of the system being modeled. And, using the built-in MATLAB function "eigs," both approaches were empirically found to have positive definite system matrices once the reference node was assigned. However, since the voxel-centered approach does not have a symmetric system matrix, it can not be solved by the PCG method. As with the memory requirements, this gives a distinct advantage to the vertex-centered approach.

Not only will the vertex-centered approach require less memory than the voxel-centered approach, but it will also be solved more quickly using the PCG method. While other iterative solvers, such as the BCG method, could be used to solve the voxel-centered approach, it is suspected that none of them will match the performance provided by the PCG method.

An additional argument can also be made for using the vertex-centered approach instead of the voxel-centered approach. The voxel-centered approach can be shown to have some difficulty when it comes to accurately modeling current flow at air-tissue boundaries in the head. This problem arises when the tissue at the air-tissue boundary is anisotropic and is related to the conductivity tensor off-diagonal terms. To remedy this problem, the tensor off-diagonal terms are simply ignored at any air-tissue boundary. This problem was not discussed previously since it was not an issue in the test cases where the only tissue at an air-tissue boundary was the isotropic scalp. While most air-tissue boundaries do occur between air and an isotropic tissue, it is imaginable that this problem could come into play in a real head.

While the quantitative results seem to indicate that the vertex-centered approach is more accurate than the voxel-centered approach, it is hard to ignore the very beneficial properties associated with the vertex-centered approach having a symmetric system matrix. Based on this and the additional arguments made, it seems that the vertex-centered approach should be considered the more suitable candidate for EEG source analysis. Consequently, the vertex-centered approach will be developed in three dimensions instead of the voxel-centered approach.

Chapter 4: Anisotropic Finite-Volume Head Model in 3D

As discussed in Chapter 3, the vertex-centered approach to developing a finite volume method (FVM) head model is more desirable than the voxel-centered approach. Consequently, in this chapter, the vertex-centered approach will be extended to three dimensions with the goal of developing a three-dimensional anisotropic FVM head model. In three dimensions, the voxels and control volumes are both three-dimensional cubic elements with dimensions of $h \times h \times h$. Additionally, the conductivity tensor in three dimensions is represented by a symmetric 3×3 matrix, such that

$$\boldsymbol{\sigma} = \begin{bmatrix} \sigma^{xx} & \sigma^{xy} & \sigma^{xz} \\ \sigma^{xy} & \sigma^{yy} & \sigma^{yz} \\ \sigma^{xz} & \sigma^{yz} & \sigma^{zz} \end{bmatrix}. \quad (4.1)$$

4.1 Head Model Development

Identical to the two-dimensional case, in three dimensions the head model development of the vertex-centered approach starts with each side of Poisson's equation being integrated over the control volume, V , such that

$$-\int_V \nabla \cdot (\boldsymbol{\sigma} \nabla \phi) dV = \int_V I_v dV. \quad (4.2)$$

This is followed by the application of the divergence theorem to the left hand side of (4.2), which results in

$$-\oint_{\partial V} (\boldsymbol{\sigma} \nabla \phi) \cdot d\mathbf{S} = \int_V I_v dV. \quad (4.3)$$

The three-dimensional computational grid and the node number convention used for the following derivation are depicted in Figure 4.1, while Figure 4.2 shows the voxel labeling convention for this grid.

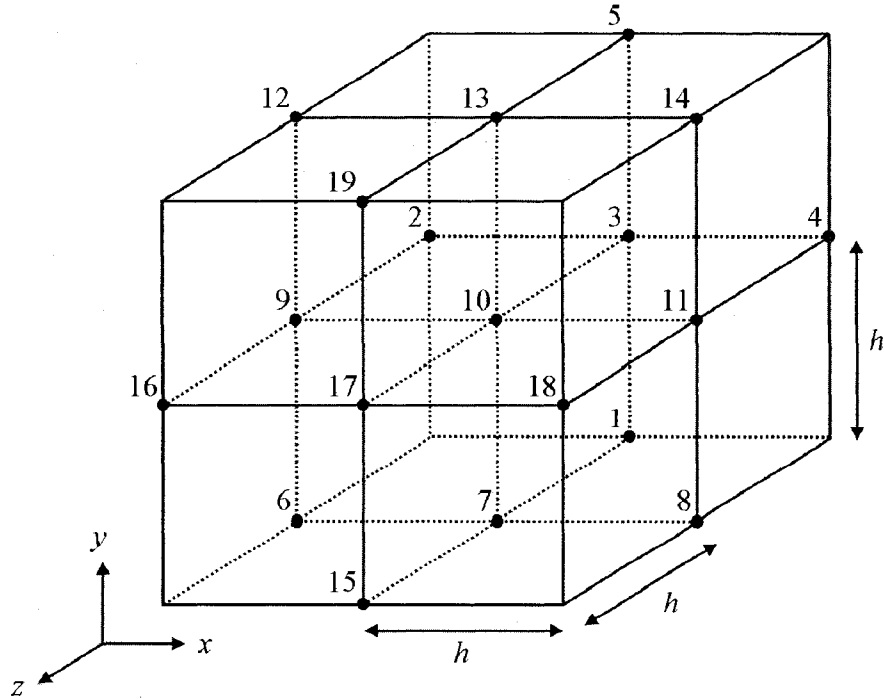


Figure 4.1: Node numbers for the 3D FVM computational grid.

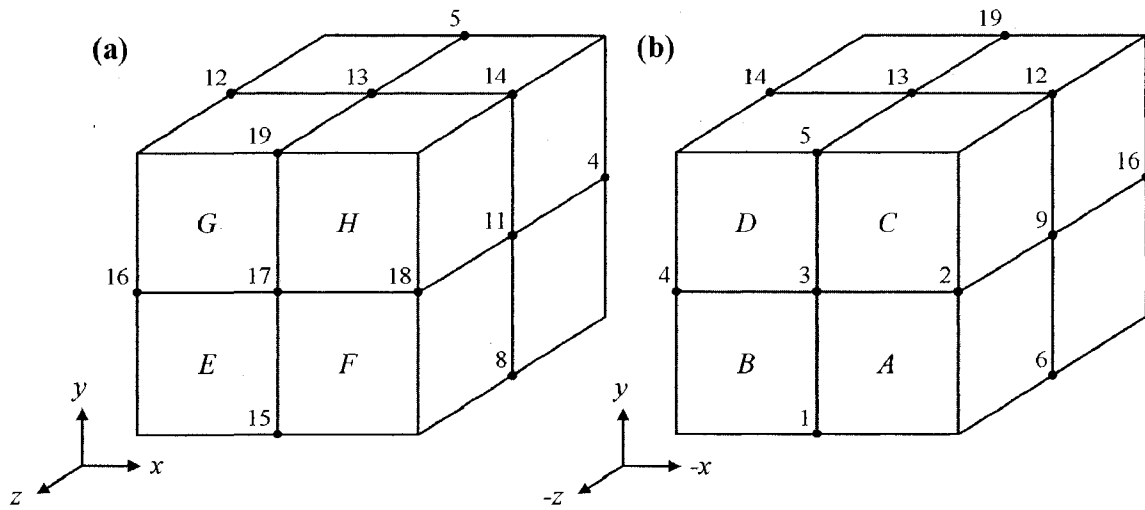


Figure 4.2: Voxel labels for the 3D FVM computational grid. The labels are shown for the (a) front and (b) back of the computational grid.

To discretize (4.3) for node 10, the current source density is assumed to be constant over the control volume and the surface integral can be evaluated for each face of the control volume such that

$$-\left\{ \begin{array}{l} (\sigma \nabla \phi \cdot \mathbf{S}^x)_{x^+} - (\sigma \nabla \phi \cdot \mathbf{S}^x)_{x^-} \\ + (\sigma \nabla \phi \cdot \mathbf{S}^y)_{y^+} - (\sigma \nabla \phi \cdot \mathbf{S}^y)_{y^-} \\ + (\sigma \nabla \phi \cdot \mathbf{S}^z)_{z^+} - (\sigma \nabla \phi \cdot \mathbf{S}^z)_{z^-} \end{array} \right\} = I_v h^3 \quad (4.4)$$

where x^+ , x^- , y^+ , y^- , z^+ , z^- are the faces of the control volume in the positive and negative x -, y -, and z -direction, and \mathbf{S}^x , \mathbf{S}^y , \mathbf{S}^z are the normal vectors for the surface of the control volume and are defined as

$$\mathbf{S}^x = \begin{bmatrix} h^2 \\ 0 \\ 0 \end{bmatrix}, \quad (4.5)$$

$$\mathbf{S}^y = \begin{bmatrix} 0 \\ h^2 \\ 0 \end{bmatrix}, \quad (4.6)$$

$$\mathbf{S}^z = \begin{bmatrix} 0 \\ 0 \\ h^2 \end{bmatrix}. \quad (4.7)$$

As with the vertex-centered approach in two dimensions, each of the terms on the left hand side of (4.4) can be physically interpreted as the current flowing out of the faces of the control volume, while the term on the right hand side is the total source current, I , originating in the control volume. The left hand side terms in (4.4) can be discretized further by calculating the current flowing through each face of the control volume. Unlike the derivation in two dimensions where the current is split into the sum of two currents, in three dimensions the current is split into the sum of four currents, since each control volume face consists of parts of four voxels. As a sample calculation, the current flowing out through face x^+ will be evaluated, with the labeling convention for locations on the control volume shown in Figure 4.3.

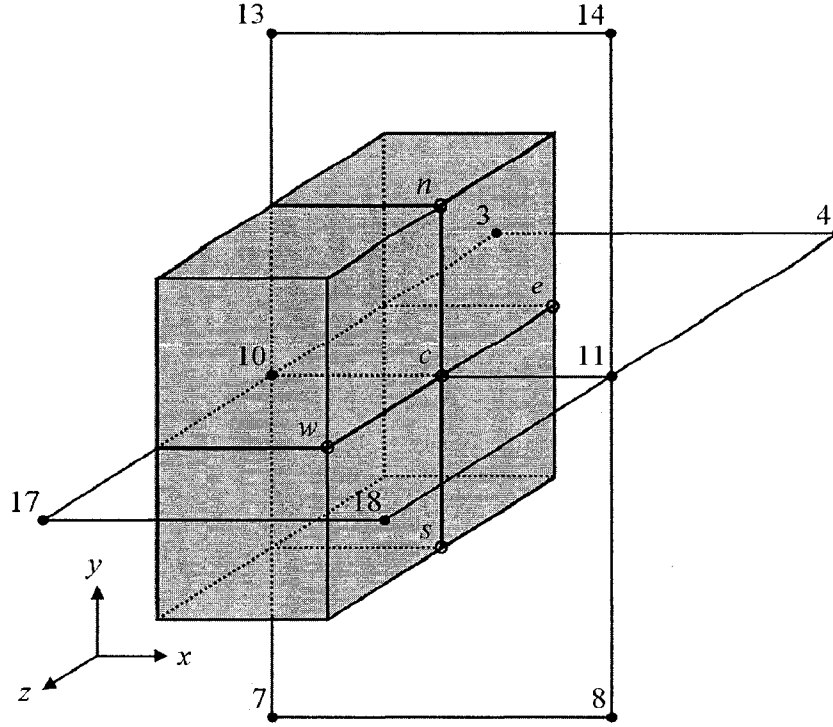


Figure 4.3: Labeling convention for a control volume face. The labels are shown for the x^+ face of the control volume.

The current through face x^+ is split into a sum of four currents, through voxel B , voxel D , voxel F , and voxel H , as shown in Figure 4.4, such that

$$(\sigma \nabla \phi \cdot \mathbf{S}^x)_{x^+} = \left\{ \begin{array}{l} J_{x^+}^B + J_{x^+}^D \\ + J_{x^+}^F + J_{x^+}^H \end{array} \right\} = \left\{ \begin{array}{l} \sigma_B \nabla \phi_c^B \cdot \left(\frac{\mathbf{S}^x}{4} \right) + \sigma_D \nabla \phi_c^D \cdot \left(\frac{\mathbf{S}^x}{4} \right) \\ + \sigma_F \nabla \phi_c^F \cdot \left(\frac{\mathbf{S}^x}{4} \right) + \sigma_H \nabla \phi_c^H \cdot \left(\frac{\mathbf{S}^x}{4} \right) \end{array} \right\}, \quad (4.8)$$

where $J_{x^+}^B$, $J_{x^+}^D$, $J_{x^+}^F$, and $J_{x^+}^H$ are the currents through face x^+ in voxels B , D , F , and H respectively, and $\nabla \phi_c^B$, $\nabla \phi_c^D$, $\nabla \phi_c^F$, and $\nabla \phi_c^H$ are the electric potential gradients at point c in voxels B , D , F , and H , respectively.

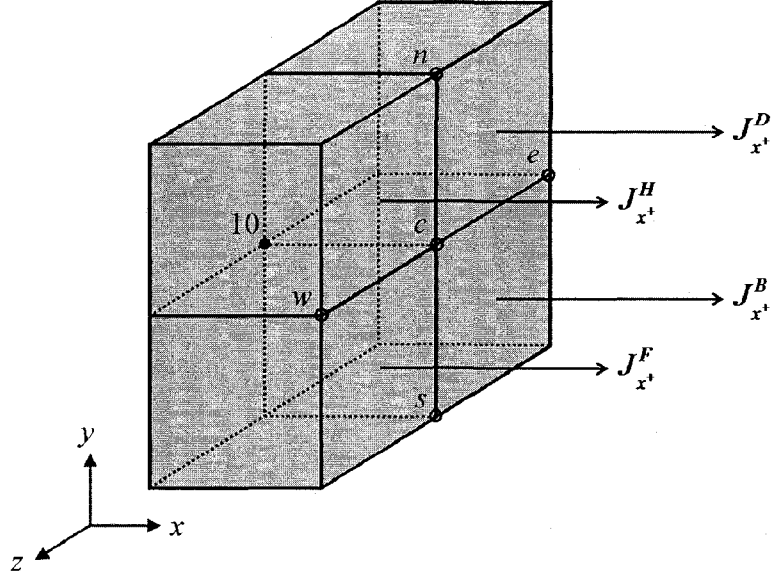


Figure 4.4: Current flow through a control volume face. The current can be split into four components through the x^+ face, one in voxel B , one in voxel D , one in voxel F , and one in voxel H .

The gradients in (4.8) can be approximated using finite differences, such that

$$\nabla \phi_c^B = \begin{bmatrix} (\phi_{11} - \phi_{10})/h \\ (\phi_c - \phi_s)/(h/2) \\ (\phi_c - \phi_e)/(h/2) \end{bmatrix}, \quad (4.9)$$

$$\nabla \phi_c^D = \begin{bmatrix} (\phi_{11} - \phi_{10})/h \\ (\phi_n - \phi_c)/(h/2) \\ (\phi_c - \phi_e)/(h/2) \end{bmatrix}, \quad (4.10)$$

$$\nabla \phi_c^F = \begin{bmatrix} (\phi_{11} - \phi_{10})/h \\ (\phi_c - \phi_s)/(h/2) \\ (\phi_w - \phi_c)/(h/2) \end{bmatrix}, \quad (4.11)$$

$$\nabla \phi_c^H = \begin{bmatrix} (\phi_{11} - \phi_{10})/h \\ (\phi_n - \phi_c)/(h/2) \\ (\phi_w - \phi_c)/(h/2) \end{bmatrix}. \quad (4.12)$$

Therefore, expressions for the currents $J_{x^+}^B$, $J_{x^+}^D$, $J_{x^+}^F$, and $J_{x^+}^H$ can now be rewritten as

$$\begin{aligned}
J_e^B &= \begin{bmatrix} \sigma_B^{xx} & \sigma_B^{xy} & \sigma_B^{xz} \\ \sigma_B^{xy} & \sigma_B^{yy} & \sigma_B^{yz} \\ \sigma_B^{xz} & \sigma_B^{yz} & \sigma_B^{zz} \end{bmatrix} \begin{bmatrix} (\phi_{11} - \phi_{10})/h \\ (\phi_c - \phi_s)/(h/2) \\ (\phi_c - \phi_e)/(h/2) \end{bmatrix} \begin{bmatrix} h^2/4 \\ 0 \\ 0 \end{bmatrix}, \\
&= \frac{h}{2} \left[\frac{\sigma_B^{xx}}{2} (\phi_{11} - \phi_{10}) + \sigma_B^{xy} (\phi_c - \phi_s) + \sigma_B^{xz} (\phi_c - \phi_e) \right]
\end{aligned} \tag{4.13}$$

$$\begin{aligned}
J_e^D &= \begin{bmatrix} \sigma_D^{xx} & \sigma_D^{xy} & \sigma_D^{xz} \\ \sigma_D^{xy} & \sigma_D^{yy} & \sigma_D^{yz} \\ \sigma_D^{xz} & \sigma_D^{yz} & \sigma_D^{zz} \end{bmatrix} \begin{bmatrix} (\phi_{11} - \phi_{10})/h \\ (\phi_n - \phi_c)/(h/2) \\ (\phi_c - \phi_e)/(h/2) \end{bmatrix} \begin{bmatrix} h^2/4 \\ 0 \\ 0 \end{bmatrix}, \\
&= \frac{h}{2} \left[\frac{\sigma_D^{xx}}{2} (\phi_{11} - \phi_{10}) + \sigma_D^{xy} (\phi_n - \phi_c) + \sigma_D^{xz} (\phi_c - \phi_e) \right]
\end{aligned} \tag{4.14}$$

$$\begin{aligned}
J_e^F &= \begin{bmatrix} \sigma_F^{xx} & \sigma_F^{xy} & \sigma_F^{xz} \\ \sigma_F^{xy} & \sigma_F^{yy} & \sigma_F^{yz} \\ \sigma_F^{xz} & \sigma_F^{yz} & \sigma_F^{zz} \end{bmatrix} \begin{bmatrix} (\phi_{11} - \phi_{10})/h \\ (\phi_c - \phi_s)/(h/2) \\ (\phi_w - \phi_c)/(h/2) \end{bmatrix} \begin{bmatrix} h^2/4 \\ 0 \\ 0 \end{bmatrix}, \\
&= \frac{h}{2} \left[\frac{\sigma_F^{xx}}{2} (\phi_{11} - \phi_{10}) + \sigma_F^{xy} (\phi_c - \phi_s) + \sigma_F^{xz} (\phi_w - \phi_c) \right]
\end{aligned} \tag{4.15}$$

$$\begin{aligned}
J_e^H &= \begin{bmatrix} \sigma_H^{xx} & \sigma_H^{xy} & \sigma_H^{xz} \\ \sigma_H^{xy} & \sigma_H^{yy} & \sigma_H^{yz} \\ \sigma_H^{xz} & \sigma_H^{yz} & \sigma_H^{zz} \end{bmatrix} \begin{bmatrix} (\phi_{11} - \phi_{10})/h \\ (\phi_n - \phi_c)/(h/2) \\ (\phi_w - \phi_c)/(h/2) \end{bmatrix} \begin{bmatrix} h^2/4 \\ 0 \\ 0 \end{bmatrix}, \\
&= \frac{h}{2} \left[\frac{\sigma_H^{xx}}{2} (\phi_{11} - \phi_{10}) + \sigma_H^{xy} (\phi_n - \phi_c) + \sigma_H^{xz} (\phi_w - \phi_c) \right]
\end{aligned} \tag{4.16}$$

Additionally, (4.13), (4.14), (4.15), and (4.16) can be further simplified by approximating the electric potentials ϕ_n , ϕ_s , ϕ_e , ϕ_w , and ϕ_c as

$$\phi_n = \frac{\phi_{10} + \phi_{11} + \phi_{13} + \phi_{14}}{4}, \tag{4.17}$$

$$\phi_s = \frac{\phi_7 + \phi_8 + \phi_{10} + \phi_{11}}{4}, \tag{4.18}$$

$$\phi_e = \frac{\phi_3 + \phi_4 + \phi_{10} + \phi_{11}}{4}, \tag{4.19}$$

$$\phi_w = \frac{\phi_{10} + \phi_{11} + \phi_{17} + \phi_{18}}{4}, \quad (4.20)$$

$$\phi_c = \frac{\phi_{10} + \phi_{11}}{2}. \quad (4.21)$$

Therefore, (4.13), (4.14), (4.15), and (4.16) can be rewritten using (4.17), (4.18), (4.19), (4.20), and (4.21), such that

$$J_e^B = \frac{h}{4} \left\{ \begin{array}{l} \sigma_B^{xx} (\phi_{11} - \phi_{10}) \\ + \frac{\sigma_B^{xy}}{2} [(\phi_{10} + \phi_{11}) - (\phi_7 + \phi_8)] \\ + \frac{\sigma_B^{xz}}{2} [(\phi_{10} + \phi_{11}) - (\phi_3 + \phi_4)] \end{array} \right\}, \quad (4.22)$$

$$J_e^D = \frac{h}{4} \left\{ \begin{array}{l} \sigma_D^{xx} (\phi_{11} - \phi_{10}) \\ + \frac{\sigma_D^{xy}}{2} [(\phi_{13} + \phi_{14}) - (\phi_{10} + \phi_{11})] \\ + \frac{\sigma_D^{xz}}{2} [(\phi_{10} + \phi_{11}) - (\phi_3 + \phi_4)] \end{array} \right\}, \quad (4.23)$$

$$J_e^F = \frac{h}{4} \left\{ \begin{array}{l} \sigma_F^{xx} (\phi_{11} - \phi_{10}) \\ + \frac{\sigma_F^{xy}}{2} [(\phi_{10} + \phi_{11}) - (\phi_7 + \phi_8)] \\ + \frac{\sigma_F^{xz}}{2} [(\phi_{17} + \phi_{18}) - (\phi_{10} + \phi_{11})] \end{array} \right\}, \quad (4.24)$$

$$J_e^H = \frac{h}{4} \left\{ \begin{array}{l} \sigma_H^{xx} (\phi_{11} - \phi_{10}) \\ + \frac{\sigma_H^{xy}}{2} [(\phi_{13} + \phi_{14}) - (\phi_{10} + \phi_{11})] \\ + \frac{\sigma_H^{xz}}{2} [(\phi_{17} + \phi_{18}) - (\phi_{10} + \phi_{11})] \end{array} \right\}, \quad (4.25)$$

which results in a final expression for the current through face x^+

$$(\sigma \nabla \phi \cdot \mathbf{S}^x)_{x^+} = \frac{h}{4} \left\{ \begin{aligned} & (\sigma_B^{xx} + \sigma_D^{xx} + \sigma_F^{xx} + \sigma_H^{xx})(\phi_{11} - \phi_{10}) \\ & + \frac{\sigma_B^{xy}}{2} [(\phi_{10} + \phi_{11}) - (\phi_7 + \phi_8)] + \frac{\sigma_B^{xz}}{2} [(\phi_{10} + \phi_{11}) - (\phi_3 + \phi_4)] \\ & + \frac{\sigma_D^{xy}}{2} [(\phi_{13} + \phi_{14}) - (\phi_{10} + \phi_{11})] + \frac{\sigma_D^{xz}}{2} [(\phi_{10} + \phi_{11}) - (\phi_3 + \phi_4)] \\ & + \frac{\sigma_F^{xy}}{2} [(\phi_{10} + \phi_{11}) - (\phi_7 + \phi_8)] + \frac{\sigma_F^{xz}}{2} [(\phi_{17} + \phi_{18}) - (\phi_{10} + \phi_{11})] \\ & + \frac{\sigma_H^{xy}}{2} [(\phi_{13} + \phi_{14}) - (\phi_{10} + \phi_{11})] + \frac{\sigma_H^{xz}}{2} [(\phi_{17} + \phi_{18}) - (\phi_{10} + \phi_{11})] \end{aligned} \right\} \quad (4.26)$$

Using the same reasoning employed for face x^+ , similar expressions can be developed for the current through each other face of the control volume

$$(\sigma \nabla \phi \cdot \mathbf{S}^x)_{x^-} = -\frac{h}{4} \left\{ \begin{aligned} & (\sigma_A^{xx} + \sigma_C^{xx} + \sigma_E^{xx} + \sigma_G^{xx})(\phi_9 - \phi_{10}) \\ & + \frac{\sigma_A^{xy}}{2} [(\phi_6 + \phi_7) - (\phi_9 + \phi_{10})] + \frac{\sigma_A^{xz}}{2} [(\phi_2 + \phi_3) - (\phi_9 + \phi_{10})] \\ & + \frac{\sigma_C^{xy}}{2} [(\phi_9 + \phi_{10}) - (\phi_2 + \phi_3)] + \frac{\sigma_C^{xz}}{2} [(\phi_2 + \phi_3) - (\phi_9 + \phi_{10})] \\ & + \frac{\sigma_E^{xy}}{2} [(\phi_6 + \phi_7) - (\phi_9 + \phi_{10})] + \frac{\sigma_E^{xz}}{2} [(\phi_9 + \phi_{10}) - (\phi_{16} + \phi_{17})] \\ & + \frac{\sigma_G^{xy}}{2} [(\phi_9 + \phi_{10}) - (\phi_{12} + \phi_{13})] + \frac{\sigma_G^{xz}}{2} [(\phi_9 + \phi_{10}) - (\phi_{16} + \phi_{17})] \end{aligned} \right\} \quad (4.27)$$

$$(\sigma \nabla \phi \cdot \mathbf{S}^y)_{y^+} = \frac{h}{4} \left\{ \begin{aligned} & (\sigma_C^{yy} + \sigma_D^{yy} + \sigma_G^{yy} + \sigma_H^{yy})(\phi_{13} - \phi_{10}) \\ & + \frac{\sigma_C^{xy}}{2} [(\phi_{10} + \phi_{13}) - (\phi_9 + \phi_{12})] + \frac{\sigma_C^{yz}}{2} [(\phi_{10} + \phi_{13}) - (\phi_3 + \phi_5)] \\ & + \frac{\sigma_D^{xy}}{2} [(\phi_{11} + \phi_{14}) - (\phi_{10} + \phi_{13})] + \frac{\sigma_D^{yz}}{2} [(\phi_{10} + \phi_{13}) - (\phi_3 + \phi_5)] \\ & + \frac{\sigma_G^{xy}}{2} [(\phi_{10} + \phi_{13}) - (\phi_9 + \phi_{12})] + \frac{\sigma_G^{yz}}{2} [(\phi_{17} + \phi_{19}) - (\phi_{10} + \phi_{13})] \\ & + \frac{\sigma_H^{xy}}{2} [(\phi_{11} + \phi_{14}) - (\phi_{10} + \phi_{13})] + \frac{\sigma_H^{yz}}{2} [(\phi_{17} + \phi_{19}) - (\phi_{10} + \phi_{13})] \end{aligned} \right\} \quad (4.28)$$

$$(\sigma \nabla \phi \cdot \mathbf{S}^y)_{y^-} = -\frac{h}{4} \left\{ \begin{aligned} & (\sigma_A^{yy} + \sigma_B^{yy} + \sigma_E^{yy} + \sigma_F^{yy})(\phi_7 - \phi_{10}) \\ & + \frac{\sigma_A^{xy}}{2} [(\phi_6 + \phi_9) - (\phi_7 + \phi_{10})] + \frac{\sigma_A^{yz}}{2} [(\phi_1 + \phi_3) - (\phi_7 + \phi_{10})] \\ & + \frac{\sigma_B^{xy}}{2} [(\phi_7 + \phi_{10}) - (\phi_8 + \phi_{11})] + \frac{\sigma_B^{yz}}{2} [(\phi_1 + \phi_3) - (\phi_7 + \phi_{10})] \\ & + \frac{\sigma_E^{xy}}{2} [(\phi_6 + \phi_9) - (\phi_7 + \phi_{10})] + \frac{\sigma_E^{yz}}{2} [(\phi_7 + \phi_{10}) - (\phi_{15} + \phi_{17})] \\ & + \frac{\sigma_F^{xy}}{2} [(\phi_7 + \phi_{10}) - (\phi_8 + \phi_{11})] + \frac{\sigma_F^{yz}}{2} [(\phi_7 + \phi_{10}) - (\phi_{15} + \phi_{17})] \end{aligned} \right\}, \quad (4.29)$$

$$(\sigma \nabla \phi \cdot \mathbf{S}^z)_{z^+} = \frac{h}{4} \left\{ \begin{aligned} & (\sigma_E^{zz} + \sigma_F^{zz} + \sigma_G^{zz} + \sigma_H^{zz})(\phi_{17} - \phi_{10}) \\ & + \frac{\sigma_E^{xz}}{2} [(\phi_{10} + \phi_{17}) - (\phi_9 + \phi_{16})] + \frac{\sigma_E^{yz}}{2} [(\phi_{10} + \phi_{17}) - (\phi_7 + \phi_{15})] \\ & + \frac{\sigma_F^{xz}}{2} [(\phi_{11} + \phi_{18}) - (\phi_{10} + \phi_{17})] + \frac{\sigma_F^{yz}}{2} [(\phi_{10} + \phi_{17}) - (\phi_7 + \phi_{15})] \\ & + \frac{\sigma_G^{xz}}{2} [(\phi_{10} + \phi_{17}) - (\phi_9 + \phi_{16})] + \frac{\sigma_G^{yz}}{2} [(\phi_{13} + \phi_{19}) - (\phi_{10} + \phi_{17})] \\ & + \frac{\sigma_H^{xz}}{2} [(\phi_{11} + \phi_{18}) - (\phi_{10} + \phi_{17})] + \frac{\sigma_H^{yz}}{2} [(\phi_{13} + \phi_{19}) - (\phi_{10} + \phi_{17})] \end{aligned} \right\}, \quad (4.30)$$

$$(\sigma \nabla \phi \cdot \mathbf{S}^z)_{z^-} = -\frac{h}{4} \left\{ \begin{aligned} & (\sigma_A^{zz} + \sigma_B^{zz} + \sigma_C^{zz} + \sigma_D^{zz})(\phi_3 - \phi_{10}) \\ & + \frac{\sigma_A^{xz}}{2} [(\phi_2 + \phi_9) - (\phi_3 + \phi_{10})] + \frac{\sigma_A^{yz}}{2} [(\phi_1 + \phi_7) - (\phi_3 + \phi_{10})] \\ & + \frac{\sigma_B^{xz}}{2} [(\phi_3 + \phi_{10}) - (\phi_4 + \phi_{11})] + \frac{\sigma_B^{yz}}{2} [(\phi_1 + \phi_7) - (\phi_3 + \phi_{10})] \\ & + \frac{\sigma_C^{xz}}{2} [(\phi_2 + \phi_9) - (\phi_3 + \phi_{10})] + \frac{\sigma_C^{yz}}{2} [(\phi_3 + \phi_{10}) - (\phi_5 + \phi_{13})] \\ & + \frac{\sigma_D^{xz}}{2} [(\phi_3 + \phi_{10}) - (\phi_4 + \phi_{11})] + \frac{\sigma_D^{yz}}{2} [(\phi_3 + \phi_{10}) - (\phi_5 + \phi_{13})] \end{aligned} \right\}. \quad (4.31)$$

Now, (4.26), (4.27), (4.28), (4.29), (4.30), and (4.31) can be used to rewrite (4.4), such that the final discrete form of Poisson's equation is

$$\sum_{\substack{i=1 \\ i \neq 10}}^{19} A_i \phi_i - \left(\sum_{\substack{i=1 \\ i \neq 10}}^{19} A_i \right) \phi_{10} = \frac{I}{h}, \quad (4.32)$$

where the coefficients, A_i , are defined as

$$A_1 = -\frac{1}{4}(\sigma_A^{yz} + \sigma_B^{yz}), \quad (4.33)$$

$$A_2 = -\frac{1}{4}(\sigma_A^{xz} + \sigma_C^{xz}), \quad (4.34)$$

$$A_3 = -\frac{1}{4}(\sigma_A^{zz} + \sigma_B^{zz} + \sigma_C^{zz} + \sigma_D^{zz}), \quad (4.35)$$

$$A_4 = \frac{1}{4}(\sigma_B^{xz} + \sigma_D^{xz}), \quad (4.36)$$

$$A_5 = \frac{1}{4}(\sigma_C^{yz} + \sigma_D^{yz}), \quad (4.37)$$

$$A_6 = -\frac{1}{4}(\sigma_A^{xy} + \sigma_E^{xy}), \quad (4.38)$$

$$A_7 = -\frac{1}{4}(\sigma_A^{yy} + \sigma_B^{yy} + \sigma_E^{yy} + \sigma_F^{yy}), \quad (4.39)$$

$$A_8 = \frac{1}{4}(\sigma_B^{xy} + \sigma_F^{xy}), \quad (4.40)$$

$$A_9 = -\frac{1}{4}(\sigma_A^{xx} + \sigma_C^{xx} + \sigma_E^{xx} + \sigma_G^{xx}), \quad (4.41)$$

$$A_{11} = -\frac{1}{4}(\sigma_B^{xx} + \sigma_D^{xx} + \sigma_F^{xx} + \sigma_H^{xx}), \quad (4.42)$$

$$A_{12} = \frac{1}{4}(\sigma_C^{xy} + \sigma_G^{xy}), \quad (4.43)$$

$$A_{13} = -\frac{1}{4}(\sigma_C^{yy} + \sigma_D^{yy} + \sigma_G^{yy} + \sigma_H^{yy}), \quad (4.44)$$

$$A_{14} = -\frac{1}{4}(\sigma_D^{xy} + \sigma_H^{xy}), \quad (4.45)$$

$$A_{15} = \frac{1}{4}(\sigma_E^{yz} + \sigma_F^{yz}), \quad (4.46)$$

$$A_{16} = \frac{1}{4}(\sigma_E^{xz} + \sigma_G^{xz}), \quad (4.47)$$

$$A_{17} = -\frac{1}{4}(\sigma_E^{zz} + \sigma_F^{zz} + \sigma_G^{zz} + \sigma_H^{zz}), \quad (4.48)$$

$$A_{18} = -\frac{1}{4}(\sigma_F^{xz} + \sigma_H^{xz}), \quad (4.49)$$

$$A_{19} = -\frac{1}{4}(\sigma_G^{yz} + \sigma_H^{yz}). \quad (4.50)$$

4.2 System Matrix Properties

Applying (4.32) to every node in a head model results in a finite system of algebraic equations that can be expressed in matrix form, such that

$$\mathbf{A}\mathbf{v} = \mathbf{i}, \quad (4.51)$$

where \mathbf{A} is an $N \times N$ system (or stiffness) matrix, \mathbf{v} is an $N \times 1$ vector containing the approximate electric potentials, \mathbf{i} is an $N \times 1$ vector containing the current source terms, and N is the number of computational nodes in the head model. Based on knowledge of the equations that help to establish (4.51), several properties of the system matrix can be determined. Familiarity with the system matrix properties helps to further characterize the system being modeled and also aids in determining appropriate methods to solve the system.

One system matrix property can be determined by considering the boundary conditions. Since a reference potential must be assigned, this implies that the system

matrix is rank deficient by one; that is, $\text{rank}(\mathbf{A}) = N - 1$. However, once a reference potential is assigned to any computational node in the head model, the system matrix will be full rank. With potentially millions of computational nodes in a head model, the system matrix is very large. However, since there are no more than nineteen nonzero elements per row, it is also very sparse. It can also be noted that each row in the system matrix sums to zero such that for any row i

$$\sum_{j=1}^N A_{ij} = 0. \quad (4.52)$$

It is reasonable to assume that the system matrix properties that were proven in the two-dimensional case are also true for the three-dimensional case. As such, the system matrix is both symmetric and positive definite. While the same proof for symmetry can be applied in the three-dimensional case, no definitive proof is available to establish that the system matrix is positive definite. For the two-dimensional case, it was shown empirically that the system matrix is positive definite, once a reference potential is assigned. Unfortunately, this same empirical method is not possible for the three-dimensional case. Due to the size of the system matrix and the amount of available memory, the built-in MATLAB function “eigs” could not be implemented. However, based on the physical nature of the system being modeled, the system matrix should be positive definite.

Chapter 5: Head Model Validation

All numerical head models have some error inherently associated with them due to the fact that they are approximations. Consequently, it is important to quantify this error before using a head model for electroencephalogram (EEG) source analysis and ensure that it produces accurate results. Analytical spherical head models are predominantly used for this validation process, serving as the “gold standard” when evaluating the accuracy of numerical models. In this chapter, an anisotropic three-shell spherical head is modeled with the anisotropic finite volume method (FVM). Solutions to the forward and inverse problems are calculated with the numerical head model and are compared to the solutions obtained with the analytical head model [67, 68]. This will allow the modeling error associated with the anisotropic FVM to be assessed.

5.1 Methods

There are primarily two ways to validate a numerical head model using the analytical solution: comparing either the forward problem solution or the inverse problem solution to that obtained with the analytical head model. Both of these methods will be used to evaluate the accuracy of the anisotropic FVM. In the case of the forward problem solution, the surface voltage error will be used to quantify the agreement between the FVM head model and the analytical head model. For the inverse problem solution, the source localization error will be used to quantify the agreement. Calculation details of the forward and inverse problem solutions are provided below along with details of the validation experiments and the error metrics.

5.1.1 Forward Problem Solution

The forward problem involves calculating the electric potential generated by a known current source at any point in the head. The finite system of algebraic equations for N computational nodes can be expressed as

$$\mathbf{A}\mathbf{v} = \mathbf{i}, \quad (5.1)$$

where \mathbf{A} is the $N \times N$ system matrix, \mathbf{v} is the $N \times 1$ electric potential vector, and \mathbf{i} is the $N \times 1$ current vector. The coefficients for the system matrix are calculated according

to (4.32), the governing equation for the anisotropic FVM. In order to solve the system of equations the system matrix must be inverted, such that

$$\mathbf{v} = \mathbf{A}^{-1} \mathbf{i}. \quad (5.2)$$

However, due to the fact that there are millions of nodes, directly inverting the system matrix in a time efficient manner is not possible, even with the most powerful desktop computers. Consequently, the inverse of the system matrix is never actually calculated and the preconditioned conjugate gradient (PCG) method is used to iteratively solve the system of equations. In this section, details of some of the procedures involved in the forward problem solution will be presented. These include descriptions of the conjugate gradient (CG) method, deflating the system matrix, and preconditioning the system matrix.

5.1.1.1 Conjugate Gradient Method

The CG method is chosen to solve the system of equations because of its well known convergence properties and because of its previous success in solving systems based on the FVM [96, 97]. For a positive-definite symmetric matrix, the CG method will converge to the correct solution using no more iterations than the dimension of the system matrix itself [96, 97]. However, in practice, iterations of the CG method are only done until the mean squared difference between the left and right side of (5.1) is below some tolerance value (or relative residual), ε , such that

$$\|\mathbf{A}\mathbf{v}_n - \mathbf{i}\|_2 < \varepsilon \quad (5.3)$$

where \mathbf{v}_n is the intermediate solution at iteration n . Using (5.3) as a stopping criterion considerably fewer iterations are required to reach convergence and, in practice, an upper limit is usually placed on the number of iterations. The iterations of the CG method begin with an initial estimate of the solution, $\mathbf{v}_0 = 0$. With a specified relative residual, ε , and a maximum iteration count, k_{\max} , the pseudo-code for the CG method is as follows:

$$\mathbf{r}_0 = \mathbf{i} - \mathbf{A}\mathbf{v}_0$$

$$\mathbf{d}_0 = \mathbf{r}_0$$

FOR $k = 0$ to k_{\max}

$$\alpha_k = \frac{\mathbf{r}_k^T \mathbf{r}_k}{\mathbf{d}_k^T \mathbf{A} \mathbf{d}_k}$$

$$\mathbf{v}_{k+1} = \mathbf{v}_k + \alpha_k \mathbf{d}_k$$

$$\mathbf{r}_{k+1} = \mathbf{r}_k - \alpha_k \mathbf{A} \mathbf{d}_k$$

$$\beta_{k+1} = \frac{\mathbf{r}_{k+1}^T \mathbf{r}_{k+1}}{\mathbf{r}_k^T \mathbf{r}_k}$$

$$\mathbf{d}_{k+1} = \mathbf{r}_{k+1} + \beta_{k+1} \mathbf{d}_k$$

IF $\|\mathbf{A}\mathbf{v}_{k+1} - \mathbf{i}\|_2 < \varepsilon$ THEN

EXIT

END IF

END FOR

5.1.1.2 Matrix Deflation

Matrix deflation is a term used to describe the process of making the system matrix full rank. This is required for the anisotropic FVM since its system matrix is rank deficient by one. Thinking of this in physical terms, matrix deflation simply means that a reference potential is assigned to one of the computational nodes. The actual process of matrix deflation involves removing the reference node's row and column from \mathbf{A} and the corresponding element from \mathbf{v} and \mathbf{i} . As a simple example, assume that the reference potential occurs at computational node 1 and has a value of c , such that $\phi_1 = c$. In this case, the original system, $\mathbf{A}\mathbf{v} = \mathbf{i}$, can be modified such that the deflated system is

$$\mathbf{A}_d \mathbf{v}_d = \mathbf{i}_d, \quad (5.4)$$

where

$$\mathbf{A}_d = \begin{bmatrix} A_{22} & \cdots & A_{2N} \\ \vdots & \ddots & \vdots \\ A_{N2} & \cdots & A_{NN} \end{bmatrix}, \quad (5.5)$$

$$\mathbf{v}_d = \begin{bmatrix} v_2 \\ \vdots \\ v_N \end{bmatrix}, \quad (5.6)$$

$$\mathbf{i}_d = \begin{bmatrix} i_2 \\ \vdots \\ i_N \end{bmatrix} - c \begin{bmatrix} A_{21} \\ \vdots \\ A_{N1} \end{bmatrix}. \quad (5.7)$$

It should be noted that while any value may be chosen for the reference potential, the most common choice of a reference potential is zero.

5.1.1.3 Matrix Preconditioning

A parameter that largely influences the effectiveness of the CG method is the condition number of the system matrix. The condition number is defined as the ratio of the largest eigenvalue to the smallest eigenvalue. The closer the condition number is to a value of one, the faster the iterative process converges. Consequently, the goal of matrix preconditioning is to improve a matrix's condition number prior to or during the process of solving the system of equations in hopes of reducing the number of iterations required by the CG method to reach convergence. The main idea behind matrix preconditioning is to solve (5.1) indirectly by solving

$$\tilde{\mathbf{A}}\tilde{\mathbf{v}} = \tilde{\mathbf{i}}. \quad (5.8)$$

The new system matrix and vectors are defined as

$$\tilde{\mathbf{A}} = \mathbf{C}_L \mathbf{A} \mathbf{C}_R, \quad (5.9)$$

$$\tilde{\mathbf{v}} = \mathbf{C}_R^{-1} \mathbf{v}, \quad (5.10)$$

$$\tilde{\mathbf{i}} = \mathbf{C}_L \mathbf{i}, \quad (5.11)$$

where C_L and C_R are the left and right preconditioning matrices, respectively. While there are many options when it comes to choosing a preconditioning matrix, there is no one preconditioning matrix that is useful for all situations. It has been previously determined [96, 97] that two preconditioning methods are particularly suitable for the large system matrix generated by the FVM in EEG source analysis: Jacobi preconditioning and polynomial preconditioning with Chebyshev polynomials.

5.1.1.3.1 Jacobi Preconditioning

Jacobi preconditioning is the simplest preconditioning method and is considered a symmetric method since it has equal left and right preconditioning matrices, $C_L = C_R = \mathbf{J}$. The Jacobi preconditioning matrix, \mathbf{J} , is a diagonal matrix with elements defined by

$$J_{kk} = \frac{1}{\sqrt{A_{kk}}}, \quad (5.12)$$

where A_{kk} are the diagonal elements of the system matrix, \mathbf{A} .

After matrix deflation is complete, Jacobi preconditioning is applied by computing $\tilde{\mathbf{A}}$ and $\tilde{\mathbf{i}}$, such that

$$\tilde{\mathbf{A}} = \mathbf{J}\mathbf{A}_d\mathbf{J}, \quad (5.13)$$

$$\tilde{\mathbf{i}} = \mathbf{J}\mathbf{i}_d. \quad (5.14)$$

The resulting preconditioned system matrix, $\tilde{\mathbf{A}}$, has all its diagonal elements equal to one and it is still symmetric, positive definite, and full rank. Because Jacobi preconditioning is symmetric and it retains the same system matrix properties, it can be applied prior to using the CG method, which is more computationally efficient than applying it during each iteration of the CG method [96]. Both $\tilde{\mathbf{A}}$ and $\tilde{\mathbf{i}}$ are input to the CG method, which converges to the preconditioned solution vector, $\tilde{\mathbf{v}}$, such that

$$\tilde{\mathbf{v}} = \mathbf{J}^{-1}\mathbf{v}_d. \quad (5.15)$$

The deflated solution vector is then obtained via the calculation

$$\mathbf{v}_d = \mathbf{J}\tilde{\mathbf{v}}. \quad (5.16)$$

While Jacobi preconditioning is fairly straightforward, it is limited as to how much it can improve the system matrix condition number. It can be shown that Jacobi preconditioning brings the system matrix's eigenvalues into the range $[0, 2]$ for the isotropic case, while for the anisotropic case the upper eigenvalue bound is not known exactly [96]. Consequently, polynomial preconditioning with Chebyshev polynomials is also used.

5.1.1.3.2 Polynomial Preconditioning with Chebyshev Polynomials

The idea behind using polynomial preconditioning after Jacobi preconditioning is to provide an even tighter clustering of the system matrix eigenvalues around unity [97]. Polynomial preconditioning with Chebyshev polynomials is an asymmetric method, using distinct left and right preconditioning matrices. As shown in [97], the right preconditioning matrix, \mathbf{C}_R , is set equal to the identity matrix, \mathbf{I} , while the left preconditioning matrix, \mathbf{C}_L , is set equal to $\mathbf{P}_{m-1}(\mathbf{A})$, where

$$\begin{aligned} \mathbf{P}_{m-1}(\mathbf{A}) &= \frac{2}{(\lambda_{\max} - \lambda_{\min}) T_m\left(\frac{\lambda_{\max} + \lambda_{\min}}{\lambda_{\max} - \lambda_{\min}}\right)} \sum_{n=1}^m t_n \sum_{k=0}^{n-1} \left(\frac{\lambda_{\max} + \lambda_{\min}}{\lambda_{\max} - \lambda_{\min}}\right)^{n-1-k} \\ &\quad \times \sum_{j=0}^k (-1)^j \frac{k!}{(k-j)! j!} \frac{(\lambda_{\max} + \lambda_{\min})^{k-j} 2^j}{(\lambda_{\max} - \lambda_{\min})^k} \mathbf{A}^j \\ &= \sum_{n=0}^{m-1} \alpha_n \mathbf{A}^n \end{aligned} \quad (5.17)$$

In (5.17), $\mathbf{P}_{m-1}(\mathbf{A})$ is the polynomial preconditioning matrix of degree $m-1$, $T_m(x)$ is the Chebyshev polynomial of degree m with scalar variable x , t_n are the coefficients of $T_m(x)$, and λ_{\max} and λ_{\min} are the maximum and minimum eigenvalues of the system matrix, \mathbf{A} . The Chebyshev polynomial, $T_m(x)$, and its coefficients, t_n , are generated by the recursive formula

$$T_{m+1}(x) = 2xT_m(x) - T_{m-1}(x), \quad (5.18)$$

where

$$T_0(x) = 1, \quad (5.19)$$

$$T_1(x) = x. \quad (5.20)$$

To calculate the polynomial coefficients, α_n , in (5.17) the only required values are λ_{\max} , λ_{\min} , and m .

In contrast to Jacobi preconditioning, polynomial preconditioning with Chebyshev polynomials must be applied during the CG method because it is an asymmetric method. While the full details of this “on the fly” approach are available in the literature [96, 97], the important result of this approach to preconditioning the CG method is that it remains very efficient in terms of both computational time and memory usage [97].

5.1.2 Inverse Problem Solution

The inverse problem involves determining a current dipole’s location, orientation, and magnitude from its EEG scalp potentials. Finding the solution to the inverse problem requires knowledge of the scalp potentials generated by every possible current source in the solution space. Thus, it would seem that part of the inverse problem involves solving the forward problem for three mutually orthogonal dipole orientations at every possible dipole location in the solution space. However, using lead field analysis along with the reciprocity theorem reduces the number of required forward problem solutions to just the number of electrodes on the scalp. Instead of calculating the electric potential at the electrodes for every possible dipole location and orientation, the lead field matrix (LFM) can be calculated simply by doing the opposite to this procedure. Placing a current sink at the reference electrode and a current source at each other electrode, the electric potential at every location in the head model can be calculated. According to reciprocity equation (2.31), the gradient of the electric potential then needs to be calculated for every node in the solution space in order to populate the LFM row-by-row. The gradient of the electric potential, $\nabla\phi$, is calculated using a second order approximation. For example, the partial derivative $\partial\phi/\partial x$ at node location (x, y, z) is approximated such that

$$\frac{\partial \phi}{\partial x}(x, y, z) = \frac{\phi(x+h, y, z) + \phi(x-h, y, z)}{2h} \quad (5.21)$$

The other partial derivatives, $\partial\phi/\partial y$ and $\partial\phi/\partial z$, can be approximated similarly. Once the LFM is calculated, the MUSIC (MUltiple SIgnal Classification) algorithm is used to obtain the final solution to the inverse problem. This algorithm searches the LFM for the dipole location and orientation that best fits the EEG scalp potentials generated by the unknown dipole. If desired, the magnitude of the dipole can subsequently be determined by simply scaling the current source until the scalp voltage magnitudes correctly match the EEG values. Full details of the MUSIC algorithm can be found in the literature [107, 108].

5.1.3 Validation Experiments

In order to assess the error associated with the anisotropic FVM head model, the numerical solution will be compared to the analytical solution in two different ways. For the first validation experiment, the forward problem is solved both numerically and analytically and the resulting surface voltages are compared. For the second validation experiment, the analytical head model is used to generate simulated EEG scalp potentials and then the numerical head model is used to solve the inverse problem for these voltages. The agreement of the FVM head model and the analytical head model is quantified by the source localization error. Both of these validation experiments are performed on a desktop computer with a 3.2 GHz Intel Pentium 4 processor and 2 GB of RAM.

5.1.3.1 Surface Voltage Error

Calculating the surface voltage error involves solving the forward problem for both the analytical and numerical head models. The surface voltages are calculated for an anisotropic three-shell spherical head with radii of 9.2 cm, 8.6 cm, and 8.0 cm for the scalp, skull, and brain, respectively. The voltages are determined for every surface node in the FVM head model and at the corresponding locations in the analytical head model. In total, there are 89358 surface nodes that are used as comparison points for the surface voltages. It should be noted that a grid resolution of 1 mm is used for the FVM head model, which corresponds to a total of 3342701 nodes.

Due to the symmetry of the spherical head and the surface node locations, the only dipole parameters that need to be considered are the dipole's radial distance from the center of the head and the dipole orientation. Two different dipole locations will be considered here, with both radial and tangential orientations considered at each location. The first dipole is located on the z -axis at a distance of 7.36 cm from the center of the head (an eccentricity of 0.8), while the second dipole is located on the z -axis at a distance of 4.6 cm from the center of the head (an eccentricity of 0.5). The reference node for these calculations is placed at the bottom of the head on the negative z -axis. It is assumed that the differences in the scalp voltage topography would be best illustrated with this choice of reference node location.

For the spherical head's conductivity, an isotropic case and nine different anisotropic cases are used to compare the analytical and numerical solutions. For the isotropic case, a ratio of 1:1/15:1 is used for the scalp-to-skull-to-brain conductivity ratio [33]. For the anisotropic cases, the skull, the brain, or both tissues are made anisotropic. Anisotropy ratios of 2:1, 5:1, and 10:1 are used for the skull's tangential-to-radial conductivity ratio and for the brain's radial-to-tangential conductivity ratio. As done previously for the head model comparison in two dimensions, the volume constraint [59] is used to calculate the anisotropic conductivities of the skull and brain. The volume constraint retains the geometric mean of the tensor eigenvalues and, thus, the volume of the conductivity tensor ellipsoid, such that

$$\frac{4}{3}\pi(\sigma_{\text{iso}})^3 = \frac{4}{3}\pi\sigma_{\text{rad}}(\sigma_{\text{tan}})^2, \quad (5.22)$$

where σ_{iso} is the isotropic conductivity and σ_{rad} and σ_{tan} are the anisotropic conductivities in the radial and tangential directions, respectively. As with the two-dimensional case, the idea behind using the volume constraint is that each test case will contain equal amounts of total conductivity, and the only difference will be the amount of conductivity in each direction. Table 5.1 summarizes the conductivities used for each test case.

Table 5.1: Spherical head model conductivities.

Anisotropy Ratio	Anisotropic Tissue	Scalp Conductivity (S/m)		Skull Conductivity (S/m)		Brain Conductivity (S/m)	
		σ_{rad}	σ_{tan}	σ_{rad}	σ_{tan}	σ_{rad}	σ_{tan}
1:1	N/A	0.300	0.300	0.0200	0.0200	0.300	0.300
2:1	Skull, Brain	0.300	0.300	0.0126	0.0252	0.476	0.238
2:1	Skull	0.300	0.300	0.0126	0.0252	0.300	0.300
2:1	Brain	0.300	0.300	0.0200	0.0200	0.476	0.238
5:1	Skull, Brain	0.300	0.300	0.00684	0.0342	0.877	0.175
5:1	Skull	0.300	0.300	0.00684	0.0342	0.300	0.300
5:1	Brain	0.300	0.300	0.0200	0.0200	0.877	0.175
10:1	Skull, Brain	0.300	0.300	0.00431	0.0431	1.392	0.139
10:1	Skull	0.300	0.300	0.00431	0.0431	0.300	0.300
10:1	Brain	0.300	0.300	0.0200	0.0200	1.392	0.139

For the FVM head model, the forward problem is solved with the PCG method. A relative residual of $\varepsilon = 10^{-10}$ and a maximum iteration count of 1000 were chosen based on previous work [96, 97]. To calculate the Chebyshev polynomials for the polynomial preconditioning, values of $\lambda_{max} = 2$, $\lambda_{min} = 0.01$, and $m = 8$ were chosen for the isotropic case based on previous work [96, 97]. However, the exact value of λ_{max} is unknown when anisotropic conductivities are used [96]. Consequently, an iterative procedure called Rayleigh's method [123] was used to estimate the largest eigenvalue for the system matrix in each test case. Rayleigh's method is used to estimate the dominant eigenvalue of a symmetric matrix, which, in this case, is the Jacobi preconditioned system matrix. With a specified tolerance, ε , and an arbitrary non-zero starting vector, \mathbf{x}_0 , the pseudo-code for the Rayleigh's method is as follows:

$$\mathbf{x}_0 = \frac{\mathbf{x}_0}{\|\mathbf{x}_0\|_2}$$

$$\mathbf{x} = \mathbf{A}\mathbf{x}_0$$

$$\lambda_{\max} = \mathbf{x}^T \mathbf{x}_0$$

$$tol = 1000$$

WHILE $tol > \varepsilon$

$$\lambda_{\text{temp}} = \lambda_{\max}$$

$$\mathbf{x}_{\text{temp}} = \mathbf{x}_0$$

$$\mathbf{x}_0 = \mathbf{x}$$

$$\mathbf{x} = \mathbf{x}_{\text{temp}}$$

$$\mathbf{x}_0 = \frac{\mathbf{x}_0}{\|\mathbf{x}_0\|_2}$$

$$\mathbf{x} = \mathbf{A}\mathbf{x}_0$$

$$\lambda_{\max} = \mathbf{x}^T \mathbf{x}_0$$

$$tol = \left| \frac{\lambda_{\max} - \lambda_{\text{temp}}}{\lambda_{\max}} \right|$$

END WHILE

Using Rayleigh's method, it was determined that an approximate value of $\lambda_{\max} = 2$ was appropriate for every test case.

The surface voltage error is quantified with the same two error measures used to compare the voxel- and vertex-centered approaches for the FVM in two dimensions: the L2 relative error norm and the correlation coefficient. To reiterate, the L2 relative error norm is defined as

$$RE = \frac{\|\phi^{\text{Num}} - \phi^{\text{Ana}}\|_2}{\|\phi^{\text{Ana}}\|_2} \times 100\%, \quad (5.23)$$

where ϕ^{Num} and ϕ^{Ana} are the voltage values from the numerical and analytical head models, respectively. The L2 relative error norm measures the agreement of the

magnitude and shape of the two different sets of voltages, and is measured with respect to the analytically calculated voltages. A value of 0% for the L2 relative error norm indicates perfect agreement between the two sets of values. The correlation coefficient is defined as

$$CC = \frac{\sum_{i=1}^M (\phi_i^{\text{Num}} - \overline{\phi^{\text{Num}}}) (\phi_i^{\text{Ana}} - \overline{\phi^{\text{Ana}}})}{\sqrt{\left(\sum_{i=1}^M (\phi_i^{\text{Num}} - \overline{\phi^{\text{Num}}})^2 \right) \left(\sum_{i=1}^M (\phi_i^{\text{Ana}} - \overline{\phi^{\text{Ana}}})^2 \right)}}, \quad (5.24)$$

where $\overline{\phi^{\text{Num}}}$ and $\overline{\phi^{\text{Ana}}}$ are the mean values of the numerical and analytical scalp potentials, respectively, and M is the number of measurement points on the scalp. The correlation coefficient measures the agreement of the shape of the two different voltage distributions. A value of 1 for the correlation coefficient indicates perfect agreement between the two sets of values.

5.1.3.2 Source Localization Error

Calculating the source localization error involves solving both the forward and inverse problem. The forward problem is solved with the analytical head model [67, 68] and the resulting voltage values serve as simulated EEG readings at the electrode sites. As with the surface voltage error calculations, an anisotropic three-shell spherical head is used with radii of 9.2 cm, 8.6 cm, and 8.0 cm for the scalp, skull, and brain, respectively. For the electrodes, an even spatial distribution of 37 electrodes over the upper half of the sphere was chosen, as shown in Figure 5.1. The exact location of each electrode is provided in Table 5.2 in terms of two angles: tip and spin. The tip is the angular displacement from the positive z -axis (top of head) towards the xy -plane, while the spin is the angular displacement from the positive x -axis towards the positive y -axis. The reference electrode is chosen to be electrode 1, located at the top of the head model on the z -axis, and is shown in red in Figure 5.1.

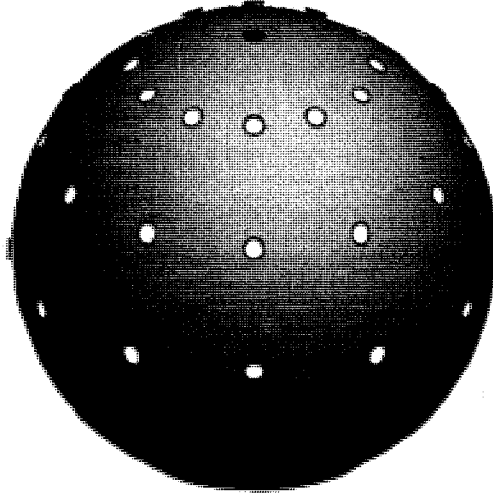


Figure 5.1: Electrode placement on the spherical head model. The reference electrode is shown in red.

Table 5.2: Electrode configuration.

Electrode Number	Tip (degrees)	Spin (degrees)	Electrode Number	Tip (degrees)	Spin (degrees)
1	0	0	20	60	180
2	30	0	21	60	210
3	30	30	22	60	240
4	30	60	23	60	270
5	30	90	24	60	300
6	30	120	25	60	330
7	30	150	26	90	0
8	30	180	27	90	30
9	30	210	28	90	60
10	30	240	29	90	90
11	30	270	30	90	120
12	30	300	31	90	150
13	30	330	32	90	180
14	60	0	33	90	210
15	60	30	34	90	240
16	60	60	35	90	270
17	60	90	36	90	300
18	60	120	37	90	330
19	60	150			

Using a 1 mm grid resolution and a total of 3342701 nodes, the inverse problem is then solved with the FVM to determine the best fit dipole location and orientation that corresponds to the simulated EEG scalp potentials. This best fit dipole location and orientation is compared to the actual dipole location to determine the source localization error. The same three-shell spherical head is used by the analytical and numerical head models and, thus, the source localization error will provide an indication of the error associated with the FVM.

Instead of using a single dipole, one hundred different dipole locations are randomly chosen for this validation test. The nodes corresponding to the dipole locations are randomly chosen from the upper half of the brain in the head model. Additionally, the dipole locations must be at least one node away from the boundary between the skull and brain because both the source and sink must reside in the brain. For each random location, a dipole is oriented in the x -, y -, and z -directions, thus a total of three hundred different dipoles are used to calculate the source localization error.

For the spherical head's conductivity, the same values are used that were used in the surface voltage error calculations. To summarize, an isotropic case and nine different anisotropic cases are used. For the isotropic case, a ratio of 1:1/15:1 is used for the scalp-to-skull-to-brain conductivity ratio [33]. For the anisotropic cases, the skull, the brain, or both tissues are made anisotropic. Anisotropy ratios of 2:1, 5:1, and 10:1 are used for the skull's tangential-to-radial conductivity ratio and for the brain's radial-to-tangential conductivity ratio. The volume constraint [59] is used to calculate the anisotropic conductivities of the skull and brain, which are shown in Table 5.1.

In order to generate the LFM, the forward problem is solved for the FVM head model with the PCG method. As with the surface voltage error calculations, a relative residual of $\varepsilon = 10^{-10}$ and a maximum iteration count of 1000 were chosen. Additionally, the same values were used for the polynomial preconditioning, such that $\lambda_{\max} = 2$, $\lambda_{\min} = 0.01$, and $m = 8$. One concern regarding the LFM is the solution space. Ideally, the entire upper half of the brain in the head model would be considered the solution space and would be used to generate the LFM. However, this region consists of 1078780 nodes and there is simply not enough computer memory available to generate the LFM. Consequently, a modified solution space is used to solve the inverse problem. Since each

of the one hundred random dipole locations is known, a unique solution space is generated for each dipole that consists of a sphere centered at the dipole location with a radius of 40 mm. If any nodes in this sphere overlap with other tissue or the lower half of the brain they are removed from the solution space so that it just consists of nodes within the upper half of the brain. This means that each solution space will consist of a maximum of 283409 nodes and that there will be enough memory to generate the LFM. Unfortunately, this method of generating the LFM is quite inefficient, since a new LFM must be generated for each of the one hundred random dipole locations. While this kind of solution space is not ideal, it seems like a good alternative given the memory limitations and it is likely that no localization errors will be larger than 40 mm.

These source localization calculations aim to find two pieces of information: the dipole location and orientation. In order to quantify the source localization error, two different error measures are used. The position error is the Euclidean distance, d , between the actual dipole location, $(x_{\text{act}}, y_{\text{act}}, z_{\text{act}})$, and the estimated dipole location, $(x_{\text{est}}, y_{\text{est}}, z_{\text{est}})$, such that

$$d = \sqrt{(x_{\text{est}} - x_{\text{act}})^2 + (y_{\text{est}} - y_{\text{act}})^2 + (z_{\text{est}} - z_{\text{act}})^2}. \quad (5.25)$$

Three different measures of the position error will be provided: the mean position error, \bar{d} , the maximum position error, d_{max} , and the minimum position error, d_{min} . The orientation error is the angle, θ , between the actual dipole orientation vector, \mathbf{r}_{act} , and the estimated dipole orientation vector, \mathbf{r}_{est} , such that

$$\theta = \cos^{-1} \left(\frac{\mathbf{r}_{\text{act}} \cdot \mathbf{r}_{\text{est}}}{|\mathbf{r}_{\text{act}}| |\mathbf{r}_{\text{est}}|} \right). \quad (5.26)$$

As with the position error, three different measures of the orientation error will be provided: the mean orientation error, $\bar{\theta}$, the maximum orientation error, θ_{max} , and the minimum orientation error, θ_{min} .

5.2 Results

The results for each of the validation experiments are provided below. Both the surface voltage error and the source localization error help to quantify the numerical accuracy of the FVM.

5.2.1 Surface Voltage Error

The results from the surface voltage error calculations are shown in the following tables. The results for the radial and tangential dipoles at an eccentricity of 0.8 are shown in Table 5.3 and Table 5.4, respectively, while the results for the radial and tangential dipoles at an eccentricity of 0.5 are shown in Table 5.5 and Table 5.6, respectively. In addition to the L2 relative error norm and the correlation coefficient, the maximum and minimum voltage values are also provided for both the numerical and analytical head models.

Table 5.3: Surface voltage error for a radial dipole at an eccentricity of 0.8.

Anisotropy Ratio	Anisotropic Tissue	RE (%)	CC	Maximum Voltage (V)		Minimum Voltage (V)	
				Numerical	Analytical	Numerical	Analytical
1:1	N/A	2.91	0.9997	9.54	9.28	0.00	0.00
2:1	Skull, Brain	3.66	0.9995	4.98	4.91	0.00	0.00
2:1	Skull	3.55	0.9995	6.99	6.75	0.00	0.00
2:1	Brain	2.68	0.9997	7.03	6.93	0.00	0.00
5:1	Skull, Brain	8.58	0.9988	1.72	1.78	0.00	0.00
5:1	Skull	4.80	0.9990	4.41	4.19	0.00	0.00
5:1	Brain	3.14	0.9996	4.44	4.44	0.00	0.00
10:1	Skull, Brain	19.34	0.9978	0.66	0.74	0.00	0.00
10:1	Skull	6.01	0.9985	2.98	2.81	0.00	0.00
10:1	Brain	4.62	0.9996	3.03	3.06	0.00	0.00

Table 5.4: Surface voltage error for a tangential dipole at an eccentricity of 0.8.

Anisotropy Ratio	Anisotropic Tissue	RE (%)	CC	Maximum Voltage (V)		Minimum Voltage (V)	
				Numerical	Analytical	Numerical	Analytical
1:1	N/A	3.24	0.9998	3.82	3.64	-3.82	-3.64
2:1	Skull, Brain	5.30	0.9997	3.04	2.82	-3.04	-2.82
2:1	Skull	5.11	0.9997	2.85	2.65	-2.85	-2.65
2:1	Brain	3.48	0.9998	4.15	3.94	-4.15	-3.94
5:1	Skull, Brain	9.34	0.9994	2.07	1.83	-2.07	-1.83
5:1	Skull	9.49	0.9993	1.90	1.67	-1.90	-1.67
5:1	Brain	3.54	0.9998	4.44	4.22	-4.44	-4.22
10:1	Skull, Brain	14.73	0.9991	1.58	1.32	-1.59	-1.32
10:1	Skull	15.71	0.9989	1.38	1.14	-1.38	-1.14
10:1	Brain	3.38	0.9998	4.61	4.39	-4.62	-4.39

Table 5.5: Surface voltage error for a radial dipole at an eccentricity of 0.5.

Anisotropy Ratio	Anisotropic Tissue	RE (%)	CC	Maximum Voltage (V)		Minimum Voltage (V)	
				Numerical	Analytical	Numerical	Analytical
1:1	N/A	1.86	0.9999	3.08	3.01	0.00	0.00
2:1	Skull, Brain	3.16	0.9998	2.56	2.46	0.00	0.00
2:1	Skull	3.05	0.9999	2.71	2.61	0.00	0.00
2:1	Brain	2.21	0.9999	3.02	2.94	0.00	0.00
5:1	Skull, Brain	5.68	0.9994	1.56	1.46	0.00	0.00
5:1	Skull	5.64	0.9998	2.18	2.04	0.00	0.00
5:1	Brain	3.32	0.9998	2.69	2.60	0.00	0.00
10:1	Skull, Brain	6.72	0.9986	0.88	0.81	0.00	0.00
10:1	Skull	9.78	0.9996	1.80	1.61	0.00	0.00
10:1	Brain	2.81	0.9998	2.29	2.22	0.00	0.00

Table 5.6: Surface voltage error for a tangential dipole at an eccentricity of 0.5.

Anisotropy Ratio	Anisotropic Tissue	RE (%)	CC	Maximum Voltage (V)		Minimum Voltage (V)	
				Numerical	Analytical	Numerical	Analytical
1:1	N/A	2.49	0.9999	1.46	1.41	-1.46	-1.41
2:1	Skull, Brain	4.63	0.9998	1.84	1.73	-1.84	-1.73
2:1	Skull	4.21	0.9999	1.29	1.22	-1.29	-1.22
2:1	Brain	2.83	0.9999	2.14	2.06	-2.14	-2.06
5:1	Skull, Brain	9.37	0.9995	2.07	1.83	-2.06	-1.83
5:1	Skull	8.56	0.9996	1.06	0.96	-1.06	-0.96
5:1	Brain	3.06	0.9999	3.25	3.11	-3.25	-3.11
10:1	Skull, Brain	15.51	0.9990	2.04	1.69	-2.04	-1.69
10:1	Skull	15.08	0.9993	0.89	0.75	-0.89	-0.75
10:1	Brain	3.01	0.9998	4.22	4.03	-4.22	-4.03

After evaluating the results from all the test cases, it can be observed that there is good agreement between the numerical and analytical head models for the isotropic case and for the anisotropic case with an anisotropy ratio of 2:1. However, the overall trend of the data is that the L2 relative error norm increases and the correlation coefficient decreases for higher anisotropy ratios; that is, the accuracy of the FVM head model decreases for higher anisotropy ratios. In most cases, the accuracy of the FVM head model also decreases when both the skull and brain are made anisotropic, instead of when just the skull or brain is anisotropic. Additionally, the accuracy of the scalp potentials' magnitude seems to be more affected by changes in the anisotropy ratio than the shape of the scalp potential distributions. This is evident when considering the consistently high value of the correlation coefficient and is further illustrated by the graphs in Figure 5.2 and Figure 5.3 that show the scalp potentials from a tangential dipole for a slice of the head in the sagittal plane.

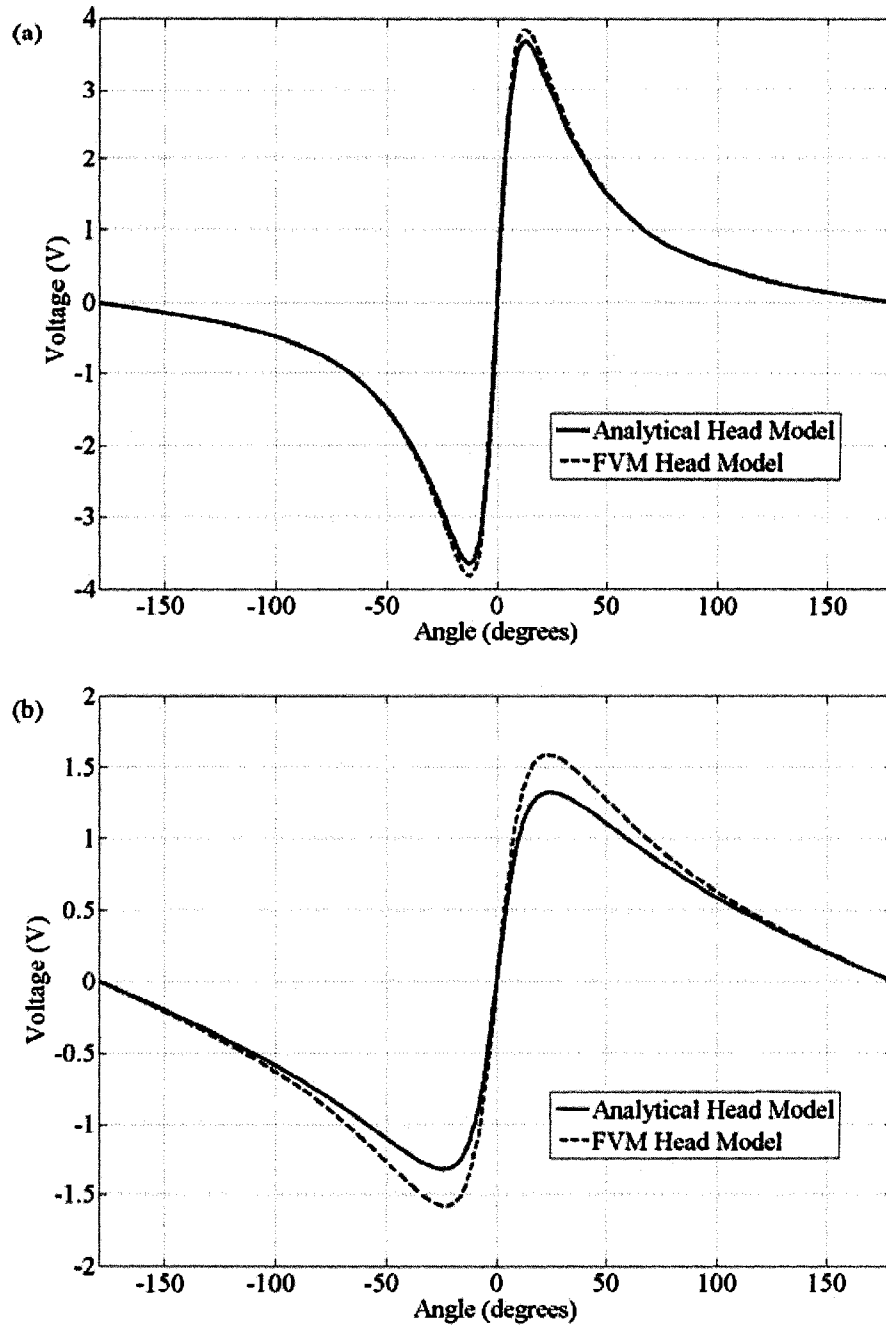


Figure 5.2: Surface voltages for a tangential dipole at an eccentricity of 0.8. The voltages are from a sagittal slice of the head and for anisotropy ratios of (a) 1:1 and (b) 10:1.

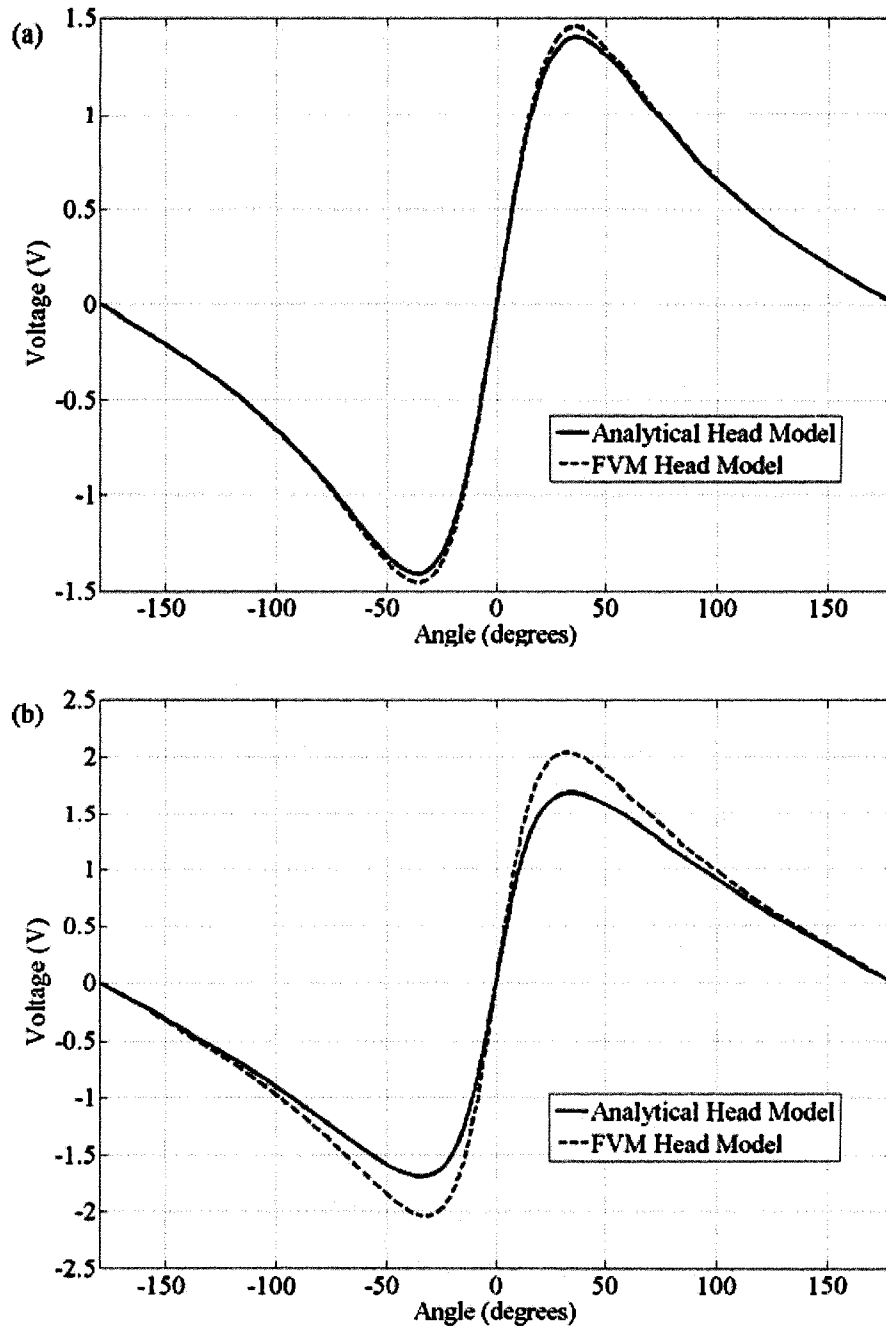


Figure 5.3: Surface voltages for a tangential dipole at an eccentricity of 0.5. The voltages are from a sagittal slice of the head and for anisotropy ratios of (a) 1:1 and (b) 10:1.

Another interesting trend observed in the data is that the accuracy of the FVM head model appears to be more affected by the skull anisotropy than the brain anisotropy. Comparing the cases when only the skull or the brain is anisotropic, the L2 relative error

norm is always higher and the correlation coefficient is always lower for the cases when the skull is anisotropic.

5.2.2 Source Localization Error

The results from the source localization error calculations are shown in Table 5.7. It is important to note that the modified solution spaces used to create the LFM's can be considered acceptable since each solution space had a radius of 40 mm and the largest position error was 22.76 mm. The average solution time required by the PCG method to solve the forward problem is summarized in Table 5.8. While this research is not focused on optimizing the PCG method, it is interesting to observe that the average solution times increase for higher anisotropy ratios and when the amount of anisotropic tissue increases.

Table 5.7: Spherical head model source localization error.

Anisotropy Ratio	Anisotropic Tissue	Position Error (mm)			Orientation Error (degrees)		
		\bar{d}	d_{\max}	d_{\min}	$\bar{\theta}$	θ_{\max}	θ_{\min}
1:1	N/A	1.21	2.45	0.00	0.39	2.43	0.00
2:1	Skull, Brain	2.21	4.90	0.00	0.68	4.64	0.00
2:1	Skull	1.61	3.32	0.00	0.41	1.63	0.00
2:1	Brain	1.47	4.90	0.00	0.52	3.69	0.00
5:1	Skull, Brain	5.79	11.45	0.00	2.59	21.73	0.00
5:1	Skull	2.73	4.90	1.00	0.62	2.39	0.01
5:1	Brain	2.41	7.55	0.00	1.34	19.08	0.00
10:1	Skull, Brain	13.66	22.76	2.83	6.37	30.14	0.04
10:1	Skull	4.17	6.40	1.00	0.92	2.96	0.01
10:1	Brain	3.57	8.77	0.00	2.35	17.73	0.01

Table 5.8: Average PCG method solution time on the spherical head model.

Anisotropy Ratio	Anisotropic Tissue	Average Solution Time (min:sec)
1:1	N/A	5:43
2:1	Skull, Brain	14:22
2:1	Skull	8:48
2:1	Brain	12:26
5:1	Skull, Brain	16:31
5:1	Skull	9:09
5:1	Brain	13:46
10:1	Skull, Brain	18:43
10:1	Skull	9:20
10:1	Brain	15:48

From Table 5.7 it can be observed that the mean position and orientation errors are very low for the isotropic case and the anisotropic case with an anisotropy ratio of 2:1. In general, though, all of the position and orientation errors increase for higher anisotropy ratios, indicating a decrease in the source localization accuracy of the FVM head model for higher anisotropy ratios. Furthermore, the source localization accuracy of the FVM head model decreases when both the skull and brain are anisotropic, as compared to when just the skull or brain is anisotropic.

For all anisotropy ratios, the mean position errors are higher for the anisotropic skull head models than for the anisotropic brain head models. Therefore, in terms of position error, the FVM head model seems to be preferentially affected by skull anisotropy rather than brain anisotropy. The mean orientation errors, on the other hand, are higher for the anisotropic brain head models than for the anisotropic skull head models. Thus, in terms of orientation error, the FVM head model appears to be slightly more affected by brain anisotropy than skull anisotropy.

5.3 Discussion

In this chapter, the anisotropic FVM head model was compared to the analytical head model using surface voltage error and source localization error. These validation experiments helped characterize and quantify the numerical accuracy of the FVM. The

FVM head model shows good agreement with the analytical head model, with the best accuracy occurring for the isotropic case and the anisotropic case with an anisotropy ratio of 2:1. Unfortunately, more severe anisotropy appears to be a problem, since increasing the anisotropy ratio from 2:1 to 5:1 and 10:1 caused a decrease in accuracy. It is suspected that this is primarily related to the increasingly large change in conductivity between the skull and the brain for the higher anisotropy ratios. While the FVM head model can handle inhomogeneous conductivities, the drastic change from the skull to the brain is likely the source of most of the numerical errors for larger anisotropy ratios. Employing a higher grid resolution could help alleviate accuracy problems associated with larger anisotropy ratios, but there is a tradeoff between the grid resolution and the amount of computer memory and computational time required. The current grid resolution of 1 mm is near the limit of the computational resources available on the desktop computer used for these calculations. However, there are faster and more powerful computers available that could easily handle grid resolutions of 0.5 mm or better, and reduce the amount of error associated with larger anisotropy ratios.

With real patient data it is expected that accuracy problems related to severe anisotropy ratios may not be as significant. Real conductivity values obtained near tissue boundaries may exhibit less severe changes in conductivity due to partial volume effects in magnetic resonance images. Also, even though large anisotropy ratios may exist in individual white matter (WM) fibers, these values may not be accurately represented by the diffusion tensor imaging data due to crossing fibers within the same voxel [62, 124]. And, while individual voxels may exhibit large anisotropy ratios, it is unlikely that this would be the same for every voxel of a particular tissue type. Moreover, the spherical head model uses a very simplistic model of the brain, with anisotropic WM fibers radiating from the center of the head in the radial direction. Therefore, the direction of the highest conductivity in the brain is perpendicular to the direction of highest conductivity in the skull. This is an abrupt change in conductivity that is not likely to exist in real human heads. In reality, the WM fiber tracts near the surface of the brain can be oriented both perpendicular and parallel to the surface of the skull and there is a layer of cerebrospinal fluid between the brain and the skull.

As indicated by the results from the surface voltage error calculations, the FVM head model more accurately calculates the shape of the scalp potential distributions than the magnitude of the scalp potentials. While it would be ideal if the magnitudes were calculated more accurately, it is important to realize that differences in the shape of the scalp potential distributions are far more important than differences in their magnitude. The scalp potential distribution's shape is indicative of the location and orientation of the current source, while its magnitude only reflects the strength of the source. Consequently, the correlation coefficient has been used in the literature as an indicator of source localization accuracy for head models. While the correlation coefficient is not a perfect indicator of source localization accuracy, it has been observed that correlation coefficients above 0.99 will result in position errors of approximately 1 mm or less [62]. Similarly, it has been observed that correlation coefficients of 0.98 could produce position errors from 5 mm up to 1.5 cm in the worst case [62]. Since all of the correlation coefficients in Table 5.3, Table 5.4, Table 5.5, and Table 5.6 are above 0.99, the observations from [62] would seem to indicate that the FVM head model will produce accurate results for EEG source analysis.

The results from the source localization error calculations can also be further evaluated by comparing them to results in the literature. In this case, the study in the literature [60] validated an anisotropic FDM head model [81] using a five-shell spherical head and the corresponding analytical solution [67, 68]. The five-shell spherical head model is comprised of scalp, skull, and three brain shells, which consists of a WM shell surrounded on either side by a gray matter shell. For the spherical head's conductivity, an isotropic case and two different anisotropic cases were used. For the isotropic case, a ratio of 1:1/16:1 was used for the scalp-to-skull-to-brain conductivity ratio. A mean position error of 0.48 mm was reported, compared to the mean position error of 1.21 mm shown in Table 5.7. For the first anisotropic case, the skull was made anisotropic with an anisotropy ratio of 10:1. Mean and maximum position error values of 2.55 mm and 6.79 mm, respectively, were reported, compared to the mean and maximum position error values of 4.17 mm and 6.40 mm, respectively, shown in Table 5.7. For the second anisotropic case, the WM was made anisotropic with an anisotropy ratio of 9:1. Mean and maximum position errors of 1.04 mm and 11.61 mm, respectively, were reported,

compared to the mean and maximum position error values of 3.57 mm and 8.77 mm, respectively, shown in Table 5.7.

It is to be expected that the values for the position errors did not match up exactly for both sets of data since the study in [60] did not have exactly the same parameters as the source localization error calculations conducted for this research. The better performance of the head model in [60] can most likely be explained by four key differences. First, a five-shell spherical head was used instead of the three-shell spherical head that was used in this research. Second, slightly different conductivity values were used. A ratio of 1:1/16:1 was used for the scalp-to-skull-to-brain conductivity ratio in [60] instead of the ratio of 1:1/15:1 used in this research. Additionally, for the case of the anisotropic brain, the brain's anisotropy ratio was 9:1 instead of 10:1 and only the WM shell was made anisotropic instead of the entire brain shell. Third, a different electrode configuration was used, with 27 electrodes being used in [60] compared to the 37 electrodes used in this research. Finally, the dipole locations used in [60] were only in the xy -, xz -, and yz -planes of the brain shells, as opposed to the random dipole locations used in this research. While the results in [60] were better than those in Table 5.7, the same trend exists for both sets of data. For both sets of data, more error occurs when there are anisotropic tissues instead of all tissues being isotropic. As well, when the skull is anisotropic there is a larger mean position error than when the brain is anisotropic.

The effect that an anisotropic brain or skull has on the numerical accuracy of the FVM is somewhat unclear. The surface voltage errors seem to indicate that the FVM accuracy is more affected by the skull anisotropy than the brain anisotropy. However, the source localization errors seem to indicate that neither tissue preferentially influences the FVM accuracy. While the position error is more affected by the skull anisotropy, the orientation error is more affected by the brain anisotropy. Therefore, unless a spherical head model is to be used for EEG source analysis, it is probably not possible to make a generalized statement about the influence of a single tissue's anisotropy on the numerical accuracy of the FVM. No two realistic head models will be exactly the same, as there will be differences in each tissue's geometry, distribution, and conductivity. Consequently, the influence of a particular tissue will vary from person to person.

Overall, these validation experiments have helped to characterize and quantify the modeling error associated with the FVM. The main conclusion that can be drawn from these studies is that the FVM head model is accurate enough to be used for EEG source analysis. And, while severe anisotropy can potentially pose a problem, it is not expected to be a significant problem when dealing with real patient data.

Chapter 6: Effect of Neglecting Anisotropy

A large amount of electroencephalogram (EEG) source analysis is still done on head models with only isotropic conductivities [18, 42-55], neglecting the fact that some tissues in the head are known to be anisotropic [3, 32, 57-61]. Consequently, it is felt that the effect anisotropy should be investigated and that any error associated with neglecting anisotropic conductivities should be quantified. In this chapter, a realistic head model and the finite volume method (FVM) are used to calculate the source localization error associated with neglecting anisotropic conductivities. The results of this study are presented and there is a discussion about the effect that neglecting anisotropy has on EEG source analysis accuracy. This will provide some insight into the importance of anisotropic conductivity in head models and whether it should be included or not.

6.1 Methods

To investigate the effect of neglecting anisotropy, a realistic head model is created using data obtained from magnetic resonance imaging (MRI) and diffusion tensor imaging (DTI), which provide structural information about the whole head and conductivity information for the brain tissues, respectively. Source localization error is used to quantify the effect of neglecting anisotropy, making it necessary to solve the inverse problem. Using the FVM, the forward problem is solved for the realistic head to produce simulated EEG readings at the electrode sites. Then, the inverse problem is solved for these simulated EEG scalp potentials, using the FVM and a version of the realistic head in which all anisotropic conductivities are made isotropic. In other words, EEG scalp potentials are produced by a head with anisotropic conductivities and then the source of these voltages is localized assuming that the head only contains isotropic conductivities. Details of how the realistic head model is created and how the forward and inverse problems are solved are provided below.

6.1.1 Realistic Head Model

The realistic head model is generated using T1-weighted MRI and DTI data obtained by imaging my own head at the University of Alberta In Vivo Nuclear Magnetic Resonance (NMR) Centre. The T1-weighted MRI data was acquired at $0.5 \times 0.5 \times 1 \text{ mm}^3$ resolution,

while the DTI data was acquired at $1 \times 1 \times 2 \text{ mm}^3$ resolution. Prior to obtaining the data from the In Vivo NMR Centre, it was co-registered in order to align the two different data sets and re-sampled in order to obtain a $1 \times 1 \times 1 \text{ mm}^3$ resolution.

The T1-weighted MRI data is used to obtain the structural information for the realistic head model by segmenting the images into five tissues types: scalp, skull, cerebrospinal fluid (CSF), gray matter (GM), and white matter (WM). Two different software packages are used to segment the T1-weighted images. The scalp and skull are obtained using the mTrack software package [125], which uses a dynamic edge tracing algorithm to determine tissue surfaces on a slice-by-slice basis. For each image slice, the user specifies starting points and mTrack defines contours along the inner and/or outer surfaces for the desired tissues. Occasionally, user intervention is required to complete a contour if mTrack is unable to or to adjust a contour if mTrack makes a mistake. For the T1-weighted images, the scalp's outer surface and the skull's outer surface (or, conversely, the scalp's inner surface) is relatively easy to segment, requiring just a small amount of user intervention. The skull's inner surface is not segmented since the boundary between the skull and CSF can not be differentiated in T1-weighted images. Since this segmentation procedure in mTrack is semi-automated, it can be somewhat time consuming and labour intensive, especially for complicated surfaces such as the GM and WM. As such, the CSF, GM, and WM are obtained using the FSL software package [126].

FSL is a comprehensive library of analysis tools for functional MRI, MRI, and DTI brain image data and it is written mainly by members of the Analysis Group at the Oxford Centre for Functional Magnetic Resonance Imaging of the Brain (FMRIB). There are two fully automated tools that FSL uses to segment the T1-weighted images into CSF, GM, and WM. The Brain Extraction Tool (BET) [127] removes the non-brain tissues from the whole head images and then FMRIB's Automated Segmentation Tool (FAST) [128] classifies each voxel as either CSF, GM, or WM. Since BET and FAST are fully automated, segmenting the CSF, GM, and WM is a very quick and easy procedure. These time savings provided by FSL greatly outweigh any slight reduction in accuracy when compared to mTrack. It should be noted that FSL could potentially be used to segment the entire head. Using BET, the outer scalp surface and the inner and outer skull

surfaces can be estimated as long as both T1- and T2-weighted images are available. Obviously this was not done in this case, since only T1-weighted images were available.

With all the tissues segmented, the final stages of assembling the realistic head model are done in MATLAB. Voxels between the scalp's outer surface and the skull's outer surface are defined as scalp, while voxels between the skull's outer surface and the CSF voxels are defined as skull. It should be noted that the entire surface of the brain is surrounded by a layer of CSF that is at least one voxel thick. The resulting realistic head model consists of a matrix with dimensions of $256 \times 192 \times 120$ and each voxel has dimensions of $1 \times 1 \times 1 \text{ mm}^3$. A comparison of the original T1-weighted images to the final version of the segmented head model is shown in Figure 6.1. Additionally, renderings of the scalp, skull, and brain are shown in Figure 6.2 to illustrate the segmented head model in three dimensions.

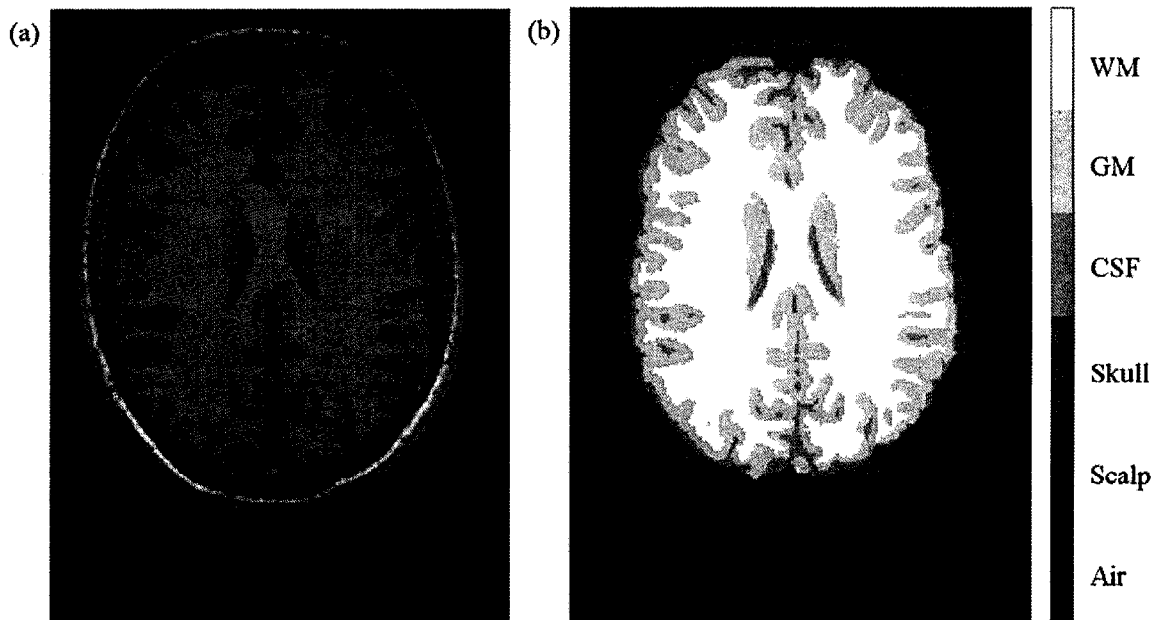


Figure 6.1: Real head and segmented head comparison. The images shown are slices from the (a) T1-weighted MRI and the (b) segmented head model.

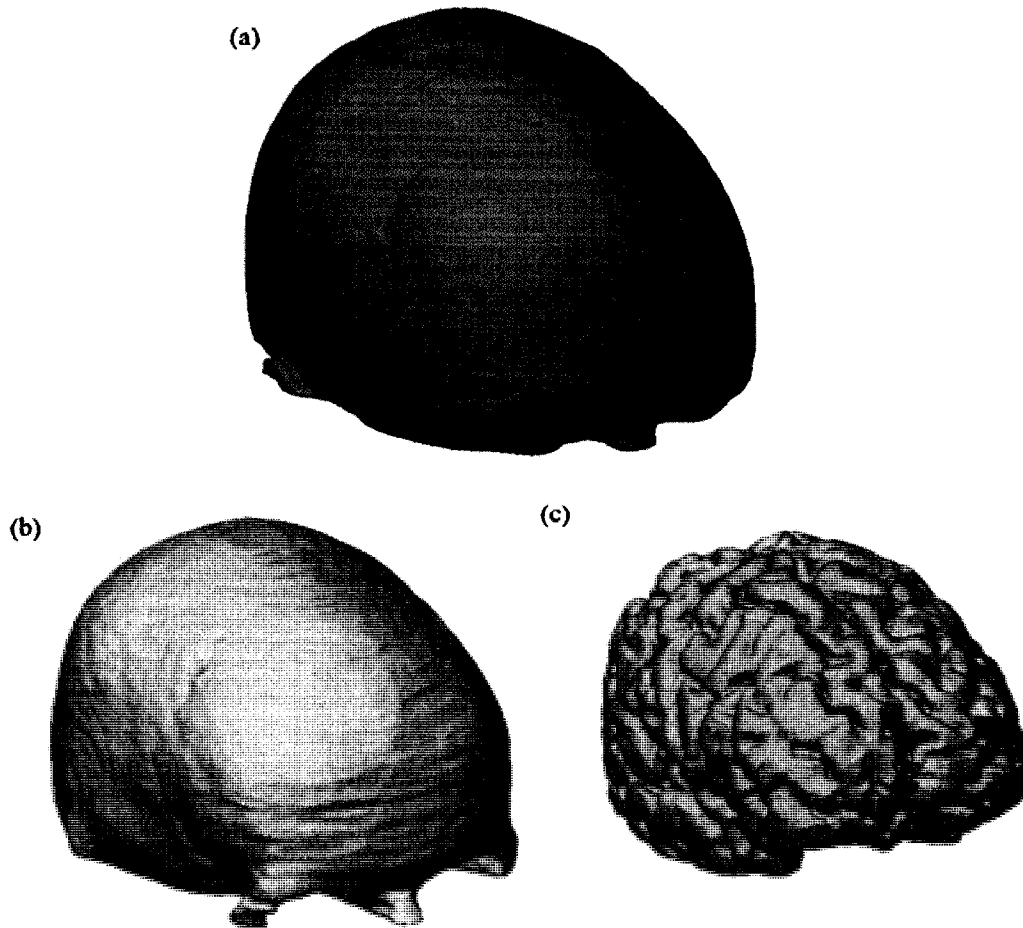


Figure 6.2: Three-dimensional representation of the realistic head model. The tissues shown are the (a) scalp, (b) skull, and (c) brain.

With the structural aspects of the realistic head model accounted for, the conductivities for each voxel must be assigned. The DTI data is used to calculate the conductivity tensors for the CSF, GM, and WM voxels in two steps. First, the diffusion tensors are calculated for the voxels using the DTI-Studio software package [129]. Then, the diffusion tensors are converted to conductivity tensors using (2.13) and the empirically determined ratio $\sigma_e/d_e = 0.736 \text{ S}\cdot\text{s}/\text{mm}^3$ [62]. The mean anisotropy ratio of the resulting conductivity tensors was calculated to be 4.11. The conductivity of the scalp and skull, unfortunately, can not be determined from DTI. Consequently, isotropic conductivities are calculated for the scalp and skull using a scalp-to-skull-to-brain conductivity ratio of 1:1/15:1 [33] and the mean conductivity of the brain. The mean brain conductivity is calculated by converting the CSF, GM, and WM conductivity

tensors into isotropic values using the volume constraint [59]. The resulting mean brain conductivity has a value of 0.680 S/m, meaning that isotropic conductivities of 0.680 S/m and 0.0453 S/m are assigned to the scalp and skull, respectively. It should be noted that while DTI has the potential to eliminate the need for segmentation, full head segmentation was still required in this case because DTI only provides the conductivity values for the CSF, GM, and WM. Additionally, in most cases some segmentation will always be required to, at the very least, define the solution space.

6.1.2 Source Localization Error

Calculating the source localization error involves solving both the forward and inverse problems with the FVM on the realistic head model. In order to evaluate the effect of neglecting anisotropy, the head model conductivity is different for the forward and inverse problems. While the forward problem is solved on an anisotropic head model, the inverse problem is solved on an isotropic head model. The forward problem solution serves as simulated EEG scalp potentials and it is calculated with anisotropic brain conductivities. The inverse problem solution is calculated for these simulated EEG scalp potentials, using a lead field matrix (LFM) that is generated from a head model with isotropic brain conductivities. As with the experiments from the previous chapter, the source localization error calculations are performed on a desktop computer with a 3.2 GHz Intel Pentium 4 processor and 2 GB of RAM.

Using the FVM, the realistic head model is decomposed into the system matrix for a 1 mm grid resolution that consists of 2626047 nodes. In order to make a valid comparison between the anisotropic and isotropic cases, both head models contain equal amounts of total conductivity. This is accomplished by using the volume constraint [59] to calculate the isotropic conductivities from the anisotropic conductivity tensors on a voxel-by-voxel basis. The electrode placement used for the realistic head is the same as what was used for the spherical head in the previous chapter, as shown in Table 5.2. However, these electrodes' tip and spin angles are defined relative to the center of a spherical head. To overcome the fact that the realistic head does not have a defined center, a sphere is fitted to the realistic head to find an approximate center of the head. Then, the surface nodes on the realistic head that most closely match each electrode's tip and spin angles are chosen as the electrode locations. The resulting electrode distribution

is shown in Figure 6.3. As with the spherical head, the reference electrode is chosen to be electrode 1, which is located at the top of the head model on the z -axis.

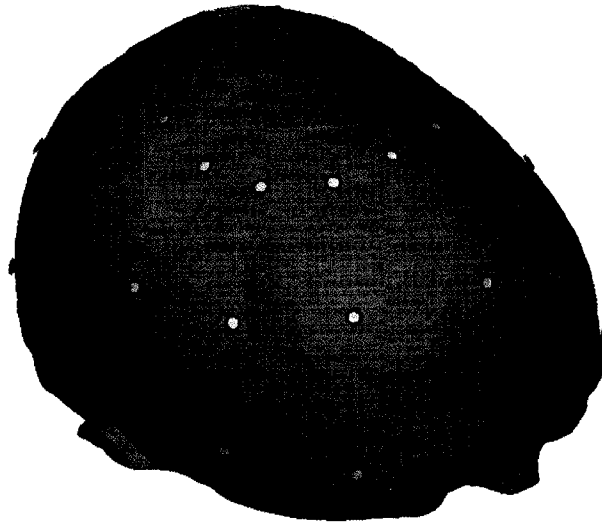


Figure 6.3: Electrode placement on the realistic head model. The reference electrode is shown in red.

One thousand different dipole locations are randomly chosen for these source localization error calculations. The nodes corresponding to the dipole locations are randomly chosen from the solution space in the head model and, for each random location, a dipole is oriented in the x -, y -, and z -directions. This means that a total of three thousand random dipoles are used to calculate the source localization error.

Unlike the different solution spaces generated for each dipole in the previous chapter, only a single solution space is defined for the realistic head model. Here, the solution space is defined using *a priori* constraints and is restricted to the GM in the head model. Additionally, the dipole locations must be at least one node away from the surface of the GM since both the source and sink must reside in the GM. Consequently, the solution space is defined as the GM minus one voxel thickness along its boundary. Due to computer memory limitations, one additional voxel along the boundary is also removed. This results in a solution space that is the GM minus 2 mm from its boundary and consists of 430850 nodes.

Using this single solution space for each of the three thousand dipoles actually reduces the number of forward problem calculations that are required. By creating a LFM

for the anisotropic realistic head model, the forward problem only needs to be solved 36 times instead of three thousand times. The simulated EEG scalp potentials for each dipole can simply be extracted from the corresponding column in the LFM. Having a single solution space also reduces the number of calculations for the inverse problem. Unlike when there was a different solution space for each dipole, only a single LFM must be generated for the isotropic realistic head model. Therefore, any forward or inverse problem can be solved once the two LFMs are created. This significantly reduces the required amount of calculation time and is the reason that so many more dipoles can be used compared to the experiments done for the spherical head.

In order to generate the two LFMs, the forward problem is solved with the preconditioned conjugate gradient (PCG) method using the same procedure as presented in the previous chapter. As with the previous calculations, a relative residual of $\varepsilon = 10^{-10}$ and a maximum iteration count of 1000 were chosen. Additionally, the same values were used for the polynomial preconditioning, such that $\lambda_{\max} = 2$, $\lambda_{\min} = 0.01$, and $m = 8$, where Rayleigh's method [123] was again used to estimate the largest eigenvalue for each system matrix.

As with previous source localization calculations, these calculations aim to find two pieces of information: the dipole location and orientation. In order to quantify the source localization error, two different error measures are used. The position error is the Euclidean distance, d , between the actual dipole location, $(x_{\text{act}}, y_{\text{act}}, z_{\text{act}})$, and the estimated dipole location, $(x_{\text{est}}, y_{\text{est}}, z_{\text{est}})$, such that

$$d = \sqrt{(x_{\text{est}} - x_{\text{act}})^2 + (y_{\text{est}} - y_{\text{act}})^2 + (z_{\text{est}} - z_{\text{act}})^2}. \quad (6.1)$$

Three different measures of the position error will be provided: the mean position error, \bar{d} , the maximum position error, d_{\max} , and the minimum position error, d_{\min} . The orientation error is the angle, θ , between the actual dipole orientation vector, \mathbf{r}_{act} , and the estimated dipole orientation vector, \mathbf{r}_{est} , such that

$$\theta = \cos^{-1} \left(\frac{\mathbf{r}_{\text{act}} \cdot \mathbf{r}_{\text{est}}}{|\mathbf{r}_{\text{act}}| |\mathbf{r}_{\text{est}}|} \right). \quad (6.2)$$

As with the position error, three different measures of the orientation error will be provided: the mean orientation error, $\bar{\theta}$, the maximum orientation error, θ_{\max} , and the minimum orientation error, θ_{\min} .

It is important to note that these calculations will just quantify the error associated with neglecting anisotropy. Any modeling error associated with the FVM will cancel out since the FVM is used for both the forward and inverse problems. For example, if the forward problem is solved for a given dipole in a head with anisotropic conductivity and the inverse problem is solved for the exact same head, there will be no position or orientation error. Therefore, the error that results from changing the head model used by the inverse problem is solely due to the change in conductivity.

6.2 Results

The results from the source localization error calculations are shown in Table 6.1. Additional information is also provided by the error histograms in Figure 6.4, which indicate that the position and orientation errors do not have normal distributions. This was also suggested by the results in Table 6.1, indicating that the mean, maximum, and minimum error values provide a good description of the error distribution. The error histograms in Figure 6.4 indicate that the position and orientation errors do not have normal distributions. The average solution time required by the PCG method to solve the forward problem was 9 minutes, 29 seconds for the anisotropic head model and 5 minutes, 15 seconds for the isotropic head model. As was observed for the validation experiments, the solution time increases when the amount of anisotropic tissue increases.

Table 6.1: Source localization error due to neglecting anisotropy.

Position Error (mm)			Orientation Error (degrees)		
\bar{d}	d_{\max}	d_{\min}	$\bar{\theta}$	θ_{\max}	θ_{\min}
2.23	23.02	0.00	7.12	65.16	0.08

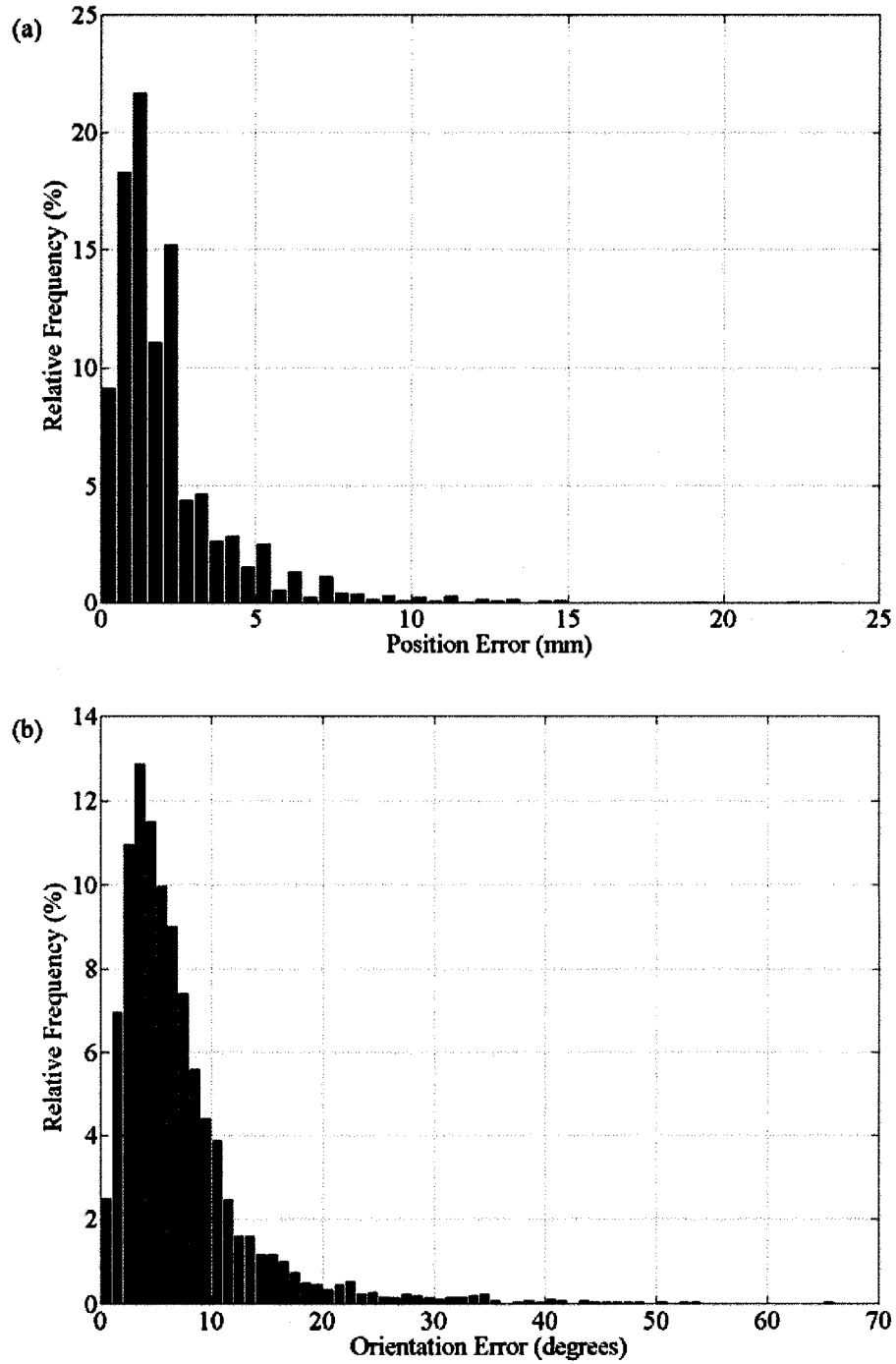


Figure 6.4: Source localization error histograms. Histograms are shown for the (a) position and (b) orientation errors.

Neglecting anisotropy seems to have a moderate effect on the source localization accuracy, with values of 2.23 mm and 7.12° for the mean position and orientation errors, respectively. The maximum values for the position and orientation errors indicate that, in extreme cases, neglecting anisotropy can have a considerable effect on source

localization accuracy with position and orientation errors reaching values of 23.02 mm and 65.16° , respectively. In order to visually illustrate the effect of neglecting anisotropy, Figure 6.5 shows the normalized scalp voltages on the isotropic and anisotropic head models. The effect of anisotropy is further illustrated in Figure 6.6, which shows the normalized scalp potentials for a slice of the head in the axial plane at the same level as the dipole. While there are observable differences in both the magnitude and shape of the scalp voltages, most of the differences are subtle. These subtle changes can still lead to significant dipole localization error, though. In this case, the scalp voltages shown in Figure 6.5 and Figure 6.6 are for a dipole location and orientation that resulted in a position error of 7.62 mm and an orientation error of 2.16° .

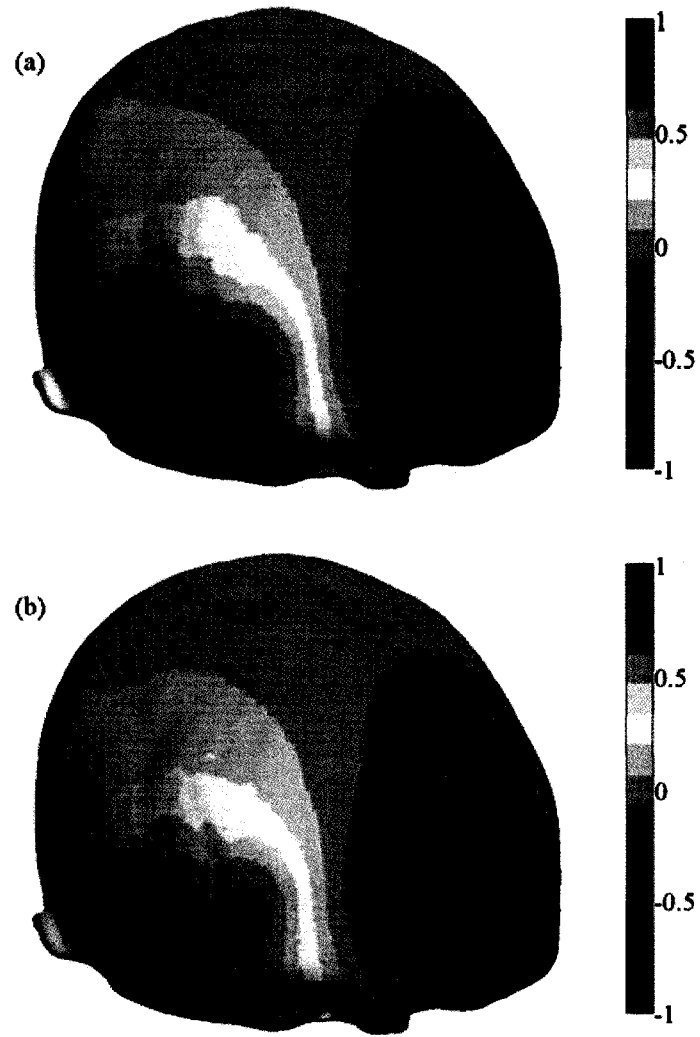


Figure 6.5: Normalized scalp voltages for the realistic head model. The scalp voltages shown are for the (a) isotropic and (b) anisotropic head models.

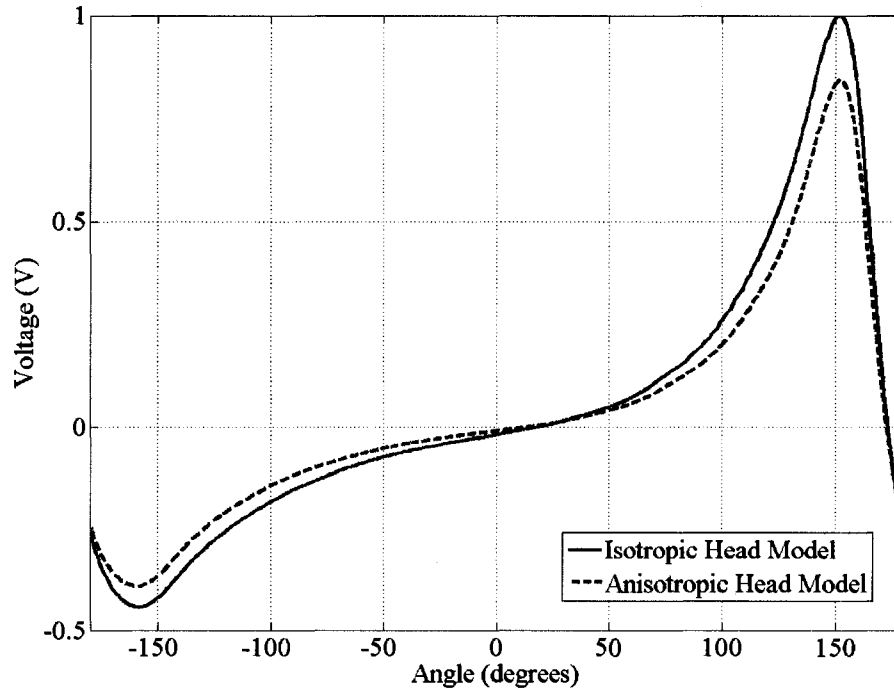


Figure 6.6: Normalized scalp voltages for an axial slice of the realistic head model. The axial slice is located at the same level as the dipole.

6.3 Discussion

In this chapter, the FVM and a realistic head model were used to investigate the influence of anisotropy on the accuracy of EEG source analysis. When the brain's anisotropy is not accounted for, it was shown that there is a definite decrease in the source localization accuracy. On average, the position and orientation errors had values of 2.23 mm and 7.12°, respectively. While these mean values are not particularly large, the maximum values for the position and orientation errors were 23.02 mm and 65.16°, respectively, showing that neglecting anisotropy can have a significant effect on EEG source analysis accuracy. It is important to realize that the value of these quantitative results could vary from patient to patient, but it is equally important to realize that neglecting anisotropy has been shown to cause a measurable reduction in source localization accuracy. Therefore, it is advisable to not ignore anisotropy without prior knowledge of how it affects the source localization accuracy for a particular patient's head model.

In this study, the effect on source localization accuracy was only investigated for the case when the brain's anisotropy is neglected. While the skull can be considered an

anisotropic tissue, it was only modeled as being isotropic due to the lack of available skull data. DTI can not provide conductivity tensors for the skull and T1-weighted MRI can not differentiate between spongy and compact bone. If any of this data was available, a more accurate representation of the skull could have been included in the realistic head model. As with the brain's anisotropy, it is expected that not accounting for the skull's anisotropy will result in decreased source localization accuracy.

While not presented in the results, it is worth mentioning that a majority of the larger position and orientation errors occurred for dipoles located near the bottom of the head model. The reason for this is not fully understood, but there are several possible explanations. First, the electrode placement is less dense near the bottom of the head. It is likely that the electrodes may not be as sensitive to different dipole locations and orientations near the bottom of the head model. This could result in very similar electrode voltages for many different dipoles. Second, the realistic head model, as seen in Figure 6.2, does not include the entire head, stopping part way down. It is suspected this anatomically incomplete head model may have influenced the results, causing some of the fairly large position and orientation errors to occur for dipoles near the bottom of the head model. Unfortunately, the MRI and DTI data used to create the head model did not include images of the entire head, so this situation could not be remedied or investigated further. In future studies, however, it would be worthwhile to acquire MRI and DTI data for the entire head, eliminating this potential source of error.

As with the results from the validation experiments, the results from this chapter can be further evaluated by comparing them to results in the literature. Some studies have been conducted that investigated the effect of anisotropy with realistic head models, but they only looked at the surface voltage errors that resulted from neglecting anisotropy instead of the source localization error [62, 85]. Another study looked at the source localization error that resulted from neglecting WM anisotropy, but it used a five-shell spherical head model instead of a realistic head model [60]. Due to the differences in head models and conductivity values, it is difficult to make a direct comparison to the results in this chapter. However, the general conclusion from the literature [60, 62, 85] is that anisotropy does affect source localization accuracy, albeit to varying degrees.

The main conclusion that can be drawn from this study is that anisotropic conductivities should not be neglected. So as to not incur unnecessary source localization errors, it is important to model the head tissues as accurately as possible, including using patient-specific conductivity values when available.

Chapter 7: Conclusions and Future Directions

The main objective of the research presented in this thesis was to improve the accuracy of electroencephalogram (EEG) source analysis by developing a more realistic head volume conductor model. Specifically, this was accomplished by creating a high-resolution finite volume method (FVM) head model that accounts for anisotropic conductivities. Two versions of an anisotropic head model were initially developed in two dimensions, using the voxel- and vertex-centered approaches to the FVM. It was ultimately determined that the vertex-centered approach is better suited to EEG source analysis, due in large part to the fact that it is more accurate than the voxel-centered approach and it requires significantly less memory to be implemented on a desktop computer.

Therefore, the final version of the anisotropic FVM head model was developed in three dimensions using the vertex-centered approach. Two different validation experiments were used to evaluate the numerical accuracy of the FVM, with the analytical solution on a three-shell spherical head serving as the “gold standard” of comparison. For both validation experiments the FVM head model was shown to produce accurate results for isotropic conductivities and for anisotropic conductivities with an anisotropy ratio of 2:1. Additionally, it was shown that the accuracy of the FVM head model decreased as the anisotropy ratio increased to 5:1 and 10:1; that is, the modeling error of the FVM head model increases for higher anisotropy ratios. It is felt that this is one of only a few studies to investigate the relationship between the accuracy of a numerical head model and the degree of anisotropy present in the head.

In addition to validating the FVM head model, another study was done in which the effect of neglecting anisotropy was investigated. With a realistic head model generated from magnetic resonance imaging (MRI) and diffusion tensor imaging (DTI) data sets, the anisotropic FVM head model was used to calculate the source localization error that occurs when anisotropic brain tissue is modeled as being isotropic. It was determined that anisotropy should not be ignored, as there is a noteworthy amount of source localization error that occurs. It is expected that this error would even larger if the influence of the skull’s anisotropy was investigated as well.

The research presented in this thesis is, by no means, an exhaustive study of the anisotropic FVM head model. There are several directions that future research in this area could take. Further research should be pursued with regards to optimizing the parameters for the preconditioned conjugate gradient (PCG) method. While convergence of the PCG method was achieved to the desired relative residual value, it is not clear whether the optimal values were used for the polynomial preconditioning. With this in mind, it is believed that better characterization of the anisotropic FVM head model would be beneficial. For example, it is possible that a more in depth understanding of the system matrix properties could lead to better estimates of the spectral bounds, which would ultimately help improve the speed of convergence of the PCG method. Another issue that should be addressed is improving the accuracy of the conductivity data. This data is obtained by scaling the DTI data using a scaling factor that was empirically determined by other researchers using their own DTI data. It would be worth investigating the feasibility of determining this scaling factor for each set of DTI data and whether it would have a significant effect on the overall EEG source analysis accuracy.

Another issue that could be improved upon in the future is the fact that the error calculations in this thesis were somewhat limited due to memory and time constraints. In Chapter 5 and Chapter 6 only one hundred and one thousand random dipole locations were used for the source localization error calculations, respectively. With enough time and computational resources, a more exhaustive set of calculations could be performed for every possible dipole location in the solution space and for each of the three mutually orthogonal orientations. This would provide a better measure of the mean position and orientation errors and would allow the errors to be displayed on the three-dimensional head model. This could help determine if a relationship exists between source localization error and the head model anatomy.

In the future, one of the biggest areas of concern should be improving the overall speed of the process of generating a head model and solving the inverse problem. If EEG source analysis is to be adopted as a standard diagnostic tool for epilepsy, in addition to being accurate it needs to be fast. One aspect of creating a realistic head model that is particularly time consuming is the image segmentation. While the FSL software package is very efficient with its fully automated segmentation of the brain, the semi-automated

procedure offered by mTrack takes considerably longer. It was mentioned, though, that FSL could potentially segment the entire head as long as both T1- and T2-weighted MRI data sets were available. This is definitely worth considering in the future, but the benefits of the time savings should be weighed against the potential loss in segmentation accuracy. Another method of improving the speed of the entire process would be to convert all of the MATLAB code into some lower level programming language such as C/C++. While MATLAB is especially useful for dealing with vectors and matrices and data visualization, it leaves something to be desired when it comes to efficiently managing memory. It is felt that more dynamic control over the memory management of the programs would ultimately make them run more efficiently. While it may seem obvious, another easy way to improve the speed of EEG source analysis would be to use more powerful computers. Desktop computers with 64-bit and multi-core processors are common place these days and could definitely offer more memory and time savings compared to the desktop computer used for this research. It is also worth investigating the possibility of running the code on a supercomputer with parallel processors. This may require some effort in terms of parallelizing the code, but the additional effort may be worth it. It should be noted that more memory efficient program code and more powerful computers would also allow for higher resolution head models to be created, improving the overall accuracy of the EEG source analysis.

References

- [1] "Epilepsy Canada," retrieved January 24, 2007, <http://www.epilepsy.ca>.
- [2] S. C. Schachter, "Who gets epilepsy?," retrieved January 30, 2007, http://www.epilepsy.com/101/ep101_who.html.
- [3] P. W. Nicholson, "Specific impedance of cerebral white matter," *Experimental Neurology*, vol. 13, pp. 386-401, 1965.
- [4] S. Rush and D. A. Driscoll, "Current distribution in the brain from surface electrodes," *Anesthesia and Analgesia*, vol. 47, pp. 717-723, 1968.
- [5] S. C. Schachter, "Symptoms of a seizure," retrieved January 30, 2007, http://www.epilepsy.com/101/ep101_symptom.html.
- [6] E. P. Widmaier, H. Raff, and K. T. Strang, "Chapter 8: Consciousness, the Brain, and Behavior," in *Vander, Sherman, & Luciano's Human Physiology: The Mechanisms of Body Function*, 9 ed. New York: McGraw-Hill, 2004, pp. 245-266.
- [7] S. C. Schachter, "Types of seizures," retrieved January 30, 2007, http://www.epilepsy.com/101/ep101_symptom.html.
- [8] J. R. Smith, M. R. Lee, D. W. King, A. M. Murro, Y. D. Park, G. P. Lee, D. W. Loring, K. J. Meador, and R. Harp, "Results of lesional vs. nonlesional frontal lobe epilepsy surgery," *Stereotactic and Functional Neurosurgery*, vol. 69, pp. 202-209, 1997.
- [9] Z. J. Koles, "Trends in EEG source localization," *Electroencephalography and Clinical Neurophysiology*, vol. 106, pp. 127-137, 1998.
- [10] R. Plonsey and D. B. Heppner, "Considerations of quasi-stationarity in electrophysiological systems," *Bulletin of Mathematical Biophysics*, vol. 29, pp. 657-664, 1967.
- [11] H. P. Schwan and C. F. Kay, "Capacitive properties of body tissues," *Circulation Research*, vol. 5, pp. 439-443, 1957.
- [12] D. B. Geselowitz, "The concept of an equivalent cardiac generator," *Biomedical Sciences Instrumentation*, vol. 1, pp. 325-330, 1963.
- [13] J. C. de Munck, B. W. Van Dijk, and H. Spekreijse, "Mathematical dipoles are adequate to describe realistic generators of human brain activity," *IEEE Transactions on Biomedical Engineering*, vol. 35, pp. 960-966, 1988.

- [14] J. S. Ebersole, "Noninvasive localization of epileptogenic foci by EEG source modeling," *Epilepsia*, vol. 41 (Supplement 3), pp. S24-S33, 2000.
- [15] J. S. Ebersole, "Defining epileptogenic foci: past, present, future," *Journal of Clinical Neurophysiology*, vol. 14, pp. 470-483, 1997.
- [16] J. Haueisen, A. Bottner, H. Nowak, H. Brauer, and C. Weiller, "The influence of conductivity changes in boundary element compartments on the forward and inverse problem in electroencephalography and magnetoencephalography," *Biomedizinische Technik*, vol. 44, pp. 150-157, 1999.
- [17] J. Haueisen, C. Ramon, M. Eiselt, H. Brauer, and H. Nowak, "Influence of tissue resistivities on neuromagnetic fields and electric potentials studied with a finite element model of the head," *IEEE Transactions on Biomedical Engineering*, vol. 44, pp. 727-735, 1997.
- [18] B. Vanrumste, G. Van Hoey, R. Van de Walle, M. D'Have, I. Lemahieu, and P. Boon, "Dipole location errors in electroencephalogram source analysis due to volume conductor model errors," *Medical and Biological Engineering and Computing*, vol. 38, 2000.
- [19] N. G. Gencer and C. E. Acar, "Sensitivity of EEG and MEG measurements to tissue conductivity," *Physics in Medicine and Biology*, vol. 49, pp. 701-717, 2004.
- [20] P. Laarne, P. Kauppinen, J. Hyttinen, J. Malmivuo, and H. Eskola, "Effects of tissue resistivity on electroencephalogram sensitivity distribution," *Medical and Biological Engineering and Computing*, vol. 37, pp. 555-559, 1999.
- [21] R. Pohlmeier, H. Buchner, G. Knoll, A. Rienacker, R. Beckmann, and J. Pesch, "The influence of skull - conductivity misspecification on inverse source localization in realistically shaped finite element head models," *Brain Topography*, vol. 9, pp. 157-162, 1997.
- [22] D. S. Tuch, V. J. Wedeen, A. M. Dale, J. S. George, and J. W. Belliveau, "Conductivity mapping of biological tissue using diffusion MRI," *Annals of New York Academy of Sciences*, vol. 888, pp. 314-316, 1999.
- [23] D. S. Tuch, V. J. Wedeen, A. M. Dale, J. S. George, and J. W. Belliveau, "Conductivity tensor mapping of the human brain using diffusion tensor MRI," *Proceedings of the National Academy of Sciences of the United States of America*, vol. 98, pp. 11697-11701, 2001.
- [24] D. S. Tuch, V. J. Wedeen, A. M. Dale, and J. W. Belliveau, "Electrical conductivity tensor map of the human brain using NMR diffusion imaging: an effective medium approach," in *Proceedings of the 6th Annual Meeting of the International Society for Magnetic Resonance in Medicine*, Sydney, Australia, 1998, pp. 572.

- [25] S. I. Goncalves, J. C. de Munck, J. P. A. Verbunt, F. Bijma, R. M. Heethaar, and F. Lopes da Silva, "In vivo measurement of the brain and skull resistivities using an EIT-based method and realistic models for the head," *IEEE Transactions on Biomedical Engineering*, vol. 50, pp. 754-767, 2003.
- [26] D. Gutierrez, A. Nehorai, and C. H. Muravchik, "Estimating brain conductivities and dipole source signals with EEG arrays," *IEEE Transactions on Biomedical Engineering*, vol. 51, pp. 2113-2122, 2004.
- [27] T. C. Ferree, K. J. Erikson, and D. M. Tucker, "Regional head tissue conductivity estimation for improved EEG analysis," *IEEE Transactions on Biomedical Engineering*, vol. 47, pp. 1584-1592, 2000.
- [28] R. D. Stoy, K. R. Foster, and H. P. Schwan, "Dielectric properties of mammalian tissues from 0.1 to 100 MHz: a summary of recent data," *Physics in Medicine and Biology*, vol. 27, pp. 501-513, 1982.
- [29] L. A. Geddes and L. E. Baker, "The specific resistance of biological material - a compendium of data for the biomedical engineer and physiologist," *Medical and Biological Engineering and Computing*, vol. 5, pp. 271-293, 1967.
- [30] H. C. Burger and R. van Dongen, "Specific electric resistance of body tissues," *Physics in Medicine and Biology*, vol. 5, pp. 431-447, 1961.
- [31] S. B. Baumann, D. R. Wozny, S. K. Kelly, and F. M. Meno, "The electrical conductivity of human cerebrospinal fluid at body temperature," *IEEE Transactions on Biomedical Engineering*, vol. 44, pp. 220-223, 1997.
- [32] M. Yedlin, H. Kwan, J. T. Murphy, H. Nguyen-Huu, and Y. C. Wong, "Electrical conductivity in cat cerebellar cortex," *Experimental Neurology*, vol. 43, pp. 555-569, 1974.
- [33] T. F. Oostendorp, J. Delbeke, and D. F. Stegeman, "The conductivity of the human skull: results of in vivo and in vitro measurements," *IEEE Transactions on Biomedical Engineering*, vol. 47, pp. 1487-1492, 2000.
- [34] R. Hoekema, G. H. Wieneke, F. S. S. Leijten, C. W. M. van Veelen, P. C. van Rijen, G. J. M. Huiskamp, J. Ansems, and A. C. van Huffelen, "Measurement of the conductivity of skull, temporarily removed during epilepsy surgery," *Brain Topography*, vol. 16, pp. 29-38, 2003.
- [35] M. Akhtari, H. C. Bryant, A. N. Mamelak, L. Heller, J. J. Shih, M. Mandelkern, A. Matlachov, D. M. Ranken, and W. W. Sutherling, "Conductivities of three-layer human skull," *Brain Topography*, vol. 13, pp. 29-42, 2000.
- [36] Y. Lai, W. van Drongelen, L. Ding, K. E. Hecox, V. L. Towle, D. M. Frim, and B. He, "Estimation of in vivo human brain-to-skull conductivity ratio from

- simultaneous extra- and intra-cranial electrical potential recordings," *Clinical Neurophysiology*, vol. 116, pp. 456-465, 2005.
- [37] K. R. Foster and H. P. Schwan, "Dielectric properties of tissues and biological materials: a critical review," *Critical Reviews in Biomedical Engineering*, vol. 17, pp. 25-104, 1989.
- [38] S. K. Law, "Thickness and resistivity variations over the upper surface of the human skull," *Brain Topography*, vol. 6, pp. 99-109, 1993.
- [39] D. Cohen and B. N. Cuffin, "Demonstration of useful differences between magnetoencephalogram and electroencephalogram," *Electroencephalography and Clinical Neurophysiology*, vol. 56, pp. 38-51, 1983.
- [40] Y. Zhang, W. van Drongelen, and B. He, "Estimation of in vivo brain-to-skull conductivity ratio in humans," *Applied Physics Letters*, vol. 89, pp. 2239031-3, 2006.
- [41] L. W. Lake, "The origins of anisotropy," *Journal of Petroleum Technology*, pp. 395-396, 1988.
- [42] B. N. Cuffin, "A method for localizing EEG sources in realistic head models," *IEEE Transactions on Biomedical Engineering*, vol. 42, pp. 68-71, 1995.
- [43] B. Vanrumste, G. Van Hoey, R. Van de Walle, M. D'Have, I. Lemahieu, and P. Boon, "The validation of the finite difference method and reciprocity for solving the inverse problem in EEG dipole source analysis," *Brain Topography*, vol. 14, pp. 83-92, 2001.
- [44] J. Haueisen, C. Ramon, P. Czapski, and M. Eiselt, "On the influence of volume currents and extended sources on neuromagnetic fields: a simulation study," *Annals of Biomedical Engineering*, vol. 23, pp. 728-739, 1995.
- [45] C. Ramon, P. Schimpf, J. Haueisen, M. Holmes, and A. Ishimaru, "Role of soft bone, CSF, and gray matter in EEG simulations," *Brain Topography*, vol. 16, pp. 245-248, 2004.
- [46] M. Rosenfeld, R. Tanami, and S. Abboud, "Numerical solution of the potential due to dipole sources in volume conductors with arbitrary geometry and conductivity," *IEEE Transactions on Biomedical Engineering*, vol. 43, pp. 679-689, 1996.
- [47] S. Abboud, Y. Eshel, S. Levy, and M. Rosenfeld, "Numerical calculation of the potential distribution due to dipole sources in a spherical model of the head," *Computers and Biomedical Research*, vol. 27, pp. 441-455, 1994.

- [48] S. Abboud, M. Rosenfeld, and J. Luzon, "Effect of source location on the scalp potential asymmetry in a numerical model of the head," *IEEE Transactions on Biomedical Engineering*, vol. 43, pp. 690-696, 1996.
- [49] M. Mohr and B. Vanrumste, "Comparing iterative solvers for linear systems associated with the finite difference discretisation of the forward problem in electro-encephalographic source analysis," *Medical and Biological Engineering and Computing*, vol. 41, pp. 75-84, 2003.
- [50] L. Lemieux, A. McBride, and J. W. Hand, "Calculation of electrical potentials on the surface of a realistic head model by finite differences," *Physics in Medicine and Biology*, vol. 41, pp. 1079-1091, 1996.
- [51] J. W. H. Meijs, O. W. Weier, M. J. Peters, and A. Van Oosterom, "On the numerical accuracy of the boundary element method," *IEEE Transactions on Biomedical Engineering*, vol. 36, pp. 1038-1049, 1989.
- [52] B. Vanrumste, "EEG dipole source analysis in a realistic head model," Ph.D. thesis, Department of Electronics and Information Systems, Ghent University, Ghent, Belgium, 2001.
- [53] B. N. Cuffin, "Effects of head shape on EEG's and MEG's," *IEEE Transactions on Biomedical Engineering*, vol. 37, pp. 44-52, 1990.
- [54] B. N. Cuffin, "EEG localization accuracy improvements using realistically shaped head models," *IEEE Transactions on Biomedical Engineering*, vol. 43, pp. 299-303, 1996.
- [55] B. N. Cuffin, D. L. Schomer, J. R. Ives, and H. Blume, "Experimental tests of EEG source localization accuracy in realistically shaped head models," *Clinical Neurophysiology*, vol. 112, pp. 2288-2292, 2001.
- [56] J. S. Shimony, R. C. McKinstry, E. Akbudak, J. A. Aronovitz, A. Z. Snyder, N. F. Lori, T. S. Cull, and T. E. Conturo, "Quantitative diffusion-tensor anisotropy brain MR imaging: normative human data and anatomic analysis," *Radiology*, vol. 212, pp. 770-784, 1999.
- [57] C. Nicholson and J. A. Freeman, "Theory of current source-density analysis and determination of conductivity tensor for anuran cerebellum," *Journal of Neurophysiology*, vol. 38, pp. 356-368, 1975.
- [58] G. Marin, C. Guerin, S. Baillet, L. Garnero, and G. Meunier, "Influence of skull anisotropy for the forward and inverse problem in EEG: simulation studies using FEM on realistic head models," *Human Brain Mapping*, vol. 6, pp. 250-269, 1998.
- [59] C. H. Wolters, "Influence of tissue conductivity inhomogeneity and anisotropy on EEG/MEG based source localization in the human brain," Ph.D. dissertation,

Faculty of Mathematics and Computer Science, University of Leipzig, Leipzig, Germany, 2003.

- [60] H. Hallez, B. Vanrumste, P. Van Hese, Y. D'Asseler, I. Lemahieu, and R. Van de Walle, "A finite difference method with reciprocity used to incorporate anisotropy in electroencephalogram dipole source localization," *Physics in Medicine and Biology*, vol. 50, pp. 3787-3806, 2005.
- [61] S. P. van den Broek, F. Reinders, M. Donderwinkel, and M. J. Peters, "Volume conduction effects in EEG and MEG," *Electroencephalography and Clinical Neurophysiology*, vol. 106, pp. 522-534, 1998.
- [62] J. Haueisen, D. S. Tuch, C. Ramon, P. H. Schimpf, V. J. Wedeen, J. S. George, and J. W. Belliveau, "The influence of brain tissue anisotropy on human EEG and MEG," *NeuroImage*, vol. 15, pp. 159-166, 2002.
- [63] D. Gullmar, J. Haueisen, M. Eiselt, F. Giessler, L. Flemming, A. Anwander, T. R. Knosche, C. H. Wolters, M. Dumpelmann, D. S. Tuch, and J. R. Reichenbach, "Influence of anisotropic conductivity on EEG source reconstruction: investigations in a rabbit model," *IEEE Transactions on Biomedical Engineering*, vol. 53, pp. 1841-1850, 2006.
- [64] P. J. Basser, J. Mattiello, and D. Le Bihan, "MR diffusion tensor spectroscopy and imaging," *Biophysical Journal*, vol. 66, pp. 259-267, 1994.
- [65] P. J. Basser, J. Mattiello, and D. Le Bihan, "Estimation of the effective self-diffusion tensor from the NMR spin echo," *Journal of Magnetic Resonance, Series B*, vol. 103, pp. 247-254, 1994.
- [66] E. Frank, "Electric potential produced by two point current sources in a homogeneous conducting sphere," *Journal of Applied Physics*, vol. 23, pp. 1225-1228, 1952.
- [67] J. C. de Munck, "The potential distribution in a layered anisotropic spheroidal volume conductor," *Journal of Applied Physics*, vol. 64, pp. 464-470, 1988.
- [68] J. C. de Munck and M. J. Peters, "A fast method to compute the potential in the multisphere model," *IEEE Transactions on Biomedical Engineering*, vol. 40, pp. 1166-1174, 1993.
- [69] H. Zhou and A. van Oosterom, "Computation of the potential distribution in a four-layer anisotropic concentric spherical volume conductor," *IEEE Transactions on Biomedical Engineering*, vol. 39, pp. 154-158, 1992.
- [70] S. Rush and D. A. Driscoll, "EEG electrode sensitivity - an application of reciprocity," *IEEE Transactions on Biomedical Engineering*, vol. BME-16, pp. 15-22, 1969.

- [71] J. P. Ary, S. A. Klein, and D. H. Fender, "Location of sources of evoked scalp potentials: corrections for skull and scalp thicknesses," *IEEE Transactions on Biomedical Engineering*, vol. BME-28, pp. 447-452, 1981.
- [72] B. J. Roth, M. Balish, A. Gorbach, and S. Sato, "How well does a three-sphere model predict positions of dipoles in a realistically shaped head?," *Electroencephalography and Clinical Neurophysiology*, vol. 87, pp. 175-184, 1993.
- [73] M. Fuchs, R. Drenckhahn, H. A. Wischmann, and M. Wagner, "An improved boundary element method for realistic volume-conductor modeling," *IEEE Transactions on Biomedical Engineering*, vol. 45, pp. 980-997, 1998.
- [74] M. Fuchs, M. Wagner, and J. Kastner, "Boundary element method volume conductor models for EEG source reconstruction," *Clinical Neurophysiology*, vol. 112, pp. 1400-1407, 2001.
- [75] B. He, T. Musha, Y. Okamoto, S. Homma, Y. Nakajima, and T. Sato, "Electric dipole tracing in the brain by means of the boundary element method and its accuracy," *IEEE Transactions on Biomedical Engineering*, vol. BME-34, pp. 406-414, 1987.
- [76] M. D. Teubner, J. B. Nixon, P. E. Rasser, M. J. Bottema, and C. R. Clark, "Source localisation in a real human head," *Brain Topography*, vol. 17, pp. 197-205, 2005.
- [77] B. Vanrumste, G. Van Hoey, P. Boon, M. D'Have, and I. Lemahieu, "Inverse calculations in EEG source analysis applying the finite difference method, reciprocity and lead fields," in *Proceedings of the 20th Annual International Conference of the IEEE Engineering in Medicine and Biology Society*, Hong Kong, China, 1998, pp. 2112-2115.
- [78] J. Li, S. Zhu, and B. He, "A finite difference method for solving the three-dimensional EEG forward problem," in *Proceedings of the 27th Annual International Conference of the IEEE Engineering in Medicine and Biology Society*, Shanghai, China, 2005, pp. 1540-1543.
- [79] V. Hedou-Rouillier, "A finite difference method to solve the forward problem in electroencephalography (EEG)," *Journal of Computational and Applied Mathematics*, vol. 167, pp. 35-38, 2004.
- [80] J. B. Nixon, P. E. Rasser, M. D. Teubner, C. R. Clark, and M. J. Bottema, "Numerical model of electrical potential within the human head," *International Journal for Numerical Methods in Engineering*, vol. 56, pp. 2353-2366, 2003.
- [81] H. I. Saleheen and K. T. Ng, "New finite difference formulations for general inhomogeneous anisotropic bioelectric problems," *IEEE Transactions on Biomedical Engineering*, vol. 44, pp. 800-809, 1997.

- [82] A. R. Mitchell and D. F. Griffiths, *The finite difference method in partial differential equations*. London: John Wiley & Sons, 1980.
- [83] F. J. Asencor and M. Panizo, "Finite-difference operators in anisotropic inhomogeneous dielectrics: general case," *Journal of Computational Physics*, vol. 95, pp. 387-399, 1991.
- [84] M. Panizo, A. Castellanos, and J. Rivas, "Finite-difference operators in inhomogeneous anisotropic media," *Journal of Applied Physics*, vol. 48, pp. 1054-1057, 1977.
- [85] S. Kim, T.-S. Kim, Y. Zhou, and M. Singh, "Influence of conductivity tensors on the scalp electrical potential: study with 2-D finite element models," *IEEE Transactions on Nuclear Science*, vol. 50, pp. 133-139, 2003.
- [86] C. H. Wolters, M. Kuhn, A. Anwander, and S. Reitzinger, "A parallel algebraic multigrid solver for finite element method based source localization in the human brain," *Computing and Visualization in Science*, vol. 5, pp. 165-177, 2002.
- [87] C. H. Wolters, A. Anwander, X. Tricoche, D. Weinstein, M. A. Koch, and R. S. MacLeod, "Influence of tissue conductivity anisotropy on EEG/MEG field and return current computation in a realistic head model: A simulation and visualization study using high-resolution finite element modeling," *NeuroImage*, vol. 30, pp. 813-826, 2006.
- [88] Y. C. Zhang, S. A. Zhu, and B. He, "A second-order finite element algorithm for solving the three-dimensional EEG forward problem," *Physics in Medicine and Biology*, vol. 49, pp. 2975-2987, 2004.
- [89] K. A. Awada, D. R. Jackson, J. T. Williams, D. R. Wilton, S. B. Baumann, and A. C. Papanicolaou, "Computational aspects of finite element modeling in EEG source localization," *IEEE Transactions on Biomedical Engineering*, vol. 44, pp. 736-752, 1997.
- [90] H. Buchner, G. Knoll, M. Fuchs, A. Rienacker, R. Beckmann, M. Wagner, J. Silny, and J. Pesch, "Inverse localization of electric dipole current sources in finite element models of the human head," *Electroencephalography and Clinical Neurophysiology*, vol. 102, pp. 267-278, 1997.
- [91] P. Schimpf, C. Ramon, and J. Hauelsen, "Dipole models for the EEG and MEG," *IEEE Transactions on Biomedical Engineering*, vol. 49, pp. 409-418, 2002.
- [92] G. W. Pruis, B. H. Gilding, and M. J. Peters, "A comparison of different numerical methods for solving the forward problem in EEG and MEG," *Physiological Measurement*, vol. 14, pp. A1-A9, 1993.
- [93] S. V. Patankar, *Numerical heat transfer and fluid flow*. Washington: Hemisphere, 1980.

- [94] Y. Xie, J. Yuan, X. Ma, and X. Guan, "Calculation of EEG problems with anisotropic conducting media by the finite volume method," *IEEE Transactions on Magnetics*, vol. 37, pp. 3749-3752, 2001.
- [95] L. A. Neilson and Z. J. Koles, "The finite volume head model for EEG source localization," *International Journal of Bioelectromagnetism*, vol. 4, pp. 149-150, 2002.
- [96] L. A. Neilson, "Realistic head volume conductor modeling for EEG source localization," M.Sc. thesis, Department of Electrical and Computer Engineering/Biomedical Engineering, University of Alberta, Edmonton, Canada, 2003.
- [97] L. A. Neilson, M. Kovalyov, and Z. J. Koles, "A computationally efficient method for accurately solving the EEG forward problem in a finely discretized head model," *Clinical Neurophysiology*, vol. 116, pp. 2302-2314, 2005.
- [98] Y. Eshel, S. Witman, M. Rosenfeld, and S. Abboud, "Correlation between skull thickness asymmetry and scalp potential estimated by a numerical model of the head," *IEEE Transactions on Biomedical Engineering*, vol. 42, pp. 242-249, 1995.
- [99] Y. Xie and X. Ma, "Calculation of EEG anisotropic forward problems by the FVM-BEM coupled approach," *International Journal of Applied Electromagnetics and Mechanics*, vol. 16, pp. 145-152, 2002.
- [100] N. L. Kuzbik and Z. J. Koles, "The effect of white matter anisotropy on the EEG forward problem," *International Journal of Bioelectromagnetism*, vol. 7, pp. 127-130, 2005.
- [101] G. Dong, J. Zou, R. H. Bayford, X. Ma, S. Gao, W. Yan, and M. Ge, "The comparison between FVM and FEM for EIT forward problem," *IEEE Transactions on Magnetics*, vol. 41, pp. May 2005, 2005.
- [102] S. Zlochiver, M. M. Radai, M. Rosenfeld, and S. Abboud, "Induced current impedance technique for monitoring brain cryosurgery in a two-dimensional model of the head," *Annals of Biomedical Engineering*, vol. 30, pp. 1172-1180, 2002.
- [103] S. Zlochiver, M. Rosenfeld, and S. Abboud, "Induced-current electrical impedance tomography: a 2-D theoretical simulation," *IEEE Transactions on Medical Imaging*, vol. 22, pp. 1550-1560, 2003.
- [104] A. Gergel, S. Zlochiver, M. Rosenfeld, and S. Abboud, "Induced current bio-impedance technique for monitoring cryosurgery procedure in a two-dimensional head model using generalized coordinate systems," *IEEE Transactions on Biomedical Engineering*, vol. 52, pp. 1361-1365, 2005.

- [105] S. Zlochiver, M. Rosenfeld, and S. Abboud, "Contactless bio-impedance monitoring technique for brain cryosurgery in a 3D head model," *Annals of Biomedical Engineering*, vol. 33, pp. 616-625, 2005.
- [106] D. Weinstein, L. Zhukov, and C. Johnson, "Lead-field bases for electroencephalography source imaging," *Annals of Biomedical Engineering*, vol. 28, pp. 1059-1065, 2000.
- [107] J. C. Mosher, P. S. Lewis, and R. M. Leahy, "Multiple dipole modeling and localization from spatio-temporal MEG data," *IEEE Transactions on Biomedical Engineering*, vol. 39, pp. 541-557, 1992.
- [108] J. C. Mosher, S. Baillet, and R. M. Leahy, "EEG source localization and imaging using multiple signal classification approaches," *Journal of Clinical Neurophysiology*, vol. 16, pp. 225-238, 1999.
- [109] M. G. Edwards, "Split full tensor discretization operators for structured and unstructured grids in three dimensions," SPE 66358, presented at the SPE Reservoir Simulation Symposium, Houston, Texas, 2001.
- [110] P. I. Crumpton, G. J. Shaw, and A. F. Ware, "Discretisation and multigrid solution of elliptic equations with mixed derivative terms and strongly discontinuous coefficients," *Journal of Computational Physics*, vol. 116, pp. 343-358, 1995.
- [111] M. G. Edwards, "Symmetric flux continuous positive definite approximation of the elliptic full tensor pressure equation in local conservative form," SPE 29147, presented at the 13th SPE Reservoir Simulation Symposium, San Antonio, Texas, 1995.
- [112] M. G. Edwards, "Split full tensor discretization operators for general hexahedral grids," *SPE Journal*, pp. 102-108, March 2004.
- [113] M. G. Edwards and C. F. Rogers, "Finite volume discretization with imposed flux continuity for the general tensor pressure equation," *Computational Geosciences*, vol. 2, pp. 259-290, 1998.
- [114] M. G. Edwards, "Cross flow tensors and finite volume approximation with deferred correction," *Computational Methods in Applied Mechanics and Engineering*, vol. 151, pp. 143-161, 1998.
- [115] I. Aavatsmark, T. Barkve, O. Boe, and T. Mannseth, "Discretization on non-orthogonal, quadrilateral grids for inhomogeneous, anisotropic media," *Journal of Computational Physics*, vol. 127, pp. 2-14, 1996.
- [116] I. Aavatsmark, T. Barkve, O. Boe, and T. Mannseth, "Discretization on unstructured grids for inhomogeneous, anisotropic media. Part I: derivation of the methods," *SIAM Journal on Scientific Computing* vol. 19, pp. 1700-1716, 1998.

- [117] I. Aavatsmark, T. Barkve, and T. Mannseth, "Control-volume discretization methods for 3D quadrilateral grids in inhomogeneous, anisotropic reservoirs," *SPE Journal*, pp. 146-154, June 1998.
- [118] I. Aavatsmark, T. Barkve, O. Boe, and T. Mannseth, "Discretization on unstructured grids for inhomogeneous, anisotropic media. Part II: discussion and numerical results," *SIAM Journal on Scientific Computing*, vol. 19, pp. 1717-1736, 1998.
- [119] I. Aavatsmark, "An introduction to multipoint flux approximations for quadrilateral grids," *Computational Geosciences*, vol. 6, pp. 405-432, 2002.
- [120] S. H. Lee, L. J. Durlofsky, M. F. Lough, and W. H. Chen, "Finite difference simulation of geologically complex reservoirs with tensor permeabilities," *SPE Reservoir Evaluation and Engineering*, pp. 567-574, December 1998.
- [121] S. H. Lee, H. A. Tchelepi, P. Jenny, and L. J. DeChant, "Implementation of a flux-continuous finite-difference method for stratigraphic, hexahedron grids," *SPE Journal*, pp. 267-277, September 2002.
- [122] P. Bruno, J. Hyttinen, P. Inchingolo, A. Magrofuoco, S. Mininel, and F. Vatta, "A FDM anisotropic formulation for EEG simulation," in *Proceedings of the 28th Annual International Conference of the IEEE Engineering in Medicine and Biology Society*, New York City, USA, 2006, pp. 1121-1125.
- [123] "Math Library Source Code: Eigenvalues and Eigenvectors for Symmetric Matrices," retrieved May 7, 2008, <http://mymathlib.webtrellis.net/matrices/eigen/symmetric.html>.
- [124] Q. Dong, R. C. Welsh, T. L. Chenevert, R. C. Carlos, P. Maly-Sundgren, D. M. Gomez-Hassan, and S. K. Mukherji, "Clinical applications of diffusion tensor imaging," *Journal of Magnetic Resonance Imaging*, vol. 19, pp. 6-18, 2004.
- [125] D. J. Withey, "Dynamic edge tracing: Recursive methods for medical image segmentation," Ph.D. thesis, Department of Electrical and Computer Engineering/Biomedical Engineering, University of Alberta, Edmonton, 2006.
- [126] S. M. Smith, M. Jenkinson, M. W. Woolrich, C. F. Beckmann, T. E. J. Behrens, H. Johansen-Berg, P. R. Bannister, M. De Luca, I. Drobnjak, D. E. Flitney, R. Niazy, J. Saunders, J. Vickers, Y. Zhang, N. De Stefano, J. M. Brady, and P. M. Matthews, "Advances in functional and structural MR image analysis and implementation as FSL," *NeuroImage*, vol. 23, pp. 208-219, 2004.
- [127] S. M. Smith, "Fast robust automated brain extraction," *Human Brain Mapping*, vol. 17, pp. 143-155, 2002.

- [128] Y. Zhang, M. Brady, and S. Smith, "Segmentation of brain MR images through a hidden Markov random field model and the expectation maximization algorithm," *IEEE Transactions on Medical Imaging*, vol. 20, pp. 45-57, 2001.
- [129] "DTI Studio," retrieved January 8, 2007, <http://www.mristudio.org>.